Molecular Collisional Excitation in Astrophysical Environments

and

Modeling the Early Universe

by

Kyle Matthew Walker

(Under the direction of Professor Phillip C. Stancil)

Abstract

Molecular collisions play an essential role in fields such as astrophysics, chemical physics, combustion, fusion research, and plasma physics. Even though molecular excitation calculations are vital in determining particle velocity distributions, internal state distributions, abundances, and ionization balance in gaseous environments, both theoretical calculations and experimental data for these processes are lacking. In order to probe material in astrophysical environments such as nebulae, molecular clouds, comets, and planetary atmospheres, reliable molecular collisional data for a complete set of species is needed. Since this set of data does not exist, various approximations, such as collider-mass scaling, are used to approximate unknown rate coefficients. The current collider-mass scaling approach utilized in i.e., the Leiden Atomic and Molecular Database (LAMDA), however, is flawed and an alternate scaling technique based on physical and mathematical principles, reduced potential scaling, is presented. To accelerate explicit calculations of collisional data, particularly rovibrationally resolved cross sections and rate coefficients for systems of astrophysical interest, parallelized versions of the scattering codes VRRMM and TwoBC were developed. Calculations and either zero energy or reduced potential scaling have been performed for

the systems CO-He, CO-H, H_2O-H_2, HF-H_2, HF-H, and H_2-H_2. Furthermore, the chemical evolution of primordial species in the Recombination Era was modeled, and accurate non-thermal spectra of the molecules H_2, HD, and H_2^+ were produced for a primordial cloud as it collapses into a first generation star. These first generation stars were analyzed for possible observables and evaluated for their detectability by current and future observational facilities, such as the *James Webb Space Telescope*.

INDEX WORDS: Early Universe, Molecular Data, Molecular Processes, Scattering

Molecular Collisional Excitation in Astrophysical Environments

and

Modeling the Early Universe

by

Kyle Matthew Walker

B.S., The Ohio State University, 2004

M.S., University of Toledo, 2008

A Dissertation Submitted to the Graduate Faculty

of The University of Georgia in Partial Fulfillment

of the

Requirements for the Degree

Doctor of Philosophy

Athens, Georgia

2015

Molecular Collisional Excitation in Astrophysical Environments

and

Modeling the Early Universe

by

Kyle Matthew Walker

Approved:

Major Professor: Phillip C. Stancil

Committee: Loris Magnani
Henning Meyer

Electronic Version Approved:

Suzanne Barbour
Dean of the Graduate School
The University of Georgia
August 2015

Dedication

To my family.

Acknowledgments

I would like to thank Shan-Ho Tsai of The Georgia Advanced Computing Resource Center and Jeff Deroshia and Michael Caplinger of the Department of Physics and Astronomy and the Center for Simulational Physics at the University of Georgia for computational assistance. Thanks to the Computer & Communications Department at Radboud University for computing resources. Thanks to Benhui Yang, Robert Forrey, Naduvalath Balakrishnan, Gerrit Gronenboom, Lei Song, and Ryan Porter for helpful discussions. This work was partially supported by NASA grant NNX12AF42G, HST Cycle 22 Phase II AR grant 13899, and a grant from the UGA Provost's Office.

Table of Contents

List of Figures

List of Tables

Chapter 1

Introduction

When the casual observer looks up into the night sky, his attention is consumed by the seemingly random distribution of stars that comprise our local neighborhood in the Milky Way. A more detailed inspection will yield fuzzy, extended sources such as galaxies, star clusters, and nebulae. But there is also a wealth of material that resides in between these visually striking objects that can give us detailed information about the chemical evolution of our universe. Referred to as the Interstellar Medium (ISM), the baryonic matter in between the stars — clouds of atoms, molecules, and dust — can be modeled computationally so that physical parameters of these regions can be obtained. These models help us understand the past, present, and future behavior of the universe in which we live.

One can easily see the vast difference of densities that the universe has to offer. In any high density environment, like on the surface of stars where collisions occur frequently, quantum level populations follow a Maxwell-Boltzmann distribution. It is said that the gas is in "local thermodynamic equilibrium," LTE, and that collisions have caused the gas to behave thermally. In less dense environments such as the cool, molecular regions of the ISM, the LTE approximation is often no longer valid and a detailed account of collisional processes must be given. In these non-thermal systems, said to be in NLTE, the fundamental atomic and molecular data needed to produce accurate models are collisional excitation rate coefficients. In many cases, however, the molecular collisional rate coefficients for astrophysical systems are completely unknown. Therefore, an important goal for the astrophysics community is to obtain set of rate coefficients spanning all energies, all quantum levels, and all interstellar species.

Since the rate of molecule detection in astrophysical environments is faster than the rate at which we can compute the scattering properties for the systems involved, scaling techniques are used to approximate data that is not explicitly calculated. For example, while many molecular collisional calculations have been performed using He as a collider due to its relative ease of computation, the dominant neutral species in many astrophysical environments is H_2 or H. A common practice to obtain estimates for these unknown rates is to approximate them from known rate coefficients from other collision systems, namely using He as a collider. This reduced-mass scaling relation (see, e.g., van der Tak 2011), a procedure generally ascribed to Green et al. (1978), is employed by many current modelers including those who obtain data from the Leiden Atomic and Molecular Database (LAMDA, Schöier et al. 2005). The basic idea behind standard reduced-mass scaling is that for a given molecule, rate coefficients for excitation by H_2 are related to those by He through the square root of the ratio of the systems' reduced masses. Although the primary data limited the applicability of the predictions to room temperature and above, this "standard" reduced-mass scaling relation has been used extensively for lower temperatures and for other collisional parameters, e.g., inelastic rate coefficients.

Recently, the accuracy of the standard reduced-mass scaling approach has been tested for SiS (Lique et al. 2008) and SO_2 (Cernicharo et al. 2011) excitation and found to be inaccurate (see also Roueff & Lique 2013; van der Tak 2011). My research investigates standard reduced-mass scaling by adopting CO as a test molecule and showing how the reduced mass and interaction potential energy surface (PES) impact explicitly computed rate coefficients. I also explore more physically reasonable analytical and scaling approximations to estimate unknown rate coefficients. Three new scaling techniques are presented in hopes of obtaining a complete set of rate coefficients needed to accurately model a plethora of astrophysical regions.

Due to the wealth of data and its importance in astrophysics, carbon monoxide is not only used here as a test molecule in new scaling techniques, but also a complete set of state-

to-state collisional rate coefficients for temperatures ranging from 1 to 3000 K are obtained for CO($\nu = 0$, j) deexcitation in collisions with H from initial states $j = 1 - 45$ to all lower j' levels, where j is the rotational quantum number. Coupled-channel and coupled-states calculations are performed on the most sophisticated 3-dimensional PES available with a new mixed mode OpenMP/MPI quantum scattering program for $j = 1 - 5$, 10, 15, 20, 25, 30, 35, 40, and 45 and scaling approaches are used to estimate the rate coefficients for all other intermediate rotational states. These calculations form the most complete and accurate set of rate coefficients for the H-CO system.

The only molecule in the universe more abundant than CO is H_2, whose rotational lines are difficult to observe from the ground. Since molecular hydrogen is homonuclear, it does not have a permanent dipole moment and therefore its rotational and vibrational electric dipole transitions are not allowed. Nonetheless, the significant abundance of H_2 leads it to be not only the dominant species in the ISM, but it is also crucial in heating and cooling, is a significant ultraviolet (UV) opacity source, and is a primary reactant in the pathway to the formation of other species. To obtain the most complete set of H_2 rovibrational inelastic collisional excitation rate coefficients, I have commenced 6-dimensional quantum dynamics calculations on the H_2–H_2 system in $\nu = 0 - 4$. These collisional rate coefficients will allow for more accurate modeling of H_2 and HD observations of the Lyman and Werner absorption bands from COS or STIS aboard the *Hubble Space Telescope* (*HST*) and rovibrational emission spectra from far IR/Submm telescopes.

The final chapter of this dissertation focuses on models that use molecular collisional rate coefficients as input data. A development version of the spectral synthesis code Cloudy was used to produce spectra of a primordial cloud as it collapses into a first generation star. With updated rovibrationally resolved molecular collisional data for H_2, HD, and H_2^+, this model couples the the non-equilibrium, non-thermal, time-dependent chemistry and level populations and self-consistently solves for molecular heating/cooling while tracing the chemical evolution of primordial species for a grid of reshifts from the recombination era to freeze out.

Only LTE and pre-computed rates have been considered previously. The resulting NLTE spectra of the molecules H_2, HD, and H_2^+ were produced, and the resulting first generation stars were analyzed for possible observables and evaluated for their detectability by current and future observational facilities, such as the *James Webb Space Telescope* (*JWST*).

Chapter 2

Molecular Collisional Excitation

2.1 Astrophysical Importance

Molecular collisional excitation processes play an important role in many astrophysical enviornments, and when collisional processes dominate, we use the "local thermodynamic equilibrium", or LTE, approximation. Radiative transitions are neglected and the populations of energy levels behave according to a Boltzmann distribution, i.e., the ratio of the densities of molecules from any upper state, n_i, to any lower state, n_j, is given by

$$\frac{n_i}{n_j} = \frac{g_i}{g_j}\exp\left(\frac{-\Delta E}{k_{\rm B}T_{\rm K}}\right), \tag{2.1}$$

where g_i and g_j are the statistical weights of the upper and lower states, respectively (usually defined by $g_m = 2J+1$, where J is the angular momentum quantum number of level m), ΔE is the difference in excitation energy between the two levels, $k_{\rm B}$ is the Boltzmann constant, and $T_{\rm K}$ is the kinetic temperature of the gas. However, the LTE approximation is not adequate in describing the conditions in astrophysical regions where radiative transitions have the same importance as collisional transitions, such as in photodissociation regions (PDRs), in shocks, and in other low density and/or moderately energetic environments. We can define a critical density $n_{\rm crit}(i)$ for any level i, where the collisional and radiative transitions bear equal weight, given by

$$n_{\rm crit}(i) = \frac{\sum\limits_{j<i} A_{ij}}{\sum\limits_{j\neq i} k_{ij}}, \tag{2.2}$$

where A_{ij} is Einstein's spontaneous emission probability from upper level i to lower level j and k_{ij} is the rate coefficient for collisional deexcitation or excitation out of level i. The collisional rate coefficient is given by $k_{ij} = \langle \sigma_{ij} v \rangle$, where v is the velocity of the particles responsible for the collisions, σ_{ij} is the cross section for collisional excitation, and the angled brackets indicate an average is taken over a distribution of relative velocities v. Therefore, any non-LTE (NLTE) model requires 1) Einstein's A coefficients, many of which have been measured or calculated and tabulated in databases such as the Jet Propulsion Laboratory (JPL) Submillimeter, Millimeter, and Microwave Spectral Line Catalog (Pickett et al. 1998) or the Cologne Database for Molecular Spectroscopy (CDMS, Müller et al. 2005), and 2) calculations of collisional rate coefficients, which are the focus of this chapter.

The most important species to consider as colliders are the species that are most abundant — H, H_2, He, and electrons. The focus here is on neutral–neutral collisions, so electrons are not considered. In this work, rate coefficient calculations were performed for the H/H_2/He–CO, H_2/He–H_2O, H/H_2/He–HF, and H_2–H_2 systems. The main emphasis is on the molecules H_2 and CO.

Carbon monoxide is of paramount importance, as it is the second most abundant molecule in the universe after molecular hydrogen and is found in a variety of astrophysical environments. Although the effect of electron collisions is minor, the role of collisional excitation of CO by H, especially in environments such as diffuse molecular clouds (Goldsmith 2013) and cool mixed atomic and molecular hydrogen gas (Liszt 2006), cannot be neglected. The creation of CO in low-density interstellar clouds proceeds mainly through gas-phase chemical reactions involving H_2, and therefore detecting and measuring CO spectral lines is one way to trace the molecular interstellar matter (ISM) in the region. While H_2 rotational lines are difficult to observe from the ground, CO is more easily detected as its transitions can be observed as absorption in the ultraviolet (UV) and near-infrared (NIR) and emission in the NIR, far-infrared (FIR), submillimeter (submm), and millimeter (mm). The rotational energy level spacings of a diatomic molecule depend inversely on moment of inertia, and the

relatively large moment of inertia of CO compared to H_2 yields rotational levels with small energy separation. The lowest rotational transition of CO has a wavelength of $\sim$2.6 mm which gives an excitation temperature of just $\sim$5.5 K. Therefore, CO can be easily collisionally excited to high rotational levels in energetic environments like PDRs and in shocks.

A number of CO pure rotational lines starting at $j = 14 \rightarrow 13$, where j is the rotational quantum number, have been detected with the Long-Wavelength Spectrometer (LWS, Clegg et al. 1996) aboard the *Infrared Space Observatory* (ISO, Kessler et al. 1996). These include the FIR spectra of all the lines up to $j = 39 \rightarrow 38$ in the carbon-rich circumstellar envelope IRC+10216 (Cernicharo et al. 1996), transitions up to $j = 25 \rightarrow 24$ in VY Canis Majoris and other oxygen-rich circumstellar envelopes (Polehampton et al. 2010), transitions up to $j = 24 \rightarrow 23$ from the carbon-rich planetary nebula NGC 7027 (Liu et al. 1996), and transitions up to $j = 19 \rightarrow 18$ of the Herbig Haro objects HH 52-53-54 and IRAS 12496-7650 in a nearby star-forming region (Nisini et al. 1996). The KOSMA 3m and IRAM 30m telescopes in Switzerland and Spain, respectively, performed observations of the low-j transitions of CO in the Rosette Molecular Complex (Schneider et al. 1998), while the *Odin Orbital Observatory* (Nordh et al. 2003) detected $j = 5 \rightarrow 4$ emission from the PDR of Orion KL (Persson et al. 2007). More recently, the *Herschel Space Observatory* (Pilbratt et al. 2010) observed the $j = 9 \rightarrow 8$ line towards Monoceros R2 (Pilleri et al. 2012) and high-j CO lines in the NGC 1333 low-mass star-forming region (Yildiz et al. 2010) with the Heterodyne Instrument for the Far-Infrared (HIFI, de Graauw et al. 2010). The Spectral and Photometric Imaging REceiver (SPIRE, Griffin et al. 2010) aboard *Herschel* has also probed the submillimeter molecular interstellar medium of M82 from $j = 4 \rightarrow 3$ up to $j = 13 \rightarrow 12$ (Panuzzo et al. 2010). The chemical and physical conditions of the above regions can be deduced from observed spectral lines, and accurate NLTE models of environments such as these require molecular collisional rate coefficients.

2.2 Scattering Formalism for Inelastic Collisions

Molecular scattering processes can be divided into three main categories: elastic collisions, which involve only simple momentum transfer, inelastic collisions, which also include a change in internal energy, and reactive collisions, where a change in chemical composition occurs. In all three categories the aim is to produce consistent scattering parameters between experiment and theory, but two main complications exist that hinder direct comparison. In experiment, the complication is that no simple two-body collision system can be observed in complete isolation. Instead of tracking the trajectory of a single particle colliding with another single particle, beams are used in collision experiments so that the parameter to compare with theory is the cross section, which is related to the probability for a certain process to occur. The complication in theory is that quantum mechanics must be included — the quantization of states and effects like interference or tunneling cannot be neglected. This leads to computationally expensive numerical solutions of difficult problems. However, at a molecular level, quantum mechanical effects may be small where classical physics is valid, and various approximations with the so called "semi-classical" approach can be used. This section details the theory of quantum non-reactive atom-diatom and inelastic scattering. The diatom-diatom formalism is quite similar and extends from our general case with extra degrees of freedom of the system. For a complete description of quantum scattering processes the reader is referred to Arthurs & Dalgarno (1960), "Molecular Collisional Theory" by Child (1996), and Chapters 4 and 5 of Flower (2007).

The general problem of scattering between an atom and diatom begins with the construction of an interaction potential energy surface (PES) between the atom and the molecule. There are several codes available to accomplish this feat, and one of the main codes is MOLPRO (Werner et al. 2010), which performs *ab initio* molecular electronic structure calculations along a given electronic PES (i.e., ground state). This set of energy points is then fit by a tractable function which can be incorporated into the scattering calculations as a subroutine. In practice, only the ground state electronic PES is calculated and transitions

between potential energy curves are not considered. This is the only step in our whole scattering calculation that involves approximation and is known as the Born–Oppenheimer approximation, or the 'adiabatic' approximation, because we consider only a single adiabatic potential energy surface. Although the technique of neglecting the coupling between the electronic and relative motions cannot be neglected when considering processes such as charge exchange or fine structure transitions, it is completely appropriate in rovibrational excitation calculations.

When describing the theory of molecular scattering it is natural to use the atomic system of units where the electron charge, electron mass, and reduced Planck constant equal unity; $e = m_e = \hbar = 1$. There are two main choices for the coordinate system, and when considering an atomic particle A incident on a vibrating diatom BC, it is natural to express the system in Jacobi coordinates as shown in Figure 2.1. These coordinates lie in what is referred to

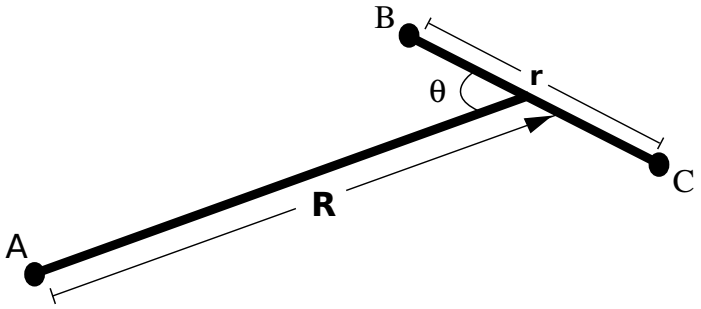

Figure 2.1: Definition of the Jacobi coordinates $\boldsymbol{r}$, $\boldsymbol{R}$, and θ.

as the 'body-fixed' frame (BF), referring to the fixed axis between the atom and the center of mass of the molecule. $\boldsymbol{r}$ is the BC intramolecular distance, $\boldsymbol{R}$ is the distance from the nucleus of atom A to the center of mass of the molecule BC (or internuclear distance), and θ is the angle between vector $\boldsymbol{R}$ and the BC bond axis, where linear A-B-C has an angle of zero degrees and linear A-C-B has a 180 degree angle. The adiabatic interaction potential energy surface often supplied by theoretical chemists is a function of the Jacobi coordinates $V(r, R, \theta)$ so the BF frame is natural for calculations. However, measurements made in the laboratory are easily expressed in the 'space-fixed' frame (SF), where the origin of the (x,y,z)

coordinates is the center of mass of the molecule BC. All derivations can be done in both frames and one can easily transform between them, however, the focus here will be on the BF frame. We define the polar coordinates of atom A in the SF frame as (R,Θ,Φ), where the coordinates (Θ,Φ) will give us the Z-axis of the BF frame. The polar coordinates of the molecule BC in the SF frame are (θ,ϕ) and in the BF frame are (θ',ϕ').

The basic scattering problem is the solution to the time-independent Schrödinger equation,

$$H\Psi = E\Psi, \tag{2.3}$$

where Ψ is the total wavefunction of the system, E is the barycentic energy of the system, and H is the Hamiltonian. When solving this equation numerically, it is advantageous to expand the total wavefunction in terms of functions of the radial and angular coordinates. First, we can expand the wavefunction of the molecule in the BF frame in terms of normalized spherical harmonics $Y_{j\Omega}$ which form a complete set of orthonormal functions of the polar angles (θ',ϕ'),

$$Y_{j\Omega}(\theta', \phi') = (-1)^{\Omega}\left[\frac{(2j+1)(l-\Omega)!}{4\pi(l+\Omega)!}\right]^{\frac{1}{2}} P_j^{\Omega}(\cos\theta')e^{i\Omega\phi'} \qquad (\Omega \geq 0), \tag{2.4}$$

where j is the angular momentum quantum number of the molecule, Ω is the projection of $\mathbf{j}$ on the BF Z-axis, l is the orbital angular momentum quantum number of the atom rotating about the molecule, and $P_j^{\Omega}(\cos'\theta')$ are the associated Legendre polynomials. Likewise, the SF spherical harmonics can be denoted by $Y_{jm}(\theta,\phi)$, with m as the projection of $\mathbf{j}$ on the SF axis.

To relate the spherical harmonics in the BF frame to those of the SF frame we must use the rotation matrix $\mathbf{D}$ which performs successive rotations through three Euler angles: α about the z-axis, β about the new y-axis, and γ about the new z-axis. These three rotations transform the SF (x,y,z) coordinate system into the BF (r,R,θ) system if we set the Euler angles to be the polar coordinates of A in the SF frame, i.e., $\alpha = \Theta$, $\beta = \Phi$, and $\gamma = 0$. The

rotation matrix is defined as

$$D^{j}_{m'm}(\alpha,\beta,\gamma) = \left\langle jm' \middle| e^{-i\alpha j_z} e^{-i\beta j_y} e^{-i\gamma j_z} \middle| jm \right\rangle \tag{2.5}$$

where the bra-ket notation of Dirac simplifies the spherical harmonics notation, $|jm\rangle = Y_{jm}(\theta,\phi)$, and j_y and j_z are components of the SF angular momentum operator,

$$\mathbf{j}^2 = j_x^2 + j_y^2 + j_z^2. \tag{2.6}$$

The SF spherical harmonics then relate to those of the BF frame by

$$Y_{j\Omega}(\theta',\phi') = \sum_m D^{j}_{m\Omega}(\Theta,\Phi,0) Y_{jm}(\theta,\phi), \tag{2.7}$$

and inversely

$$Y_{jm}(\theta,\phi) = \sum_\Omega D^{j*}_{m\Omega}(\Theta,\Phi,0) Y_{j\Omega}(\theta',\phi'), \tag{2.8}$$

where the asterisk denotes the complex conjugate. The functions in Equation (2.7) are eigenfunctions of $\mathbf{j}^2$ and j_Z in the BF frame with corresponding eigenvalues $j(j{+}1)$ and Ω, while the functions in Equation (2.8) are eigenfunctions of $\mathbf{j}^2$ and j_z in the SF frame with eigenvalues $j(j{+}1)$ and m.

We define $\mathbf{l}$ as the orbital angular momentum of the atom relative to the molecule and the total angular momentum to be $\mathbf{J}{=}\mathbf{j}{+}\mathbf{l}$. We can likewise determine the eigenfunctions of the orbital angular momentum operators $\mathbf{l}^2$ and l_z as $Y_{lm_l}(\Theta,\Phi)$ with corresponding eigenvalues $l(l{+}1)$ and m_l. However, to ease computation, we require eigenfunctions of the *total* angular momentum operators $\mathbf{J}^2$ and $\mathbf{J}_\mathrm{z}$. These can be formed by performing a transformation that connects the orbital and rotational bases via the Clebsch-Gordan coefficients,

$$C^{jlJ}_{mm_lM} = (-1)^{j-l+M}(2J+1)^{\frac{1}{2}} \begin{pmatrix} j & l & J \\ m & m_l & -M \end{pmatrix}, \tag{2.9}$$

where $M = m + m_l$ and the final term is the Wigner 3j-symbol. The eigenfunctions of the total angular momentum operators $\mathbf{J}^2$ and $\mathbf{J}_\mathrm{z}$ in the SF frame can then be given by multiplying the two sets of spherical harmonics together,

$$\mathcal{Y}_{jlJM}(\theta,\phi;\Theta,\Phi) = \sum_{mm_l} C^{jlJ}_{mm_lM} Y_{jm}(\theta,\phi) Y_{lm_l}(\Theta,\Phi). \tag{2.10}$$

Expressing the eigenfunctions of $\mathbf{J}^2$ and $\mathbf{J}_\mathrm{Z}$ in the BF frame requires the use of the aforementioned rotation matrix. As presented in Chapter 3 of Sakurai (1994), the spherical harmonics can be expressed in terms of the rotation matrix,

$$Y_{lm_l}(\Theta,\Phi) = \left(\frac{2l+1}{4\pi}\right)^{\frac{1}{2}} D^{l*}_{m_l0}(\Theta,\Phi,0). \tag{2.11}$$

Substituting this relation as well as Equation (2.7) into Equation (2.10) yields

$$\mathcal{Y}_{jlJM}(\theta,\phi;\Theta,\Phi) = \left(\frac{2l+1}{4\pi}\right)^{\frac{1}{2}} \sum_{mm_l\Omega} C^{jlJ}_{mm_lM} Y_{j\Omega}(\theta',\phi') D^{j*}_{m\Omega}(\Theta,\Phi,0) D^{l*}_{m_l0}(\Theta,\Phi,0). \tag{2.12}$$

The last two terms combine according to

$$D^{j}_{m\Omega}(\Phi,\Theta,0) D^{l}_{m_l0}(\Theta,\Phi,0) = \sum_{J'} C^{jlJ'}_{mm_lM} C^{jlJ'}_{\Omega 0\Omega} D^{J'}_{M\Omega}(\Theta,\Phi,0). \tag{2.13}$$

The Clebsch-Gordan coefficients form a unitary matrix whose elements are taken to be real by convention; the orthonormal conditions state that

$$\sum_{mm_l} C^{jlJ}_{mm_lM} C^{jlJ'}_{mm_lM'} = \delta_{JJ'}\delta_{MM'}. \tag{2.14}$$

The final result which relates the eigenfunctions of $\mathbf{J}^2$ in the BF frame to those of the SF frame is

$$\mathcal{Y}_{jlJM}(\theta,\phi;\Theta,\Phi) = \left(\frac{2l+1}{2J+1}\right)^{\frac{1}{2}} \sum_{\Omega} C^{jlJ}_{\Omega 0\Omega} \mathcal{Z}_{j\Omega JM}(\theta',\phi';\Theta,\Phi), \tag{2.15}$$

and the functions $\mathcal{Z}_{j\Omega JM}(\theta',\phi';\Theta,\Phi)$ are the eigenfunctions of $\mathbf{J}^2$ and J_{Z} in the BF frame,

$$\mathcal{Z}_{j\Omega JM}(\theta',\phi';\Theta,\Phi) = \left(\frac{2J+1}{4\pi}\right)^{\frac{1}{2}} D^{J*}_{M\Omega}(\Theta,\Phi,0) Y_{j\Omega}(\theta',\phi'). \tag{2.16}$$

In addition to applying the law of conservation of angular momentum to help solve the scattering problem, another useful property to use is symmetry. In the domain of quantum mechanics, space inversion is performed through the discrete parity operator $\mathbf{P}$, which transforms a right-handed coordinate system into a left-handed system. Since the hamiltonian is invariant under space inversion, the parity operator simply acts on the BF coordinates according to

$$\theta' \to \theta', \qquad \phi' \to \pi - \phi', \tag{2.17}$$

$$\Theta \to \pi - \Theta, \qquad \Phi \to \pi + \Phi. \tag{2.18}$$

Performing the parity operation on the eigenfunctions of $\mathbf{J}^2$ and J_Z we obtain

$$\mathbf{P}\mathcal{Z}_{j\Omega JM}(\theta',\pi-\phi';\pi-\Theta,\pi+\Phi) = \mathcal{Z}_{j\Omega JM}(\theta',\pi-\phi';\Theta,\Phi) = (-1)^J \mathcal{Z}_{j,-\Omega,JM}(\theta',\phi';\Theta,\Phi), \tag{2.19}$$

where, unfortunately, the change of sign in Ω indicates that $\mathcal{Z}_{j\Omega JM}(\theta',\phi';\Theta,\Phi)$ is not an eigenfunction of $\mathbf{P}$. However, we may form the needed eigenfunctions by performing a linear combination of these functions,

$$\mathcal{Z}_{j\bar{\Omega}\epsilon JM} = \frac{\left(\mathcal{Z}_{j\bar{\Omega}JM} + \epsilon \mathcal{Z}_{j,-\bar{\Omega},JM}\right)}{[2(1+\delta_{\bar{\Omega}0})]^{\frac{1}{2}}}, \tag{2.20}$$

where $\bar{\Omega} = |\Omega|$, the parameter $\epsilon = \pm 1$, and the denominator represents a normalization factor. One important note here is that for $\Omega = 0$ only $\epsilon = +1$ is allowed; there is only one parity when the projection of $\mathbf{j}$ on the BF axis is zero. Operating parity on the linear

combination created in Equation (2.20) yields

$$\mathbf{P}\mathcal{Z}_{j\bar{\Omega}\epsilon JM} = p\mathcal{Z}_{j\bar{\Omega}\epsilon JM}, \tag{2.21}$$

$$\mathbf{P}\mathcal{Z}_{j\bar{\Omega}pJM} = (-1)^J \epsilon \mathcal{Z}_{j\bar{\Omega}pJM}, \tag{2.22}$$

and we obtain the eigenvalues of the inversion operator, $p = (-1)^J\epsilon$. In $\mathcal{Z}_{j\bar{\Omega}pJM}$ we finally have angular eigenfunctions in which we can expand the total wavefunction.

We also separate the radial coordinates into translational $G(R)$ and vibrational $\chi(r)$ eigenfunctions, for the latter making use of the vibrational quantum number, ν. The expanded total wavefunction combines the radial and angular functions into the form

$$\Psi(r, \theta', \phi'; R, \Theta, \Phi) = \sum_{\nu j\bar{\Omega}pJM} \frac{G(\nu j\bar{\Omega}pJM|R)}{R} \frac{\chi(\nu j|r)}{r} \mathcal{Z}_{j\bar{\Omega}pJM}(\theta', \phi'; \Theta, \Phi). \tag{2.23}$$

It is this form of Ψ that we place into the Schrödinger equation (2.3), with the hamiltonian given by

$$H = h - \frac{\nabla_R^2}{2\mu} + V(r, R, \theta), \tag{2.24}$$

where $-\frac{\nabla_R^2}{2\mu}$ is the relative kinetic energy operator, ∇_R^2 is the Laplacian operator, and $\mu = m_A m_{BC}/(m_A + m_{BC})$ is the reduced mass of the system. The internal energy of the molecule at infinite separation from the atom is given by

$$h = -\frac{\nabla_r^2}{2m} + v(r), \tag{2.25}$$

where $m = m_B m_C/(m_B + m_C)$ is the reduced mass of the molecule. We can furthermore separate the kinetic energy operators into radial and angular parts,

$$-\frac{\nabla_r^2}{2m} = -\frac{1}{2mr}\frac{\partial^2}{\partial r^2} r + \frac{\mathbf{j}^2}{2mr^2} \tag{2.26}$$

and likewise

$$-\frac{\nabla_R^2}{2\mu} = -\frac{1}{2\mu R}\frac{\partial^2}{\partial R^2}R + \frac{\mathbf{l}^2}{2\mu R^2}. \tag{2.27}$$

The Schrödinger equation, therefore, becomes

$$\left[\frac{1}{2mr}\frac{\partial^2}{\partial r^2}r - \frac{\mathbf{j}^2}{2mr^2} + \frac{1}{2\mu R}\frac{\partial^2}{\partial R^2}R - \frac{\mathbf{l}^2}{2\mu R^2} + V(r,R,\theta) - E\right]\Psi = 0. \tag{2.28}$$

In the analysis of basis functions above, ϕ' was included for completeness, but thankfully the interaction between an atom and a linear molecule only depends on the Jacobi coordinates r, R, and θ' since the interaction potential is invariant under rotations of the molecular axis BC about $\mathbf{R}$.

The interaction potential can be expressed as an expansion over the complete set of functions of the angular coordinate

$$V(r,R,\theta) = \sum_{\lambda=0}^{\infty} v_\lambda(r,R)P_\lambda(\cos\theta), \tag{2.29}$$

where P_λ are the Legendre Polynomials, defined by the Rodrigues formula

$$P_l(x) = \frac{1}{2^l l!}\Big(\frac{d}{dx}\Big)^l (x^2-1)^l \qquad l = 0,1,2,\ldots. \tag{2.30}$$

Since the basis functions are orthonormal, we use the property

$$\int \mathcal{Z}^*_{j\bar{\Omega}pJM}(\theta',\phi';\Theta,\Phi)\mathcal{Z}_{j'\bar{\Omega}'p'J'M'}(\theta',\phi';\Theta,\Phi)d\theta' d\phi' d\Theta d\Phi = \delta_{jj'}\delta_{\bar{\Omega}\bar{\Omega}'}\delta_{pp'}\delta_{JJ'}\delta_{MM'} \tag{2.31}$$

to operate on Equation (2.28) and obtain

$$\left[\frac{\mathrm{d}^2}{\mathrm{d}R^2} + k^2_{\nu j}\right]G(\nu j\bar{\Omega}pJ|R) = 2\mu\sum_{\nu' j'\bar{\Omega}'} V_{\text{eff}}(\nu j\bar{\Omega},\nu' j'\bar{\Omega}';J|R)G(\nu' j'\bar{\Omega}'pJ|R), \tag{2.32}$$

where $k^2_{\nu j} = 2\mu(E-\epsilon_{\nu j})$, E is the total energy, $\epsilon_{\nu j} = \kappa^2_\nu/2m + B_\nu j(j+1)$ is the rovibrational

energy of the molecule, and B_ν is the rotational constant. The effective potential is given by

$$V_{\text{eff}}(r, R, \theta') = V(r, R, \theta') + \frac{\mathbf{l}^2}{2\mu R^2} \tag{2.33}$$

with matrix elements

$$V_{\text{eff}}(\nu j\bar{\Omega}, \nu' j'\bar{\Omega}'; J|R) = \left\langle \nu j\bar{\Omega} pJM \right| V(r, R, \theta') + \frac{\mathbf{l}^2}{2\mu R^2} \left| \nu' j'\bar{\Omega}' pJM \right\rangle . \tag{2.34}$$

The non-vanishing elements of the potential are given by

$$\left\langle \nu j\bar{\Omega} pJM \right| V(r, R, \theta') \left| \nu' j'\bar{\Omega} pJM \right\rangle = (-1)^{\bar{\Omega}} \sum_\lambda \frac{[(2j+1)(2j'+1)]^{\frac{1}{2}}}{(2\lambda+1)} C^{jj'\lambda}_{000} C^{jj'\lambda}_{\bar{\Omega},-\bar{\Omega},0} y_\lambda(\nu j, \nu' j'|R), \tag{2.35}$$

where

$$y_\lambda(\nu j, \nu' j'|R) = \int_0^\infty \chi^*(\nu j|r) v_\lambda(r, R) \chi(\nu' j'|r) \mathrm{d}r. \tag{2.36}$$

Note these elements are independent of M. The interaction potential cannot change the value of Ω but the centrifugal potential operator can, so we obtain two expressions for the non-vanishing elements of the centrifugal potential operator,

$$\left\langle j\bar{\Omega} pJM \right| \frac{\mathbf{l}^2}{2\mu R^2} \left| j\bar{\Omega} pJM \right\rangle = \frac{J(J+1) + j(j+1) - 2\bar{\Omega}^2}{2\mu R^2} \tag{2.37}$$

and

$$\left\langle j\bar{\Omega} pJM \right| \frac{\mathbf{l}^2}{2\mu R^2} \left| j, \bar{\Omega} \pm 1, pJM \right\rangle = \tag{2.38}$$

$$-(1+\delta_{\bar{\Omega}0})^{\frac{1}{2}}(1+\delta_{\bar{\Omega}\pm1,0})^{\frac{1}{2}} \frac{[J(J+1) - \bar{\Omega}(\bar{\Omega}\pm1)]^{\frac{1}{2}}[j(j+1) - \bar{\Omega}(\bar{\Omega}\pm1)]^{\frac{1}{2}}}{2\mu R^2}.$$

The ordinary differential equations (2.32) can be solved numerically and are called coupled-channel (CC) calculations because the matrix elements on the right-hand side couple the set of differential equations through the rovibrational states, or channels. The number of coupled

channels for a partial wave are given by

$$\sum_{j=0}^{j_\nu}(j+1) = (j_\nu+1)(j_\nu+2)/2 \tag{2.39}$$

and

$$\sum_{j=0}^{j_\nu} j = j_\nu(j_\nu+1)/2 \tag{2.40}$$

for + and − parities, respectively. It is nominal for the basis to include all j_ν levels below the collision energy, and one can easily see that as the kinetic energy of the collision rises, the quadratic dependence of the number of channels quickly escalates the computational time.

In solving the second order coupled differential equations one needs to impose two boundary conditions, 1) that the wavefunction is finite everywhere, and 2) asymptotic conditions, where the interaction potential vanishes and the scattering solution must match the asymptotic form

$$\Psi_{\text{asym}}(R,\theta) = \mathrm{e}^{\mathrm{i}kz} + f(\theta)\frac{\mathrm{e}^{\mathrm{i}kR}}{R}, \tag{2.41}$$

where $\mathrm{i} = \sqrt{-1}$ and $f(\theta)$ is called the scattering amplitude. We can then introduce the scattering matrix, or S matrix, that relates the incoming channels (νj) to the outgoing channels $(\nu' j')$ by means of the scattering amplitude,

$$f(\theta) = \frac{1}{2\mathrm{i}k_{\nu j}^2}\sum_{l=0}^{\infty}(2l+1)(S^{(l)}_{\nu\nu' jj'} - \delta_{\nu\nu' jj'})P_l(\cos\theta). \tag{2.42}$$

The S matrix contains all the information about the collision, and from it we can obtain both elastic and inelastic cross sections.

We define $\sigma_{\nu j\to\nu' j'}(E_{\nu j})$ as the degeneracy-averaged-and-summed integral cross section — a parameter that can be determined by both numerical solution and laboratory measurements — for a vibrational-rotational transition from an initial state νj to a final state $\nu' j'$ in the

CC formalism as

$$\sigma_{\nu j\to\nu' j'}(E_{\nu j}) = \frac{\pi}{(2j+1)k_{\nu j}^2}\sum_{J=0}^{J_{\max}}(2J+1)\sum_{l=|J-j|}^{J+j}\sum_{l'=|J-j'|}^{J+j'}|\delta_{\nu\nu'}\delta_{jj'}\delta_{ll'} - S^J_{\nu\nu' jj' ll'}(E_{\nu j})|^2, \quad (2.43)$$

where $E_{\nu j}$ is the relative kinetic energy of the initial channel.

If the number of channels is large and CC calculations are impractible, two main decoupling approximations are utilized to facilitate computation of the solutions to the scattering problem. The Infinite Order Sudden (IOS) approximation assumes that the collision happens "suddenly" and the molecule does not have time to rotate significantly, effectively reducing θ' to a constant. This approximation is applicable at a high collision energies when compared with the molecules' rotational excitation energies or in collisions with heavy molecules which have large rotational constants. This work does not make use of the IOS approximation.

Another decoupling scheme, the coupled states (CS) approximation first introduced by McGuire & Kouri (1974), was used in this dissertation for calculations containing high kinetic energies and large basis sets where CC calculations are not feasible. Also termed *J*-*j* or centrifugal coupling, the CS approximation reduces the computation expense by modifying the matrix elements in Equations (2.35) - (2.38) to neglect the Coriolis coupling between different values of $\bar{\Omega}$, effectively decoupling the differential equations (see also Florian et al. 2004). Within this formalism the integral cross section is given by

$$\sigma_{\nu j\to\nu' j'}(E_{\nu j}) = \frac{\pi}{(2j+1)k_{\nu j}^2}\sum_{J=0}^{J_{\max}}(2J+1)\sum_{\bar{\Omega}=0}^{\bar{\Omega}_{\max}}(2-\delta_{\bar{\Omega}0})|\delta_{\nu\nu'}\delta_{jj'} - S^{J\bar{\Omega}}_{\nu\nu' jj'}(E_{\nu j})|^2, \quad (2.44)$$

where $\bar{\Omega}_{\max}$ is equal to $0, 1, 2, \ldots$, max(J,j). Unlike CC calculations where each partial wave has a large number of channels denoted by Equations (2.39) and (2.40), for each value of J there are j terms to compute, but these terms each have a smaller number of channels to calculate in the S matrix, greatly reducing computational expense by about an order of magnitude.

Once the state-to-state cross sections are calculated, inelastic collisional rate coefficients are readily obtained by averaging the cross sections over a Boltzmann distribution of collision energies,

$$k_{\nu j\to\nu' j'}(T) = \left(\frac{8k_{\rm B}T}{\pi\mu}\right)^{1/2} \frac{1}{(k_{\rm B}T)^2} \int_0^\infty \sigma_{\nu j\to\nu' j'}(E_{\nu j}) \exp(-E_{\nu j}/k_{\rm B}T) E_{\nu j} dE_{\nu j}. \qquad (2.45)$$

The theory of atom-diatom collisions is laid out fully and formally, so we now turn to programming and the development of numerical techniques used in obtaining inelastic collisional rate coefficients.

2.3 A Computational Approach to Scattering

Several powerful programming packages are available to solve the quantum mechanical close-coupling calculations, such as MOLSCAT (Hutson & Green 1994), HIBRIDON (Alexander et al. 2011), MOLCOL (Flower, Bourhis, & Launay 2000), and TwoBC (Krems 2006). The research detailed below utilize the nonreactive scattering program MOLSCAT (modified by Valiron & McBane (2008) and N. Balakrishnan [private communication]) for atom-diatom rovibrational inelastic cross section calculations and TwoBC to obtain cross sections from the full 6-dimensional diatom-diatom PES.

Building on the serial MOLSCAT code, I developed a hybrid message-passing, shared-memory rovibrational capable program (VRRMM — Vibrational/Rotational Rich Man's MOLSCAT) to speed up the molecular collisional excitation cross section calculations. Solving the full close-coupled second-order differential equations for the S matrix typically scales as the number of equations cubed, N^3, and when considering systems with large rotational (> 50) and vibrational momenta (> 5) or relatively high energy (~ 1 eV), a large number of basis functions and partial waves are needed for the cross sections to converge. A significant number of basis functions causes the computation time to dramatically increase. With VRRMM, the diagonalization of large matrices in the solution can be quickly performed

on several OpenMP threads (manipulating one matrix across several cpu cores), and each partial wave in the expansion can be computed as a separate MPI process. Essentially, the cross section calculation for one energy with VRRMM now takes only as long as a single partial wave. For high energies and the systems considered here, this is equivalent to one wallclock day with VRRMM instead of one wallclock month with serial MOLSCAT.

VRRMM has been used to calculate rovibrationally resolved cross sections for He-CO and H-CO and the wallclock speedup has been significant. To calculate the wallclock speedup, one simply divides the wallclock time for execution on a single processor by that of a run on multiple threads,

$$S_{\text{threads}} = \frac{T_{\text{single}}}{T_{\text{threads}}}. \tag{2.46}$$

Furthermore, VRRMM obeys Amdahl's law, which imposes a upper limit on the increased performance of a parallel program compared to the serial version. The maximum decrease in runtime can never exceed $1/p_{\text{seq}}$, where p_{seq} is the intrinsically sequential fraction of the program. Figure 2.2 shows the execution time for VRRMM when it uses a single processor and multiple shared memory OpenMP threads. The calculations are for a single partial wave, parity combination ($J = 24$, parity $= +$) for He colliding with CO($\nu = 1$,$j = 0$) at a collision energy of 100 cm^{-1}. The number of channels in the calculation is 648.

The best speedup achieved is 2.5 using 6 processors. Implementing 2 processors does not make a substantial difference in the execution time. This is most likely due to the linear algebra math libraries — the Lapack routines optimize at 3 threads, which exhibits significant speedup. Performing calculations on 4 threads actually slows the performance, and using ≥ 5 processors does not make a substantial difference compared to the performance on 3 threads. Considering the submission of jobs to the queue system on the CSP and Georgia Advanced Computing Resource Center (GACRC) clusters, 3 threads are easily scheduled, and are therefore recommended when running VRRMM.

Even more significant than the speedup obtained by shared memory threads is that obtained by adding MPI processes within VRRMM. Message-passing interface (MPI) com-

munications allow a program to send out routines to other cores for execution. In VRRMM, each partial wave and parity combination, henceforth called a (J,p) pair, is executed as an MPI process. This means, in theory, that the wallclock calculation can be reduced to the time it takes to execute a single partial wave (initialization is trivial when compared to calculating the S matrix). The smallest partial waves have fewer than 100 channels, but for a large basis set the number of channels increases to over 2000. Instead of performing each (J,p) pair in succession, they can now all be computed simultaneously. Figure 2.3 shows the execution times for VRRMM when it uses a single processor, 30 MPI processes, and 80 processes. The calculations are for the collision of He with CO($\nu = 1$,$j = 0$) at a collision energy of 100 cm^{-1}. The log scale of the plot shows that the calculation time decreases $\propto 1/x$. The speedup for the $J_{\max} = 24$ and $J_{\max} = 40$ calculations are 34.1 and 26.4, respectively. A large number of calculations can be a daunting task for serial MOLSCAT, but the power of VRRMM to combine MPI processes with OpenMP threads can lead to speedups ≥ 85!

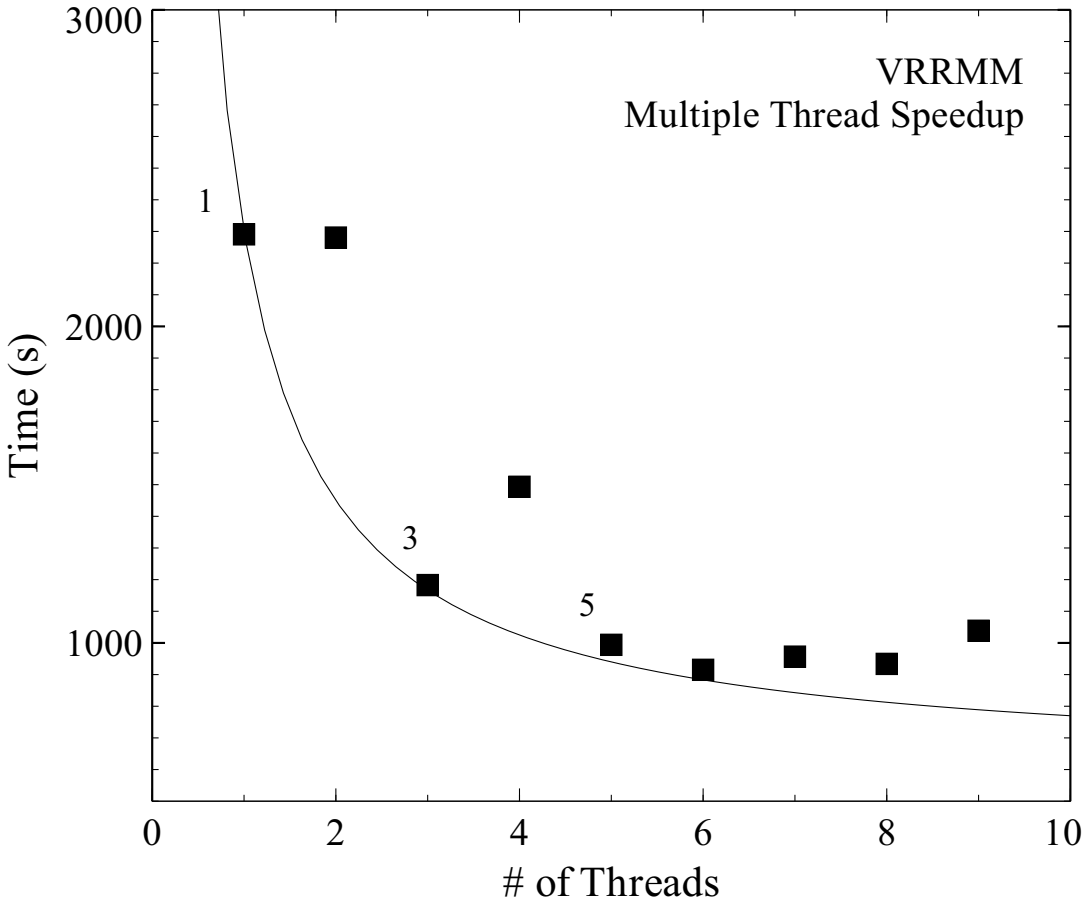

Figure 2.2: Wallclock execution times for one partial wave, parity combination (J,p) calculated by VRRMM with differing numbers of OpenMP shared memory threads. The solid line indicates Amdahl's law.

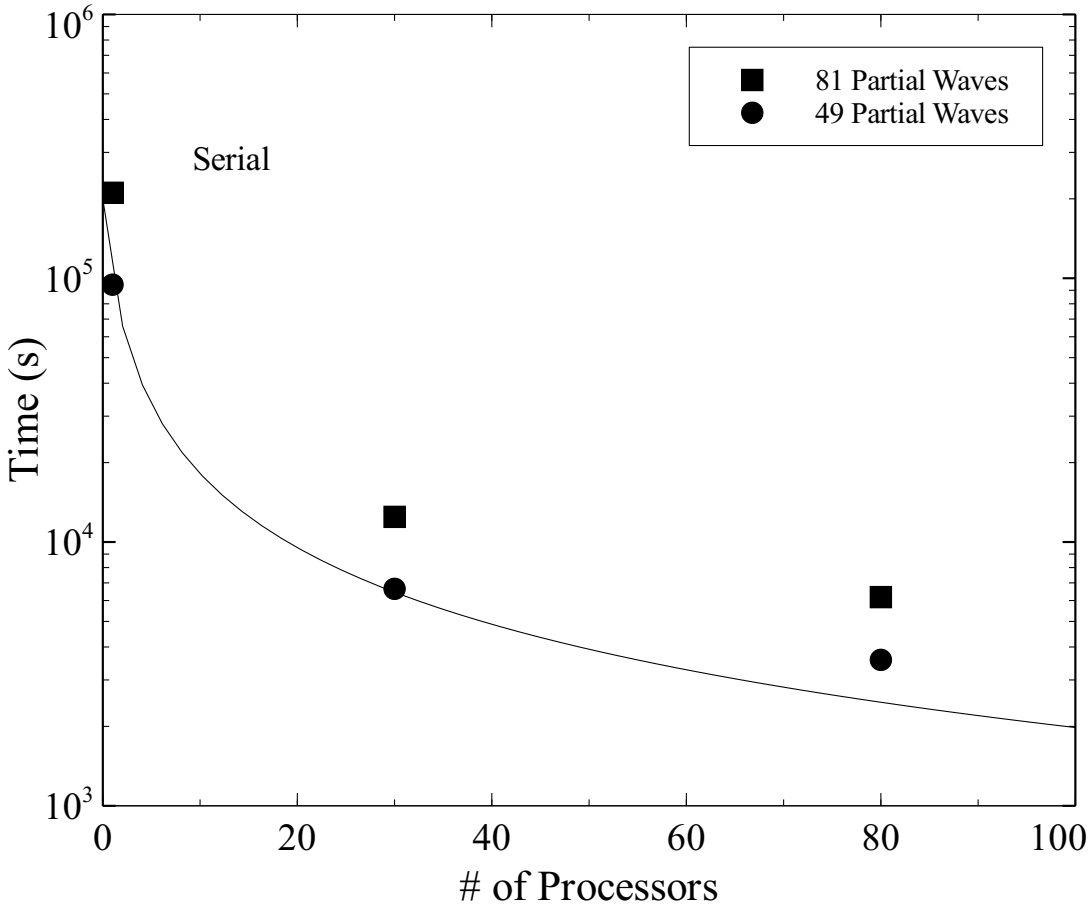

Figure 2.3: Wallclock execution times for the collision of He and CO($\nu = 1$, $j = 0$) at $E = 100$ cm^{-1} calculated by VRRMM serially and with 30 and 80 single-threaded MPI processes for one value of parity. The squares denote $J_{\max} = 24$ while the circles indicate $J_{\max} = 40$. Note the log scale of the ordinate. The solid line indicates Amdahl's law.

2.4 H_2-H_2 Collisions

The scattering theory behind an atom and a diatomic molecule can be extended to diatom-diatom collisions by including the extra degress of freedom of the system. The number of degrees of freedom of a two-body collisional system of three or more atoms is given by $3N - 6$, where N is the number of atoms involved in the collision. Therefore, there are only three degrees of freedom in an atom-diatom system, but it doubles to six in a diatom-diatom system such as H_2-H_2 or H_2-HD. These extra degrees of freedom can be expressed in the Jacobi coordinates shown in Figure 2.4, where $\boldsymbol{R}$ is the distance from the center of mass of molecule AD to the center of mass of molecule BC, $\boldsymbol{r}_1$ is the AD intramolecular distance, $\boldsymbol{r}_2$ is the BC intramolecular distance, θ_1 is the angle between vector $\boldsymbol{R}$ and the AD bond axis, θ_2 is the angle between vector $\boldsymbol{R}$ and the BC bond axis, and ϕ is the toroidal angle between the planes of AD and BC. This more complicated scattering problem now has CC and CS calculations which scale as $J^6_{\max}$ and $J^4_{\max}$, respectively, where $J_{\max}$ is the maximum size of the rovibrational basis set.

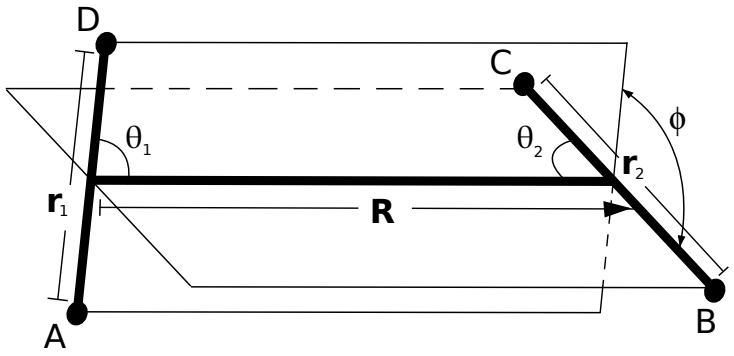

Figure 2.4: Definition of the Jacobi coordinates $\boldsymbol{R}$, $\boldsymbol{r}_1$, $\boldsymbol{r}_2$, θ_1, θ_2, and ϕ for a system with 6 degrees of freedom.

The program TwoBC (Krems 2006) was modified in a similar fashion as VRRMM to be parallelized by angular momentum and parity, and similar excellent speedup is attained. The modified code will be used in the future to benchmark interstellar observations from the Space Telescope Imaging Spectrograph (STIS) and Cosmic Origins Spectrograph (COS) aboard the *Hubble Space Telescope* (*HST*). Rate coefficient calculations for the H_2-H_2 system

will extend the the collisional rate coefficients of low-lying rovibrational levels from $\nu = 2$ (Fonseca dos Santos et al. 2013) up to initial states $\nu = 4$ and $j = 20$ for collisions due to both para and ortho moieties. Furthermore, the first initial rovibrational calculations for H_2-HD collisional excitation are planned for the future. Full dimensional 6D quantum calculations are now more feasible thanks to the parallelization of TwoBC.

2.5 H-CO Collisions[1]

We now move on to implementing VRRMM in calculations of the H-CO system. The earliest analysis of H-CO collisions was performed by Chu & Dalgarno (1975), who used a short-range, semi-empirical potential joined with a long-range Buckingham potential to calculate cross sections via two close-coupling formulations. The resulting cross sections were found to be comparable to those of H_2-CO for small Δj. The Maxwellian-averaged rate coefficients were calculated for the temperature range of $5 - 150$ K. The following year, quantal calculations were carried out by Green & Thaddeus (1976) over the same temperature range, but with a new semi-empirical potential and strikingly different results. These collisional rate coefficients were typically an order of magnitude smaller than those of Chu & Dalgarno (1975), and small Δj transitions, i.e., $|\Delta j| = 1$ or 2, were reported to have much larger rate coefficients when compared to large Δj transitions. The small magnitude of the H-CO rate coefficients obtained by Green & Thaddeus (1976) led to the neglect of H as a collider in CO emission modeling.

The next interaction PES for the H-CO system followed a more sophisticated level of theory using *ab initio* calculations for the surface (Bowman et al. 1986, hereafter called BBH). These calculations employed the Dunning & Hay (1971) valence double-zeta contractions of the Huzinaga (1971), (9s,5p) sets of carbon- and oxygen-centered primitive Gaussians and used the (4s,2s) contraction with a scale factor of 1.2 for hydrogen. Restricted Hartree-Fock calculations were carried out, followed by configuration interaction computations including

[1]Based on Walker et al. (2015)

all singly- and doubly-excited configurations. The resulting empirically corrected potential was used in dynamics calculations using a cubic spline interpolation. Subsequent coupled-channel scattering calculations were carried out on this PES by Lee & Bowman (1987) who first noticed the propensity for even-Δj transitions for inelastic scattering.

Another surface was constructed by Werner et al. (1995), hereafter WKS, to see if new experimental results could be more closely reproduced. The *ab initio* electronic structure calculations were performed with the MOLPRO program package (Werner et al. 2010) using the internally contracted multireference configuration interaction (icMRCI) method. Resonance energies and widths from the WKS surface agreed with experimental data (Keller et al. 1996), but striking differences were apparent in the collision cross sections obtained using the BBH and WKS surfaces (Green et al. 1996). The cross sections on the newer WKS surface, especially for low-j pure rotational transitions, yielded larger values than those calculated on the BBH surface. Balakrishnan, Yan, & Dalgarno (2002) obtained similar results when they used both the BBH and the WKS surfaces to compute collisional rate coefficients for temperatures in the range 5 to 3000 K. The discrepancy in the CO($j = 1 \rightarrow 0$) transition was the largest. However, Balakrishnan, Yan, & Dalgarno (2002) performed explicit quantum-mechanical scattering calculations with the WKS PES for the first eight pure rotational transitions (using the coupled-channel framework) and first five vibrational levels (in the infinite order sudden [IOS] approximation), and this complete set of rate coefficients has been extensively used in astrophysical models.

Shepler et al. (2007) revisited H-CO scattering by introducing two new rigid-rotor PESs and computing cross sections on each surface at collision energies of 400 and 800 cm^{-1}. One *ab initio* surface was calculated using the coupled cluster method with single and double excitations and a perturbative treatment of triple excitations [CCSD(T)] employing the frozen core approximation (Purvis & Bartlett 1982). Restricted Hartree-Fock orbitals were used for the open-shell calculations and the spin-restrictions were relaxed in the solution of the coupled cluster equations [R/UCCSD(T)] (Knowles, Hampel, & Werner 1994). The other

PES was computed using the complete active space self-consistent field (CASSCF) (Knowles & Werner 1985) and icMRCI (Werner & Knowles 1989) method with the aug-cc-pVQZ basis set[2] for H, C, and O by Woon & Dunning (1994) as implemented in the MOLPRO program. Their results for both potentials are more similar to Green & Thaddeus (1976) and it was recommended that the rate coefficients calculated by Balakrishnan, Yan, & Dalgarno (2002) using the inaccurate WKS surface be abandoned. Based on this recommendation, astrophysical models using the overestimated rate coefficients should also be reexamined. The most recent set of H-CO calculations were performed by Yang et al. (2013b) which extended the calculations of Shepler et al. (2007) on the MRCI rigid-rotor PES. State-to-state rotational deexcitation cross sections and rate coefficients from initial states $j = 1 - 5$ in the ground vibrational state to all lower j' levels were computed.

In this section, we report new quantum scattering calculations for rotational deexcitation transitions of CO induced by H using the new three-dimensional (3D) interaction PES of Song et al. (2013). This 3D *ab initio* PES uses the spin-unrestricted open-shell single and double excitation coupled-cluster method with perturbative triples [UCCSD(T)] with molecular orbitals from restricted Hartree-Fock calculations (RHF). Electronic structure calculations were performed with the MOLPRO 2000 package (Werner et al. 2010) and 3744 interaction energies were included in the fit. When compared to previous PESs, the new 3D surface uses the most sophisticated level of theory and is the most accurate available for scattering calculations. State-to-state cross sections for collision energies from 10^{-5} to 15,000 cm^{-1} are computed for CO($\nu = 0$, j) deexcitation from initial states $j = 1 - 45$ to all lower j' levels. While coupled-channel and coupled-states calculations, in full-dimension, are performed for $j = 1 - 5$, 10, 15, 20, 25, 30, 35, 40, and 45, scaling approaches are used to estimate the rate coefficients for all other intermediate rotational states. Rate coefficients for temperatures

[2]In computational quantum chemistry, a linear combination of atom-centered Gaussian basis functions is often used to create the atomic orbitals that describe the wavefunction of an electron in an atom. The basis sets developed by T. Dunning and collaborators converge toward the infinite basis set limit and are widely used in correlated molecular calculations. The notation aug-cc-pVQZ indicates a correlation-consistent polarized valence-only quadrupole-zeta set augmented by added diffuse functions.

ranging from 1 to 3000 K were computed and are compared with previous scattering results obtained on earlier surfaces. The astrophysical implications of new rotational deexcitation rate coefficients are illustrated.

2.5.1 Computational Parameters

Inelastic scattering calculations were performed on the most current three-dimensional PES of the H-CO complex in the ground state ($\widetilde{X}^2A'$) (Song et al. 2013). Computations were carried out using the CC method for kinetic energies below 1000 cm^{-1}. From 1000 cm^{-1} to 15,000 cm^{-1} the CS approximation was utilized. We treated hydrogen as a structureless atom and allowed the bond length to vary for CO. The full 3D surface is used in the calculations; at no point is the CO bond length fixed nor a rigid-rotor approximation made. The interaction potential was expressed as $V(r,R,\theta)$, where r is the CO intramolecular distance, R the distance from the CO center of mass to the H nucleus, and θ the angle between vector R and the CO bond axis, where linear C-O-H has an angle of zero degrees and $\theta = 180^\circ$ for linear H-C-O (see Figure 2.1). The potential was expanded according to Legendre polynomials of order λ. The radial dependence of the potential used a 20-point Gauss-Hermite quadrature over r to represent CO stretching. The angular dependence of the potential was expanded according to Equation 2.29 with $\lambda_{\max} = 20$ and a 22-point Gauss-Legendre quadrature. The reduced mass of the H-CO system is $\mu = 0.97280$ u.

The quantum-mechanical close-coupling calculations were performed using VRRMM, described in Section 2.3. The modified log-derivative Airy propagator of Alexander & Manolopoulos (1987) with variable step size was used to solve the coupled-channel equations. The propagation was carried out from $R = 1$ a_0 to a maximum distance of $R = 100$ a_0, where a_0 is the atomic unit of length (the Bohr radius). For calculations with initial state $j < 25$, the basis set included 31 rotational levels in the ground vibrational state of CO. For initial states $j \geq 25$ the basis sets were expanded so that at least $5 - 10$ closed rotational levels were also included. Only pure rotational transitions within the $\nu = 0$ vibrational level are

reported here. A convergence study was performed with excited vibrational levels in the basis set, but the addition of higher vibrational levels yielded results within 2%. A sufficient number of angular momentum partial waves were included to ensure convergence to within 10% for the largest state-to-state cross sections. For the low energy range, 10^{-5}–10^{1} cm^{-1}, $J_{\max}$ was increased each decade resulting in the values 2, 4, 8, 12, 14, and 20 being added to the value of initial j, respectively, while converged cross sections for energies from $10-49$, $50-95$, $100-900$, $1000-9000$, and $10,000-15,000$ cm^{-1} were calculated by increasing $J_{\max}$ by 26, 30, 40, 50, and 60, respectively. State-to-state cross sections for collision energies from 10^{-5} to 15,000 cm^{-1} were computed for CO($\nu = 0$,j) deexcitation from initial state $j = 1-5$, 10, 15, 20, 25, 30, 35, 40, and 45 to all lower j' levels. Deexcitation rate coefficients ranging from 1 to 3000 K were obtained by thermally averaging the cross sections over the kinetic energy distribution.

2.5.2 H-CO Scattering Results

Before scattering calculations were carried out, we compared the RHF-UCCSD(T) three-dimensional *ab initio* PES of Song et al. (2013) with the two-dimensional rigid-rotor MRCI and CCSD(T) surfaces of Shepler et al. (2007). The Legendre terms of the RHF-UCCSD(T) PES agree well with the CCSD(T) terms; the similar high level of theory in both CCSD(T) calculations is expected to yield a more accurate potential than the lower-level MRCI calculations (see Figure 2.5). When comparing the CCSD and RHF-UCCSD calculations, the higher order λ terms are small ($\lesssim$0.1 cm^{-1}, a factor of $\sim$200 smaller compared to $\lambda = 0$) and most likely do not have a significant effect on the cross sections. The values of the Legendre expansion terms of the MRCI potential are all greater than those of the RHF-UCCSD(T) and CCSD(T) PESs. The feature seen in the MRCI results near $R = 10$ a$_0$ is due to the poor quality of fitting where the long–range and short–range regions are joined. Since the depth and location of the van der Waals well may strongly influence rotationally inelastic scattering, the behavior of the three interaction potentials was closely examined in the vicinity of

the van der Waals well. Figure 2.6 shows a contour plot of the long-range behavior of the interaction potential of Song et al. (2013) with the CO bond length fixed at the equilibrium distance of $r_e = 2.1322$ a_0. The positions and values of the local and van der Waals minima on the three interaction PESs were calculated and are shown in Table 2.1. The van der Waals well of the MRCI potential is significantly different from that of the CCSD(T) and RHF-UCCSD(T) being both shallower and at a larger internuclear distance. The differences in van der Waals well depth and anisotropies of the surfaces lead to differences in the scattering results.

Table 2.1: Minima of the interaction PESs.

PES	$r_{CO}(a_0)$	$V_{min}(cm^{-1})$	$R(a_0)$	θ (degrees)
Global minimum:[a]				
MRCI[b]	2.20	-6934.052	3.01	145.5
CCSD(T)[b]	2.1322	-5817.161	3.00	144.7
RHF-UCCSD(T)[c]	2.1322	-5832.994	3.01	144.8
RHF-UCCSD(T)[c]	2.20	-7256.805	3.02	144.8
van der Waals minimum:				
MRCI	2.20	-19.934	7.21	110.8
CCSD(T)	2.1322	-34.677	6.87	108.1
RHF-UCCSD(T)	2.1322	-35.269	6.86	108.0
RHF-UCCSD(T)	2.20	-36.296	6.84	108.5

[a] The term "global" is used loosely here since r_{CO} has been frozen at an unoptimized distance to ease direct comparison with the previous 2D surfaces.
[b] Shepler et al. (2007)
[c] Song et al. (2013)

Figure 2.7 shows state-to-state pure rotational H-CO rate coefficients from initial state CO($j = 5$) to indicated lower states j'. The largest rate coefficients of CO($5 \rightarrow 3$) as calculated by Chu & Dalgarno (1975), Green & Thaddeus (1976), and Balakrishnan, Yan, & Dalgarno (2002) are shown. Rate coefficients from Yang et al. (2013b) on the MRCI PES of Shepler et al. (2007) are also shown. The rate coefficients in this work agree well with those of Chu & Dalgarno (1975) and Yang et al. (2013b). On average, rate coefficients of Green & Thaddeus (1976) are less than those of this work by around an order of magnitude,

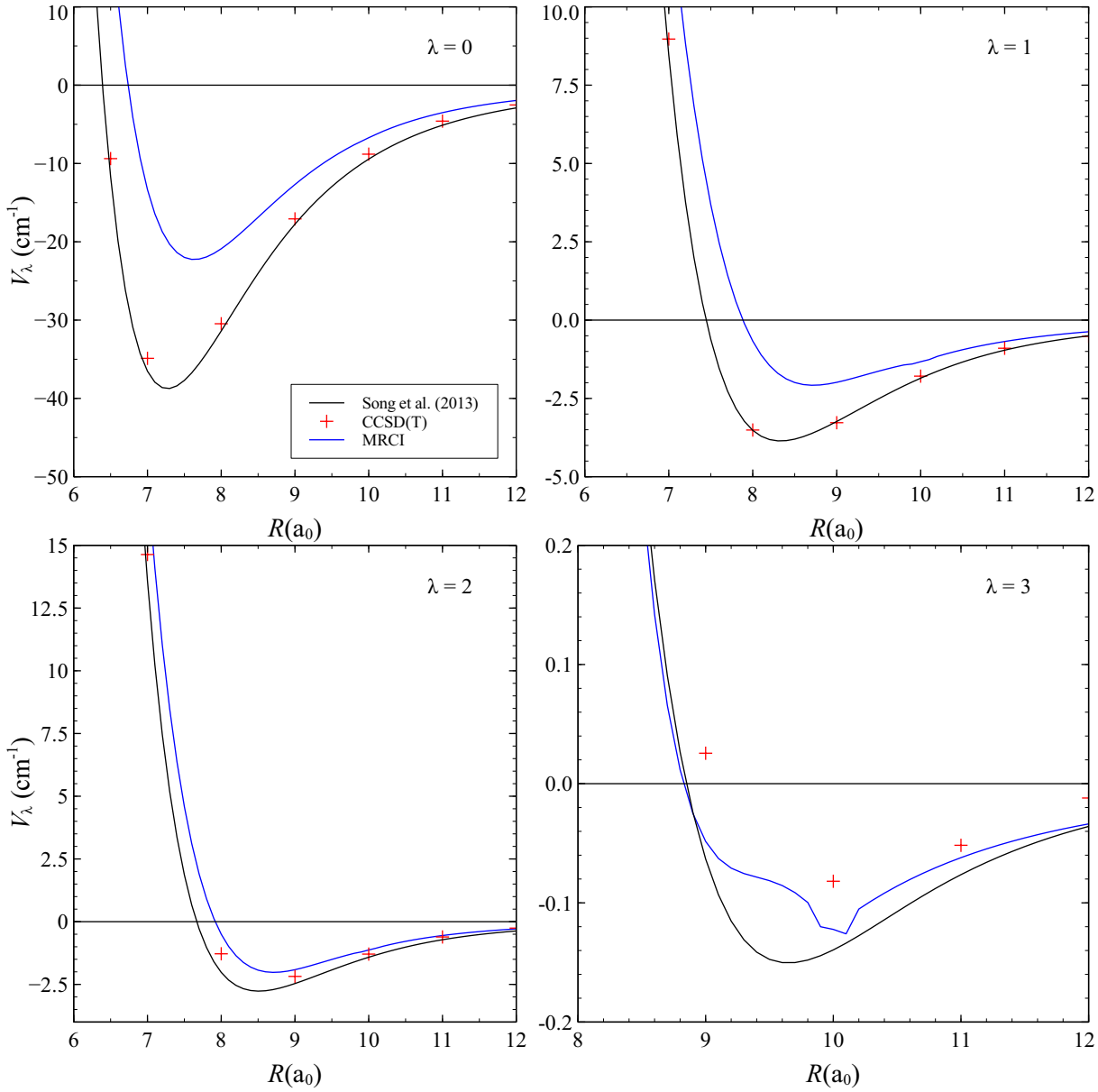

Figure 2.5: The first four Legendre expansion terms $V_\lambda(R)$ near the van der Waals well of the H-CO PES with the CO intermolecular distance fixed at $r = 2.20$ a$_0$ for MRCI and the equilibrium bond length $r_e = 2.1322$ a$_0$ for the CCSD(T) and RHF-UCCSD(T) surfaces.

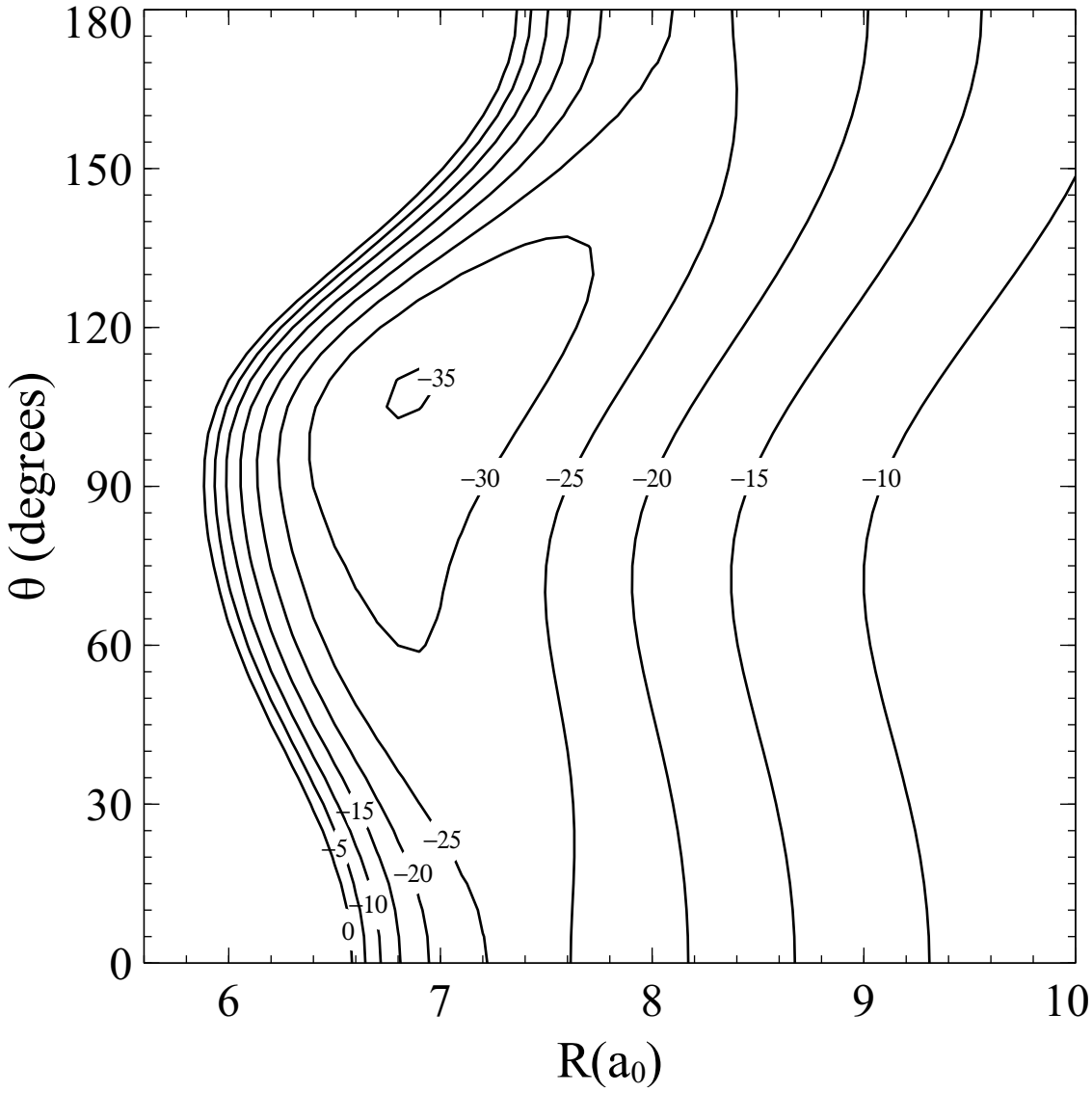

Figure 2.6: The long-range behavior of the interaction potential of Song et al. (2013) with V_{HCO} in cm^{-1} and r fixed at the equilibrium bond length $r_e = 2.1322$ a_0.

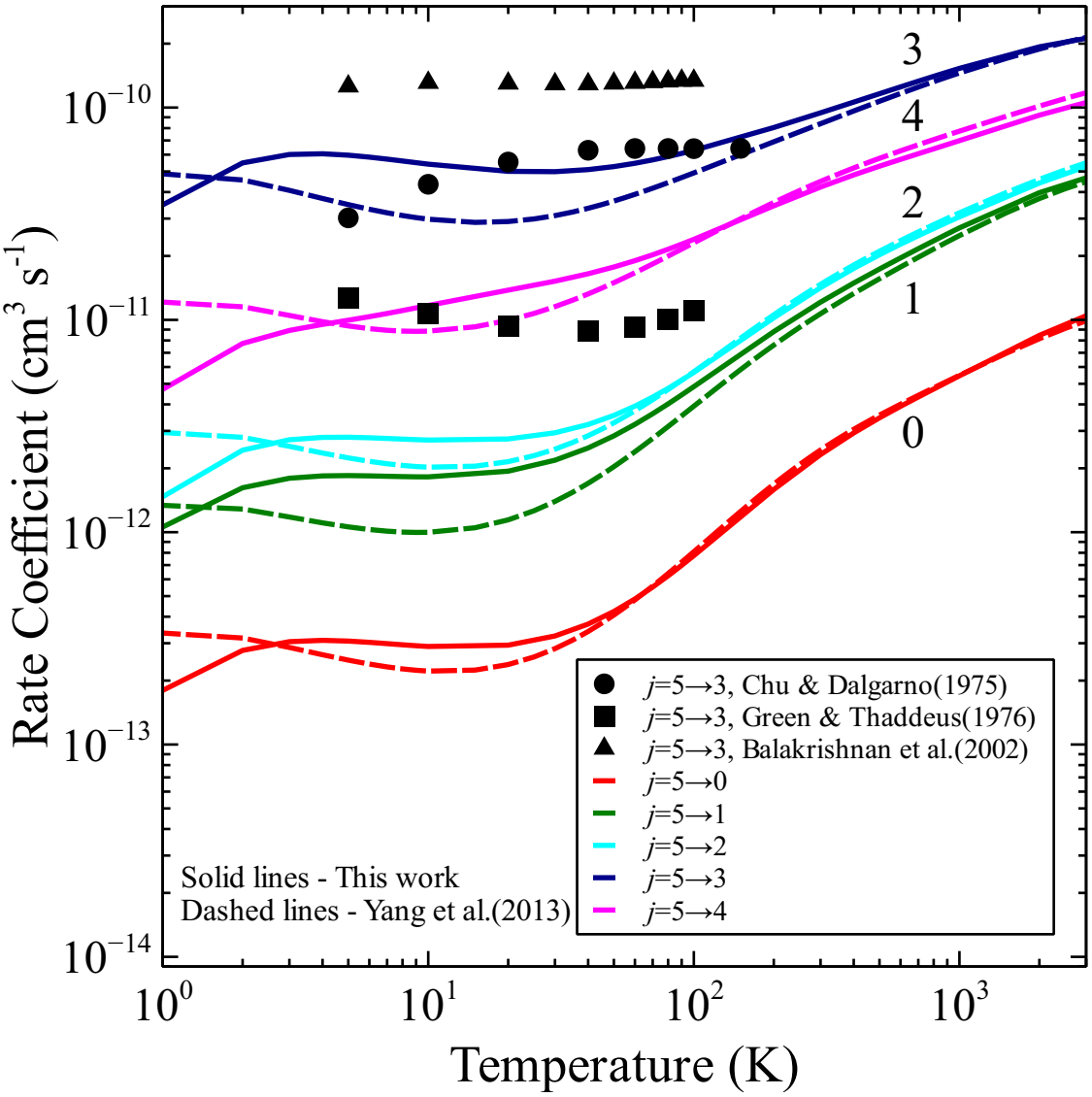

Figure 2.7: State-to-state pure rotational rate coefficients due to H collisions from initial state CO($j = 5$) to indicated lower states j' from this work using the Song et al. (2013) PES, and from Yang et al. (2013b) on the MRCI PES of Shepler et al. (2007). Previous rate coefficient calculations of Chu & Dalgarno (1975), Green & Thaddeus (1976), and Balakrishnan, Yan, & Dalgarno (2002) on other surfaces are also shown for the dominant transition $j = 5 \rightarrow 3$.

while the values from Balakrishnan, Yan, & Dalgarno (2002) are around twice as much as ours. Although the CO($5 \rightarrow 3$) transition is highlighted here, the results are typical for other state-to-state transitions as well.

Figures 2.8 and 2.9 present sample results from our computations of cross sections and rate coefficients, respectively, from initial state j=10 to all final states j'. In general, the cross sections for j'=0 are smallest and then increase with increasing j' up to the dominating transition where $|\Delta j| = |j' - j| = 2$ after which they decrease. Since CO is near-homonuclear, odd-Δj transitions are suppressed and the transitions follow an even-Δj propensity. At 1000 cm^{-1}, the difference between the CC and CS cross sections is less than $\sim$5%, except for the largest changes in Δj where the differences are typically $\sim$10%.

While the quenching from selected high rotational states is explicitly calculated, a zero-energy scaling technique (ZEST) is used to predict state-to-state rate coefficients for all intermediate states. Figure 2.10 shows the total quenching and state-to-state cross sections calculated at 10^{-5} cm^{-1} as a function of increasing j. The total quenching rate coefficient in the ultracold limit (collision energy of 10^{-5} cm^{-1}) is fairly constant for $j > 10$. Note that $\Delta j = -2$ dominates for low initial j, as expected, but at $j \sim 22$, $\Delta j = -1$ begins to dominate. From these ultracold state-resolved quenching rate coefficients, we estimated the rate coefficients for all temperatures following the procedure introduced in Yang et al. (2006), but modified here. The unknown rate coefficient for a transition from j to $j - \Delta j$ for any temperature T [$k(j, j - \Delta j; T)$] can be estimated based on the rate coefficients from calculated transitions for other initial rotational states, for example, larger j (i.e., above, j_A) or smaller j (i.e., below, j_B) [$k(j_A, j_A - \Delta j; T)$ and $k(j_B, j_B - \Delta j; T)$, respectively] and calculated ultracold rate coefficients for the transitions above, below, and the desired according to

$$k(j, j - \Delta j; T) = k(j, j - \Delta j; T = 0) \frac{w_A k(j_A, j_A - \Delta j; T) + w_B k(j_B, j_B - \Delta j; T)}{w_A k(j_A, j_A - \Delta j; T = 0) + w_B k(j_B, j_B - \Delta j; T = 0)}. \tag{2.47}$$

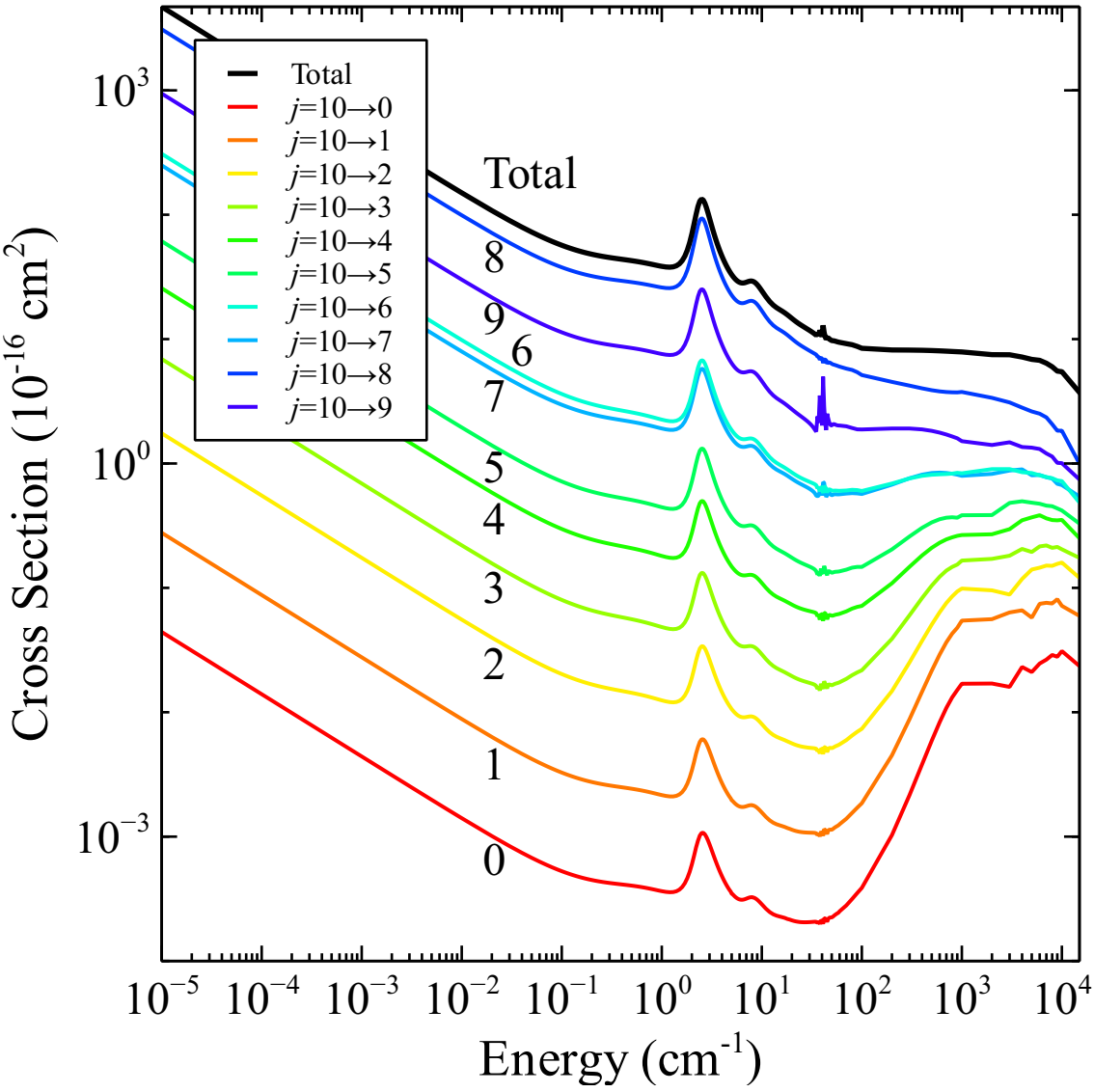

Figure 2.8: State-to-state pure rotational deexcitation cross sections due to H collisions from initial state CO($j = 10$) to all lower states j'.

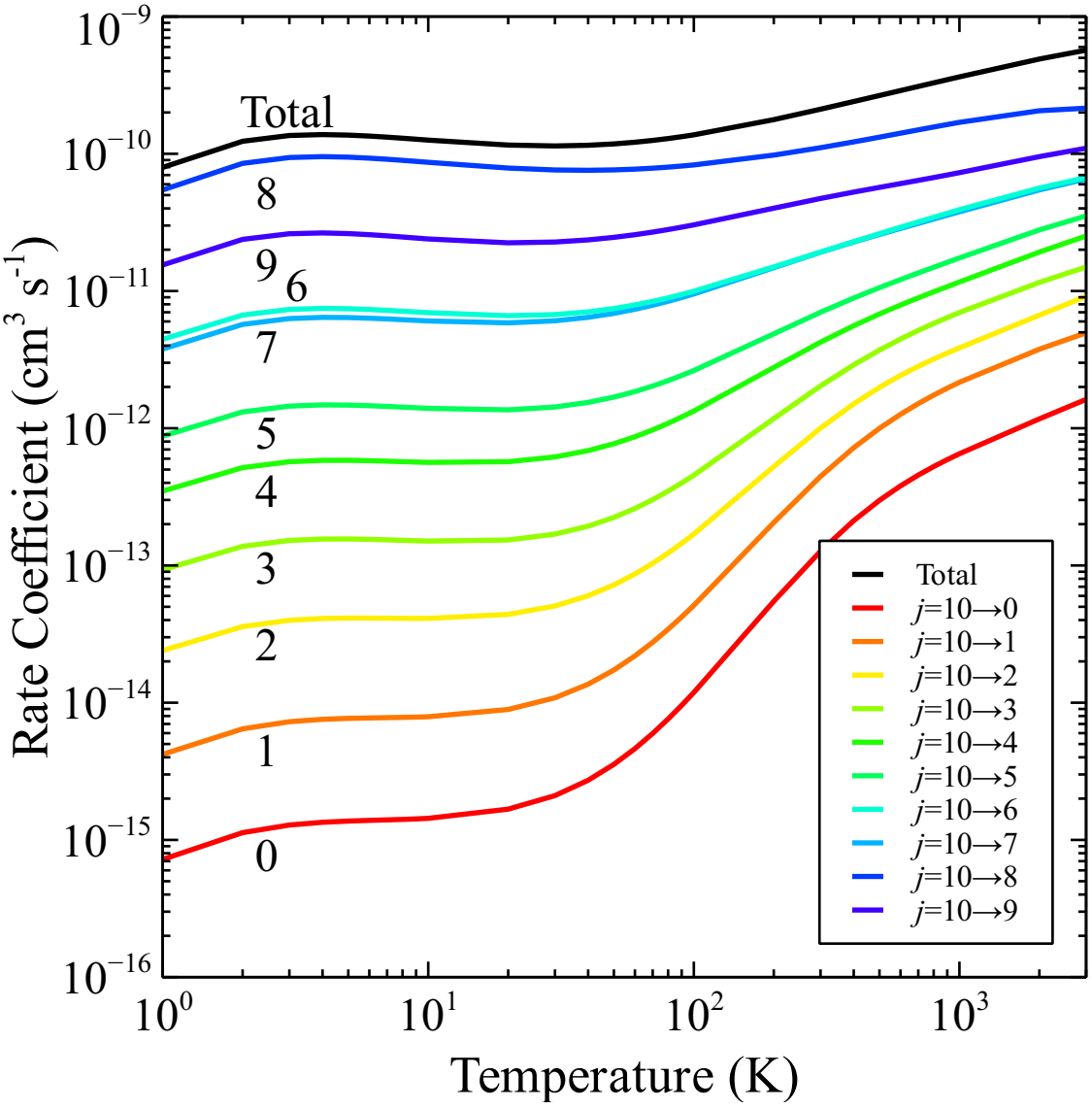

Figure 2.9: State-to-state pure rotational deexcitation rate coefficients due to H collisions from initial state CO($j = 10$) to all lower states j'.

Weights w_A and w_B for the calculated rate coefficients were determined by considering the change in initial j in the desired transition when compared to the states above and below according to the equations

$$w_A = \frac{j - j_B}{j_A - j_B} \qquad w_B = \frac{j_A - j}{j_A - j_B}. \tag{2.48}$$

For example, the predicted $j = 16$ rate coefficients used calculated transitions from $j = 20$ and $j = 15$ and weights $w_A = 0.2$ and $w_B = 0.8$. The cross sections at ultracold energies (i.e., 10^{-5} cm^{-1}) are easily calculated and simply multiplied by the velocity of the system (obtained from the kinetic energy of the collision) to obtain the $T \sim 0$ rate coefficients. A comparison of this zero-energy scaling technique with explicit calculations is given in Figure 2.11 for initial state $j = 4$. The predicted rate coefficients agree well with the calculated values, although in this case transitions from $j = 3$ and $j = 5$ are equally weighted and a slight underestimate of the $j = 4 - 2$ transition occurs. Likewise, a comparison is done for $j = 15$ and is given in Figure 2.12. Given the high accuracy of the current PES, any uncertainty remaining in the explicit cross section calculations is likely due to the adoption of the CS approximation and limited basis set sizes for collision energies above 1000 cm^{-1}. Otherwise, the interpolation formula introduces the largest source of uncertainty.

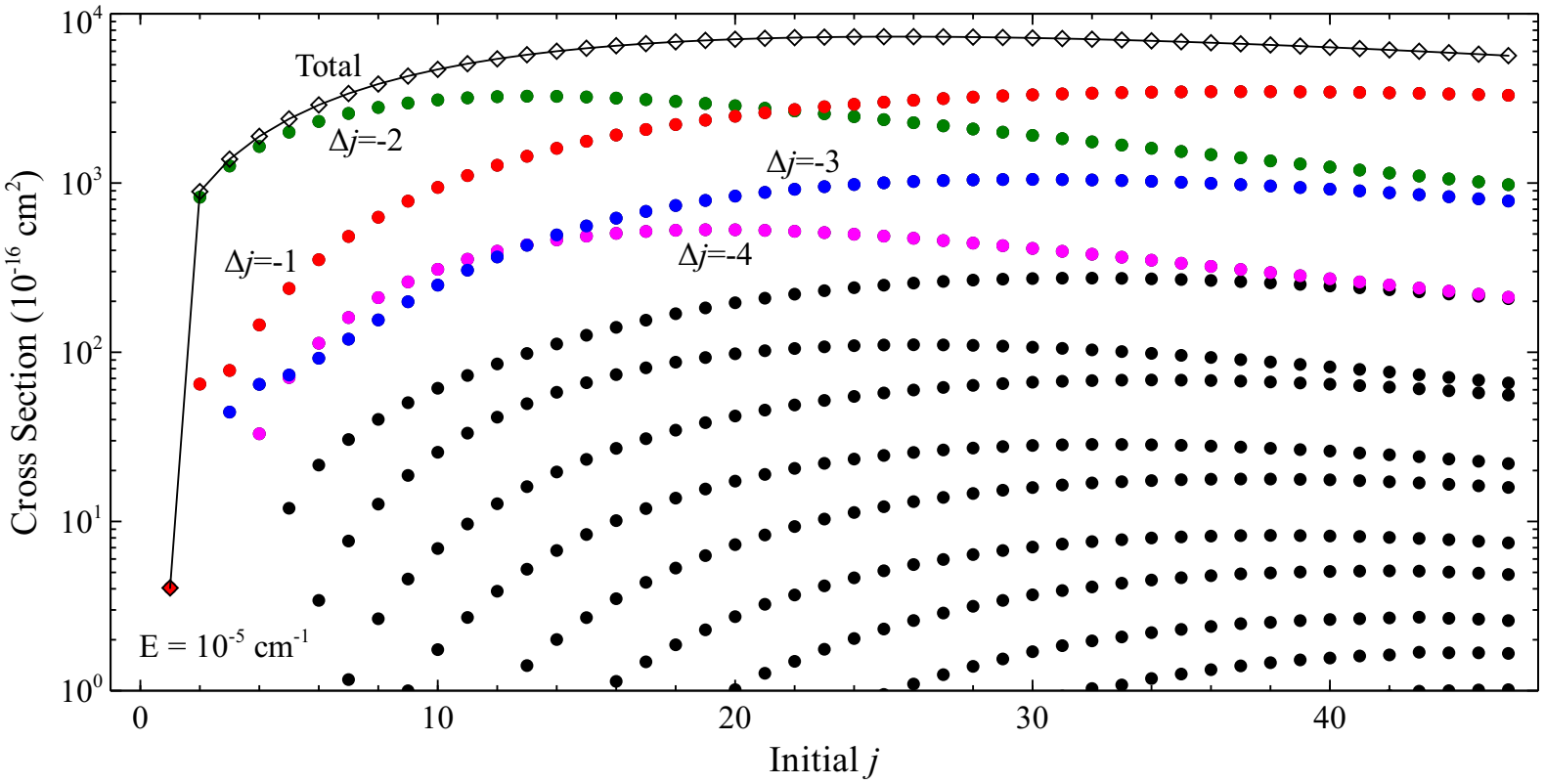

Figure 2.10: Ultracold state-resolved cross sections as a function of increasing j for the H-CO system. Circles indicate state-to-state cross sections while diamonds indicate total quenching cross sections. Each series (circles) correspond to different values of Δj, decreasing from the top at the far right as $\Delta j = -1, -2, -3, -4, ...$ (red, green, blue, magenta).

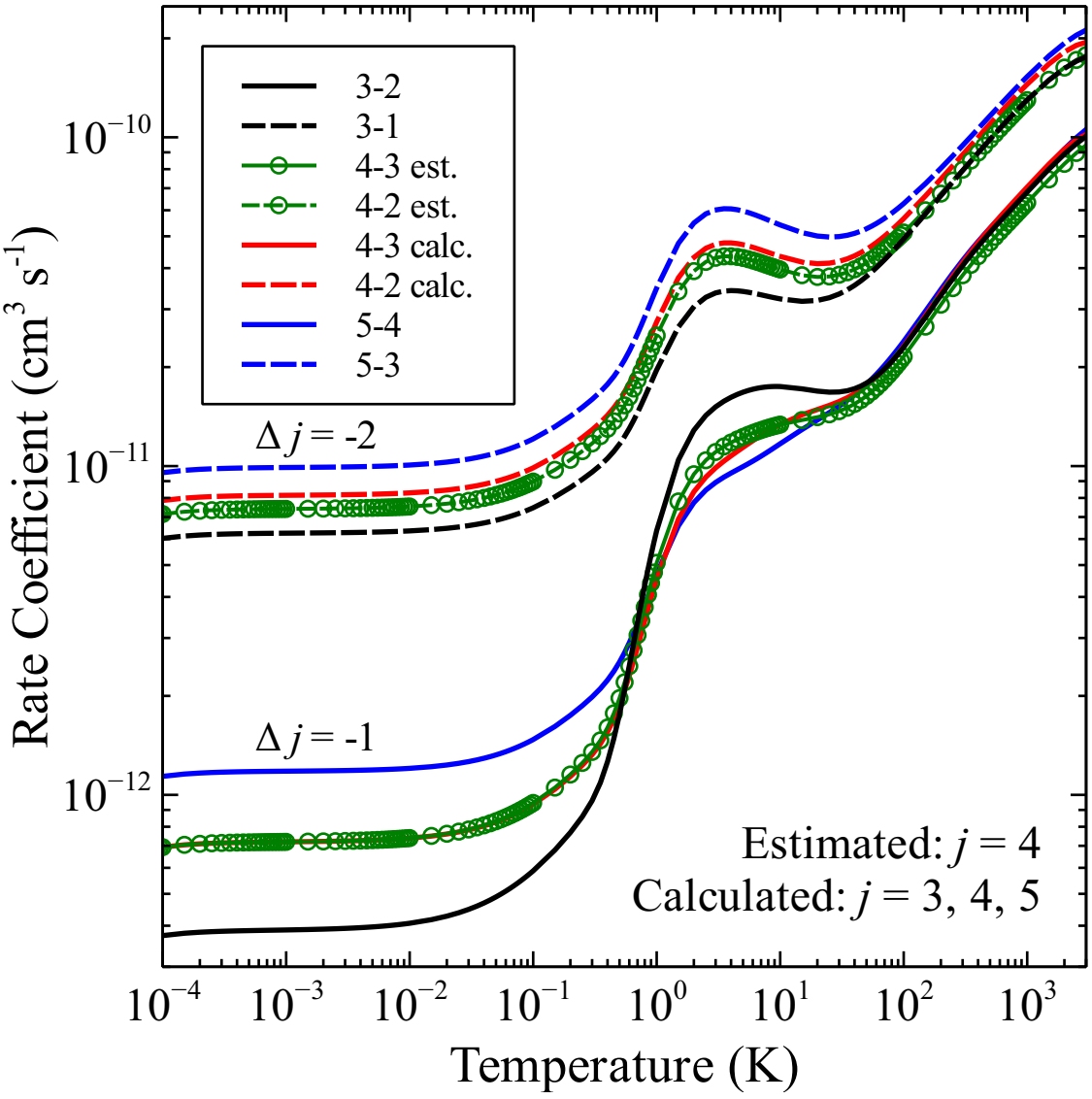

Figure 2.11: A comparison of the zero-energy scaling technique with explicit calculations of the largest deexcitation rate coefficients for initial state $j = 4$. Solid lines indicate $\Delta j = -1$ while dashed lines are $\Delta j = -2$. Initial states are: $j = 3$ (black), $j = 4$ estimated from Equation (2.47) (green with symbols), $j = 4$ explicitly calculated (red), and $j = 5$ (blue).

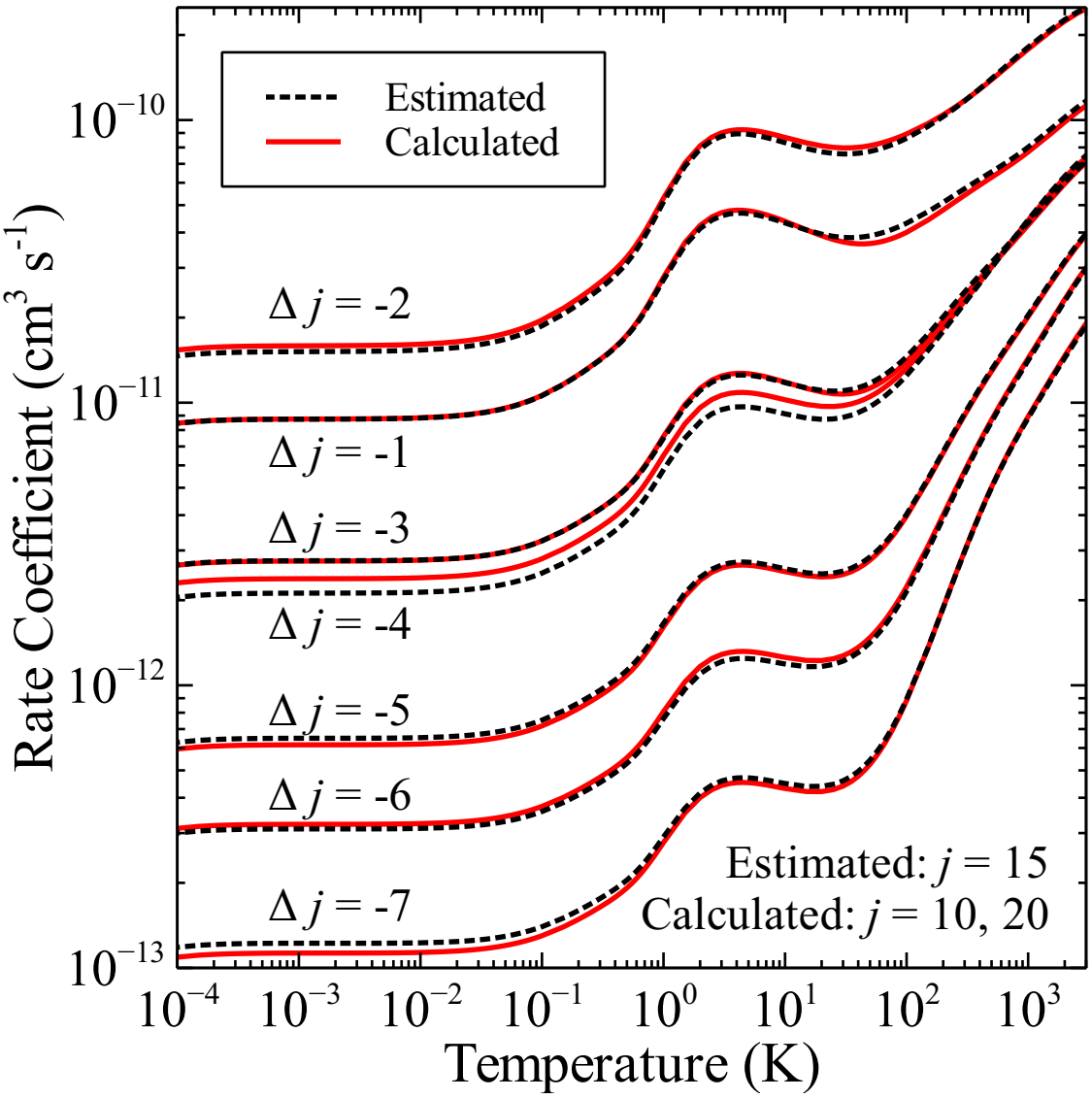

Figure 2.12: A comparison of the zero-energy scaling technique (dashed black lines) with explicit calculations (solid red lines) of the largest deexcitation rate coefficients for initial state $j = 15$.

2.5.3 Astrophysical Applications

The cross sections and/or rate coefficients calculated in this work can be obtained online.[3] These high-j pure rotational rate coefficients are especially useful as input data for codes developed to solve for level populations. One such code is RADEX (van der Tak et al. 2007), which can perform a non-LTE analysis of interstellar line spectra. The reliable rate coefficients calculated in this work also will help extract more accurate astrophysical conclusions from current models. Recently, Thi et al. (2013) modeled protoplanetary disks (PPDs) adopting the H-CO rate coefficients computed by Balakrishnan, Yan, & Dalgarno (2002). These rate coefficients are based on an inaccurate interaction surface, so the conclusions of Thi et al. (2013) may be compromised. Furthermore, Thi et al. (2013) extrapolated the rate coefficients to higher temperatures. Our rate coefficients extend the range in temperature from previous studies up to 3000 K; therefore extrapolation in this case would not be necessary. It is expected that our reliable and comprehensive rate coefficients would lead to more accurate astrophysical models of PDRs, PPDs, and other molecular environments.

In the PPD models of Thi et al. (2013), they note that pure rotational transitions of CO probe the entire disk, while the warm inner regions are probed by rovibrational transitions. Further, the abundance of atomic hydrogen is high in the CO line-emitting region. In particular, it is typically greater than 10^6 cm^{-3} throughout the disk, except near the midplane and at the disk surface. Assuming that H collisions and spontaneous emission dominate the CO rotational populations, the critical density for each rotational level j can be estimated following Osterbrock & Ferland (2006) (see Equation 2.2) and are displayed in Figure 2.13 (a similar figure for para-H_2 collisions can be found in Yang et al. 2010). Except near the inner disk where temperatures exceed 500 K and the density is greater than 10^8 cm^{-3}, levels for $j \geq 15$ will not be in LTE. Infrared and UV-fluorescence pumping may also contribute resulting in supra-thermal CO rotational populations.

[3]Rate coefficient data in the Leiden Atomic and Molecular Database (LAMDA, Schöier et al. 2005) format, as well as cross section data can be obtained at www.physast.uga.edu/amdbs/excitation/.

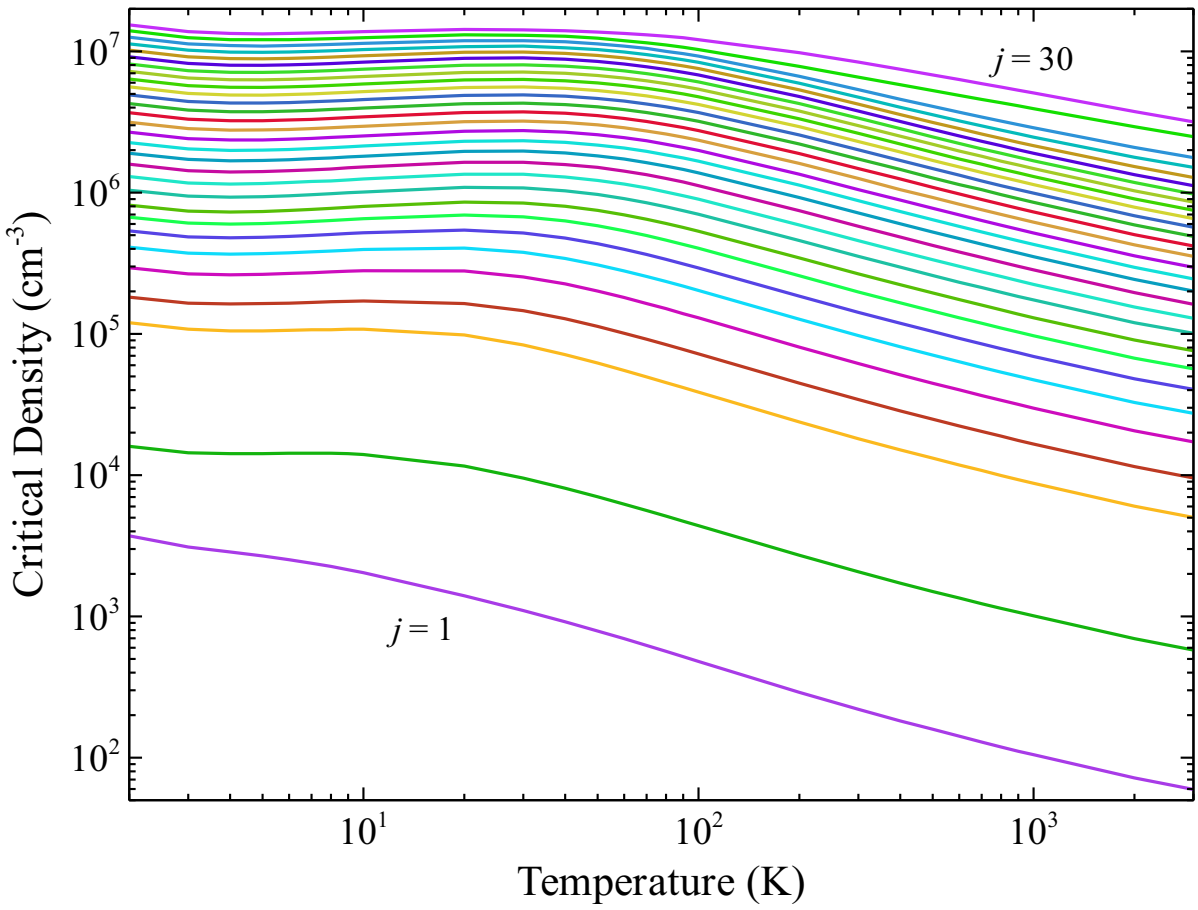

Figure 2.13: Critical densities for CO($\nu = 0, j$) due to H collisions as a function of gas temperature T.

Chapter 3

Collider-Mass Scaling in Collisional Excitation

The modeling of astrophysical observations requires a large variety of fundamental data, and as explained in section 2.1, collisional excitation rate coefficients are one class of data greatly needed to produce realistic results. Although computational advancements are improving the rate at which these data are calculated, in many cases collisional excitation rates for systems of astrophysical interest are not available — this is especially true when considering the colliders H and H_2. The past few decades have seen more molecular collisional calculations performed using He as a collider due to its relative ease of computation, but H and H_2 are the dominant neutral species in many astrophysical regions, not He. In light of this, it is common practice to approximate unknown collisional rate coefficients for the colliders H, H_2, and other species from the known rate coefficients of another collider, i.e., He (e.g., Schöier et al. 2005; van der Tak 2011). This procedure, which we refer to as "standard" reduced-mass scaling, dates back to Green et al. (1978), who predicted excitation rates of H_2 to be about 30% higher than He rates in collisions with H_2CO, and later computed broadening cross sections from line-width parameters and predicted state-to-state excitation rate coefficients for H_2O-CO collisions (Green 1993). These predictions were compared to theoretical He-CO rate coefficients and it was found that rate coefficients for excitation by water were related to those by He through the square root of the ratio of the systems' reduced masses. Note, however, that these experimental data limited the predictions to room temperature and above, yet this "standard" reduced-mass scaling technique has been used at lower temperatures and the results have been extensively applied to inelastic rate coefficients.

Recently, the standard reduced-mass scaling approach has been applied to excitation of the molecules SiS (Lique et al. 2008) and SO_2 (Cernicharo et al. 2011) and has produced inaccurate results (see also Roueff & Lique 2013; van der Tak 2011). The vast amount of data on CO, and its importance in astrophysics, leads us to use it as a test molecule to explore more physically reasonable analytical and scaling approximations to estimate unknown rate coefficients. This chapter delves deeper into the standard reduced-mass scaling technique and investigates the effects of interaction potential energy surface and reduced mass on computed rate coefficients.

3.1 The (In)validity of Reduced-Mass Scaling[1]

Quantum mechanical close-coupling calculations were performed using the nonreactive scattering program MOLSCAT (Hutson & Green 1994) with the modern PESs of Shepler et al. (2007), Jankowski & Szalewicz (2005), and Heijmen et al. (1997) for H-, H_2-, and He-CO, respectively. The scattering cross sections were computed for kinetic energies between 10^{-6} and 10^3 cm^{-1} within the rigid-rotor approximation with CO in its vibrational ground state and H_2 it is rovibrational ground state, i.e. para-H_2. Only para-$H_2(j = 0)$ is considered in our study; ortho-H_2 and para-$H_2(j > 0)$ rate coefficients obtained via any mass scaling approach from He data are unlikely to be accurate due to the molecules' lack of spherical symmetry.

The main assumption of standard reduced-mass scaling is the statement that the cross section as a function of E_k is independent of the collider. It is then argued that the rate coefficients between He-CO and H_2-CO, for example, scale as the square root of the ratio of reduced masses according to

$$k^{H_2}_{j\to j'}(T) = \left(\frac{\mu_{He}}{\mu_{H_2}}\right)^{\frac{1}{2}} k^{He}_{j\to j'}(T), \tag{3.1}$$

[1]Based on Walker et al. (2014)

as deduced from the prefactor of Equation (2.45). Here $k^X_{j\to j'}(T)$ is the state-to-state rate coefficient for collider X, μ_X is the reduced mass for the X-CO system, and a prefactor of $\sim$1.4 is obtained in this case. As an illustration, Figure 3.1 displays the calculated rate coefficients for the deexcitation of CO(j=1) with the colliders He and H_2. The estimated H_2 rate coefficients using the standard reduced-mass scaling relation, Equation (3.1), are seen to deviate significantly from the explicitly computed values, especially for $T \lesssim 100$ K.

Although the standard reduced-mass scaling relation has been widely adopted (e.g., Schöier et al. 2005; Adande, Edwards, & Ziurys 2013; Matsuura et al. 2014), it actually assumes not that the cross section $\sigma(E_k)$, but that the integral in Equation (2.45), is independent of the collider. However, this assumption is not generally valid because: (a) the cross section depends on the adopted PES and (b) the kinetic energy depends on μ. In cases where Equation (3.1) has produced reasonable estimates, it may have been the result of fortuitous cancellation of the effects due to points (a) and (b).

To explicitly illustrate the failings of Equation (3.1) and to explore other more physically-motivated approaches, we investigate three tracks: i) the behavior of inelastic cross sections as a function of system parameters, ii) prediction of $k_{j\to j'}(T)$ adopting analytical relations for the cross section, and iii) an alternative scaling approach based on the well-depth of the PES. To test the dependence of the cross section on μ and the PES, a series of calculations were performed for the collider masses H, H_2, ^{3}He, and ^{4}He with CO on each of the H-CO, H_2-CO, and He-CO PESs. In Figure 3.2, the cross sections, which were all calculated on the He-CO PES, are seen to depend significantly on the adopted μ. In addition to changes in the cross section slopes and magnitudes, the positions of quasibound resonances vary, especially for H_2 and He compared to H. Figs. 3.3–3.4 show similar calculations for calculations of the four reduced masses on the H_2-CO and H-CO PESs, respectively. Figure 3.5 shows the results of calculations using the H-CO reduced mass on the three different PESs.

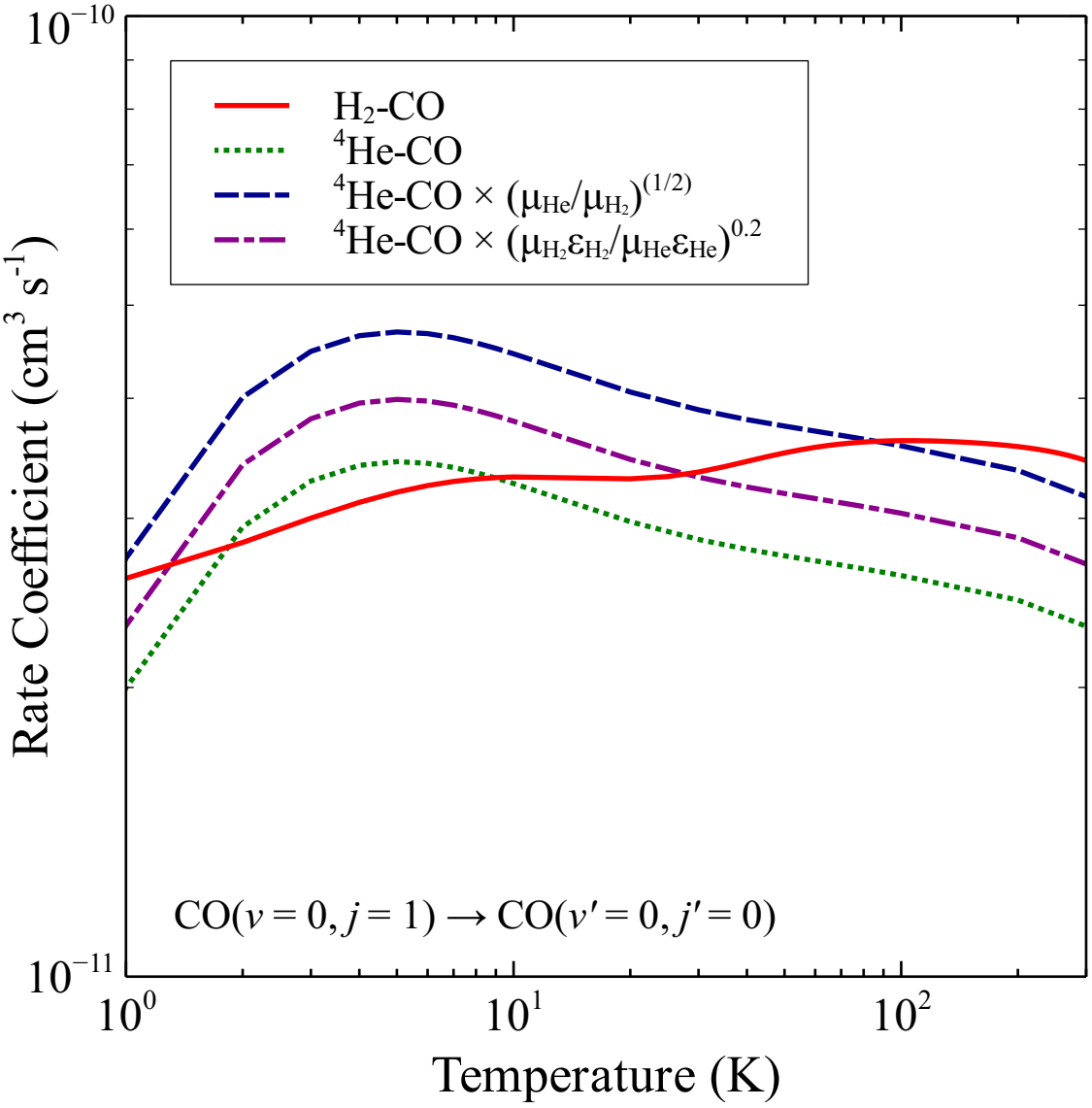

Figure 3.1: Rate coefficients for the deexcitation of CO(j=1) with the colliders He and para-H_2 and estimated values for H_2 via standard reduced-mass scaling and reduced-potential scaling.

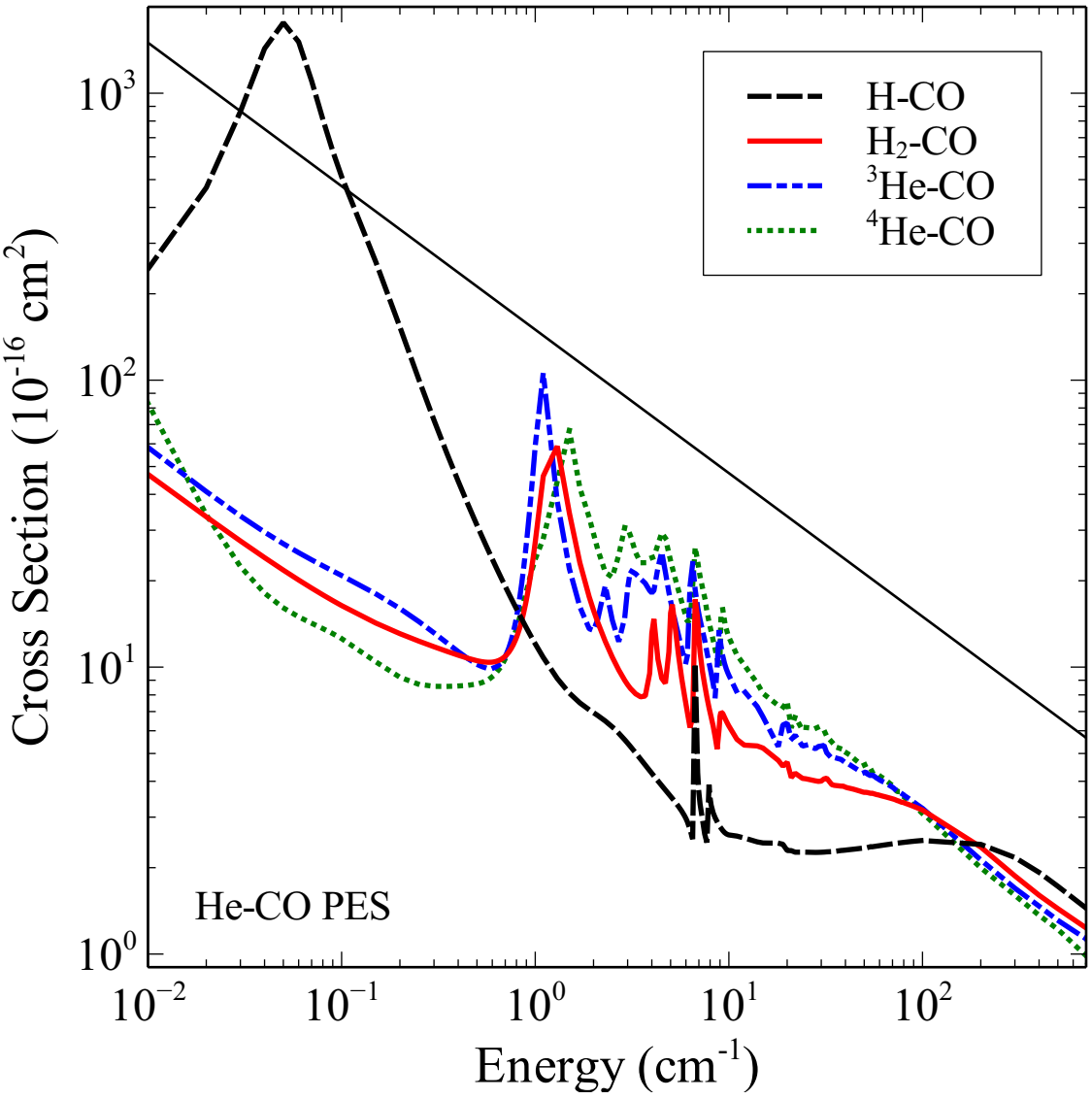

Figure 3.2: Cross sections of the colliders H, para-H_2, ^{3}He, and ^{4}He on the He-CO PES for the $j = 1 \rightarrow 0$ transition. The straight solid line indicates a $1/v$ cross section dependence.

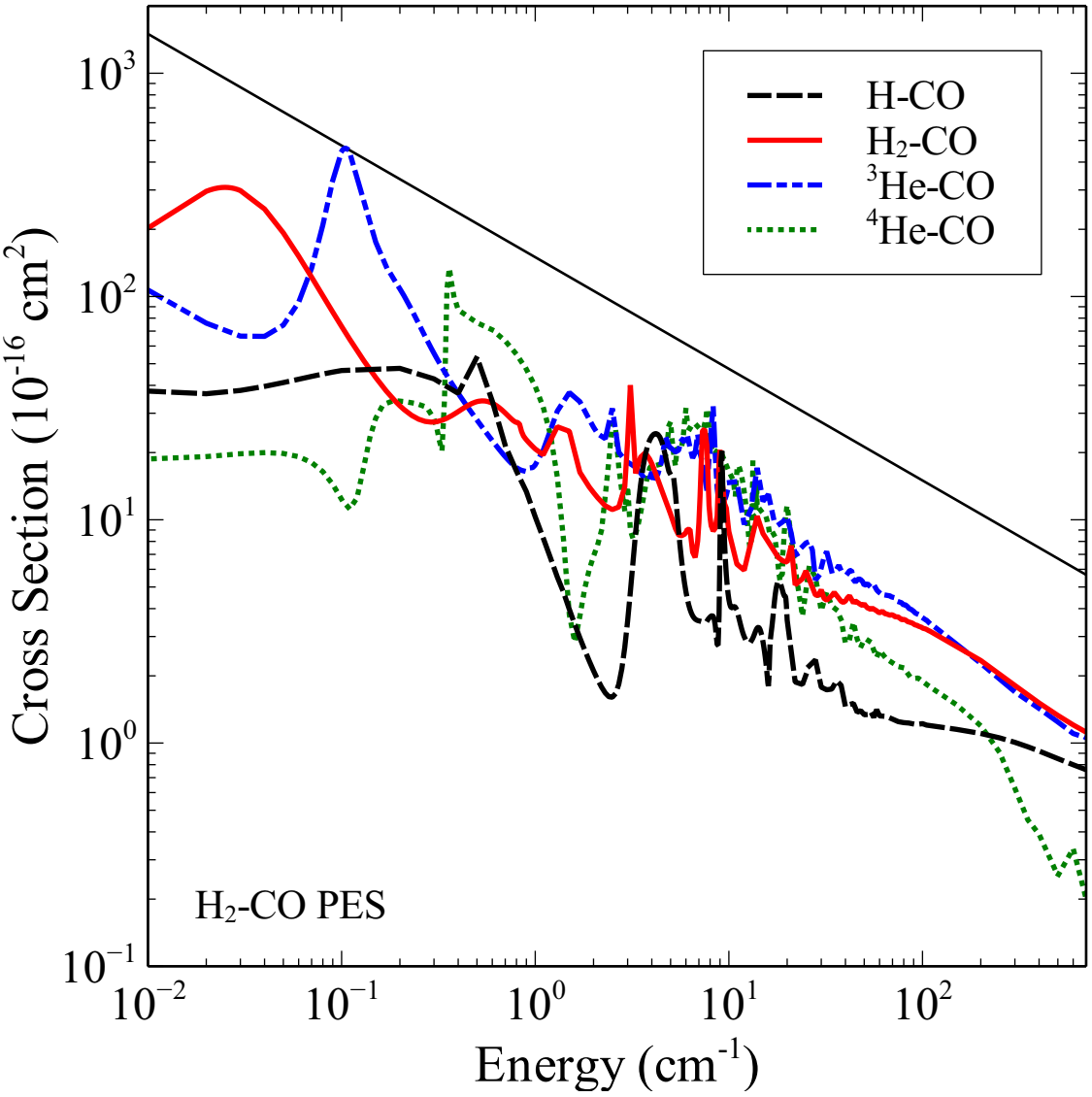

Figure 3.3: Same as Figure 3.2 for the H_2-CO PES.

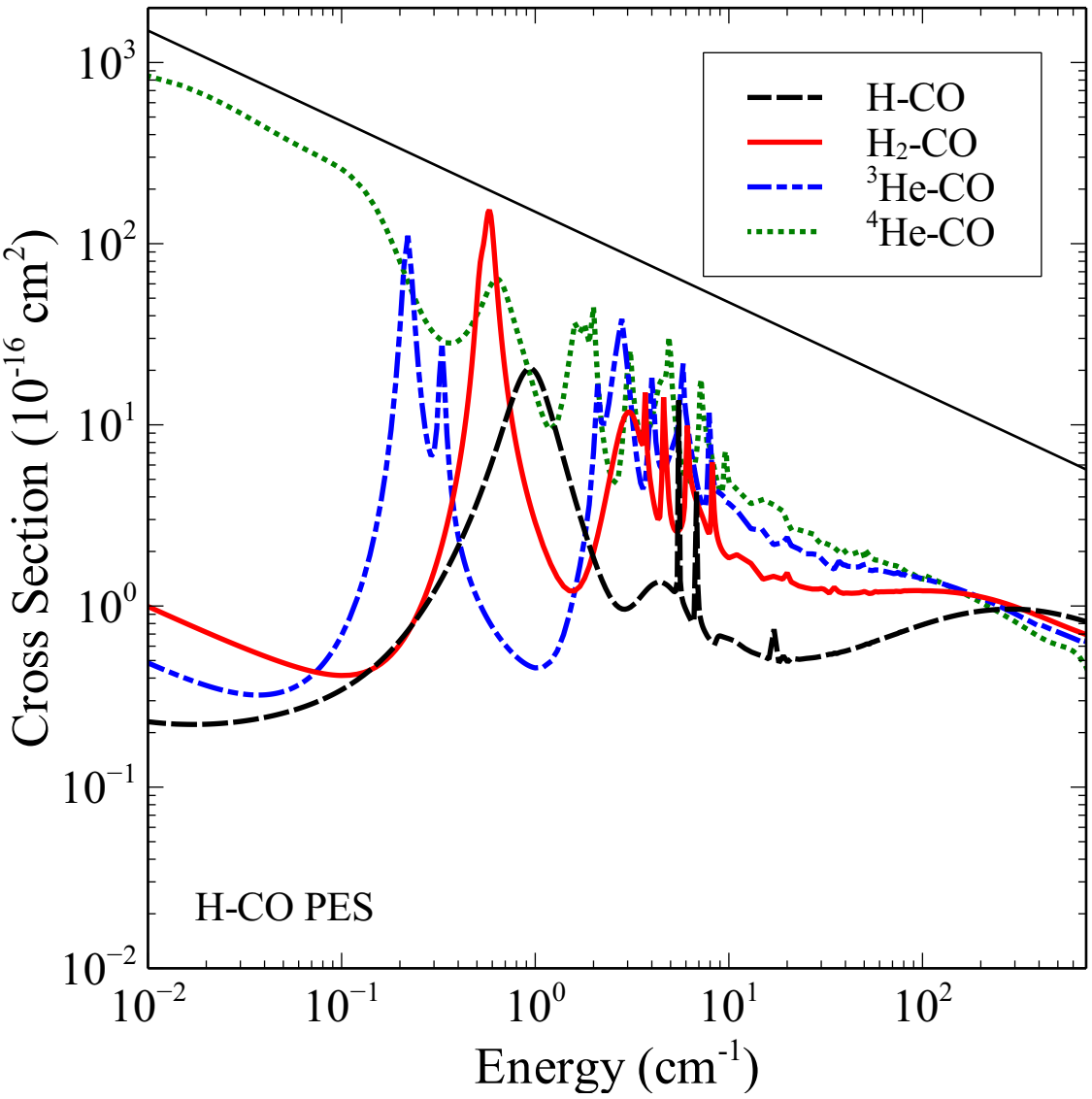

Figure 3.4: Same as Figure 3.2 for the H-CO PES.

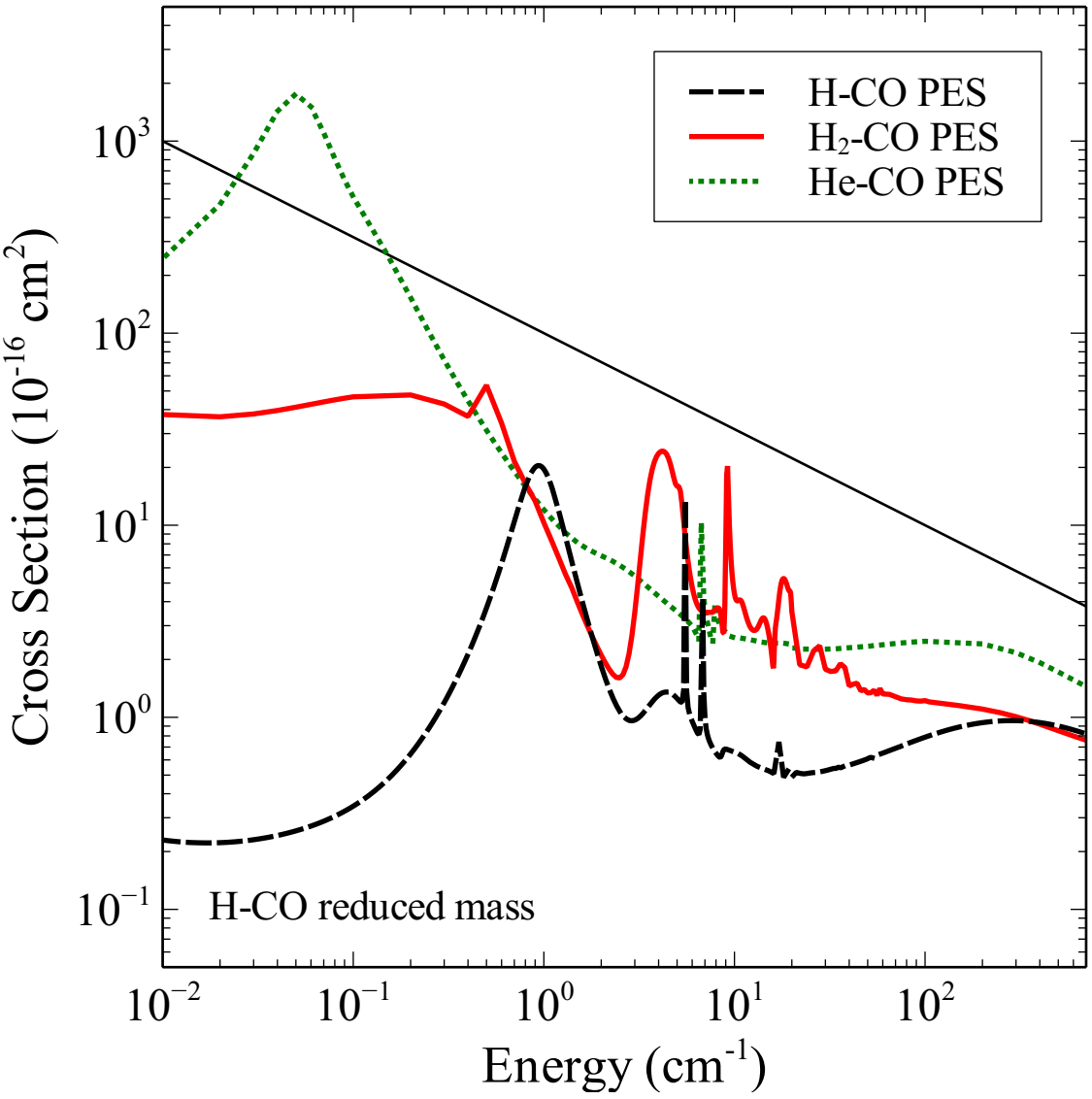

Figure 3.5: Cross sections for the $j = 1 \rightarrow 0$ transition using the H-CO reduced mass on the H-, H_2-, and He-CO PESs. The straight solid line indicates a $1/v$ cross section dependence.

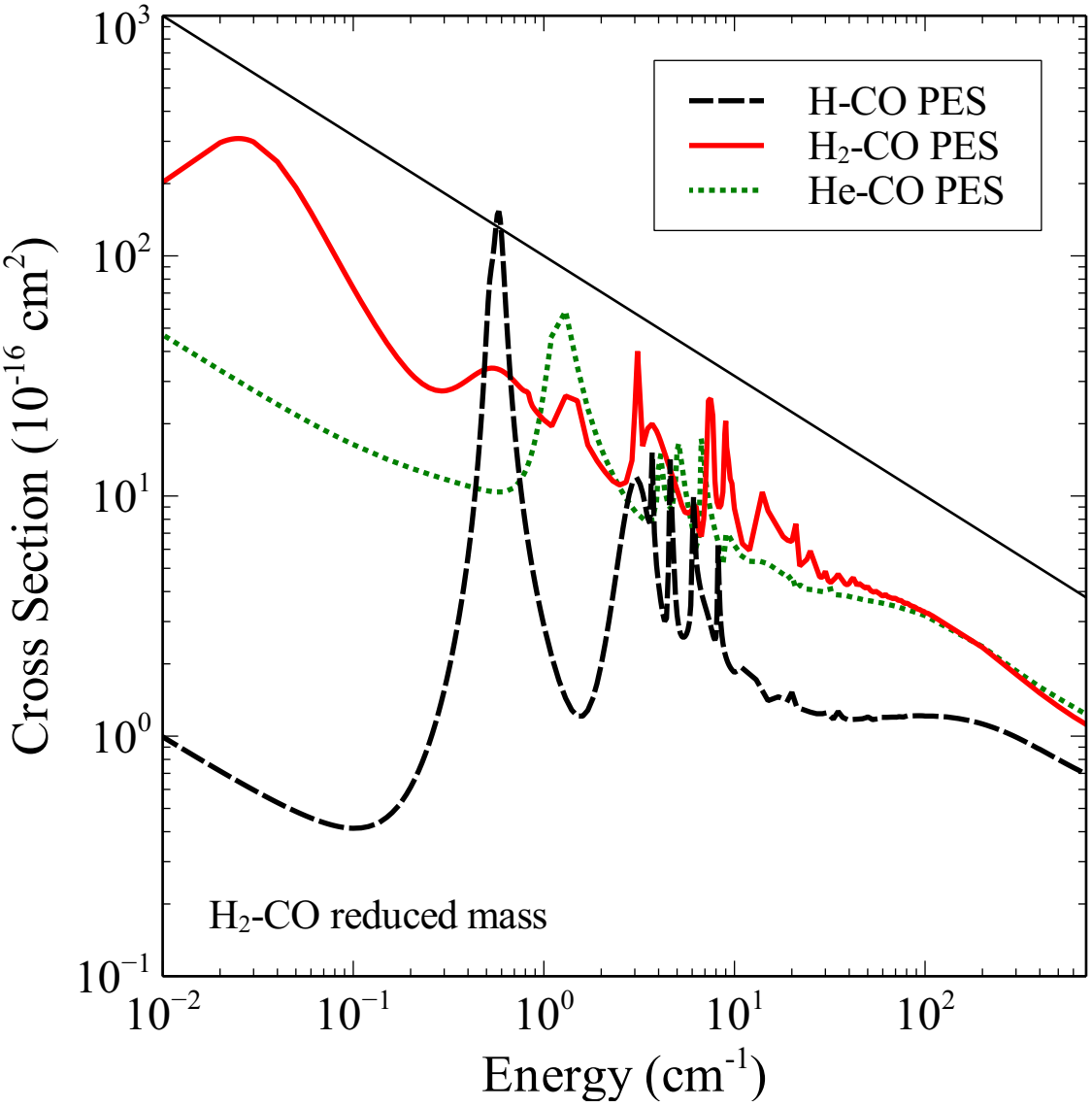

Figure 3.6: Same as Figure 3.5 for the H_2-CO reduced mass.

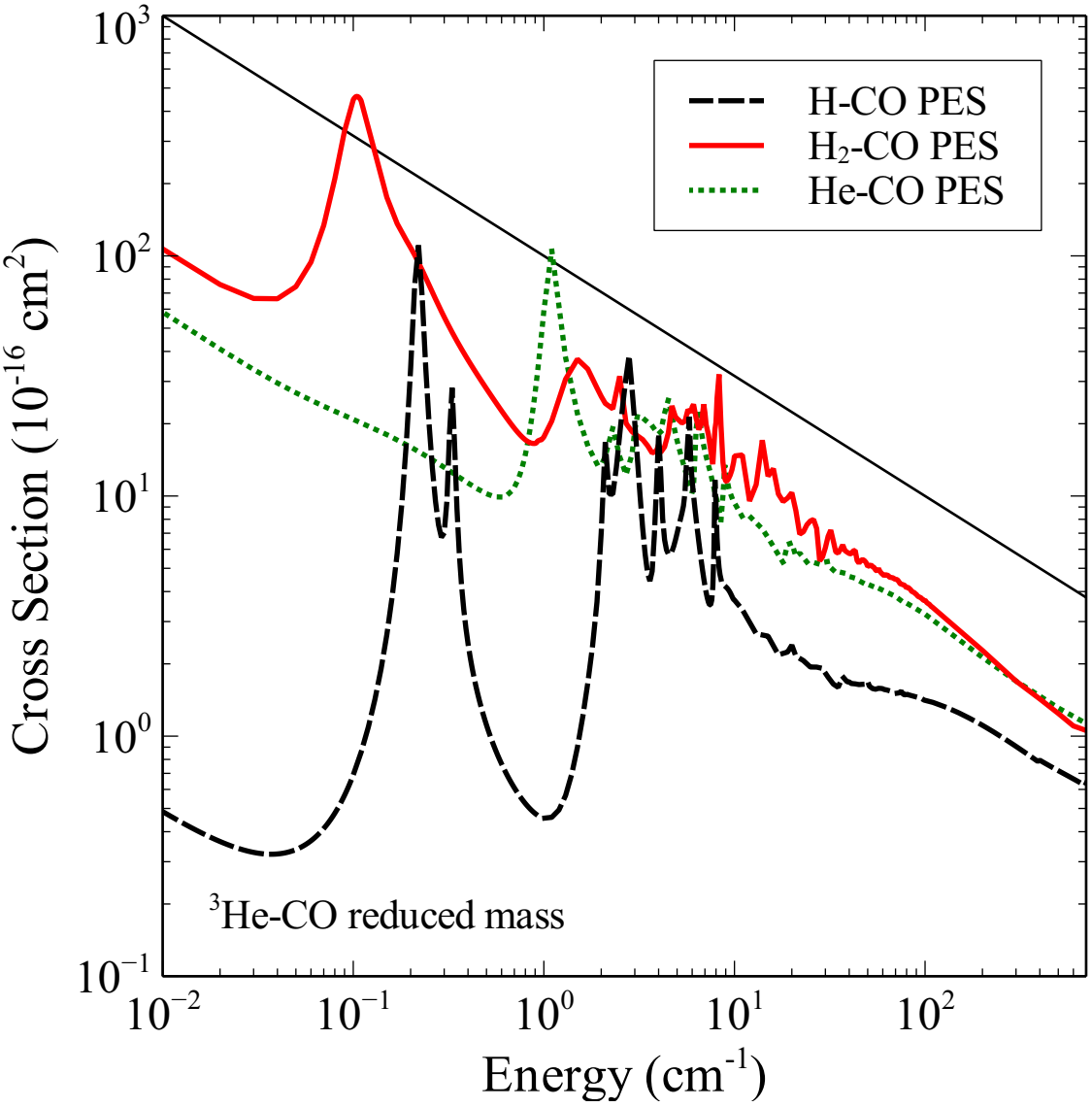

Figure 3.7: Same as Figure 3.5 for the ^{3}He-CO reduced mass.

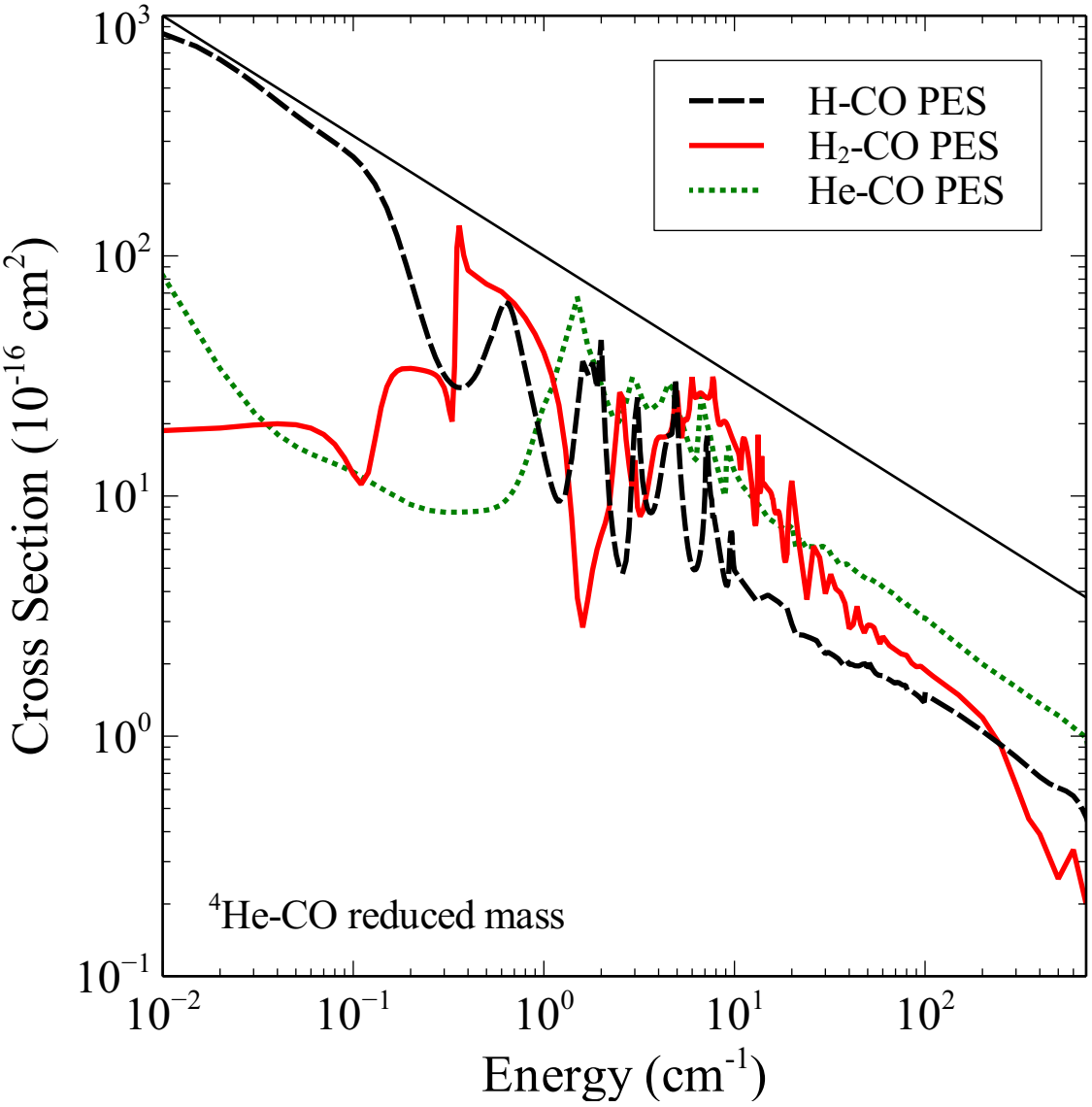

Figure 3.8: Same as Figure 3.5 for the ^{4}He-CO reduced mass.

Results for the other three masses were likewise found to be sensitive to the PES and are shown in Figs. 3.6–3.8. As expected, the cross section does indeed depend on both the PES and μ, and the assumptions implicit in Equation (3.1) are not valid.

As a yet further illustration, Equation (2.45) can be rewritten with the cross section given in terms of the relative velocity v of the collision system (Flower 2007);

$$k_{j\to j'}(T) = \left(\frac{2}{\pi}\right)^{\frac{1}{2}} \left(\frac{\mu}{k_B T}\right)^{\frac{3}{2}} \int_0^\infty \sigma_{j\to j'}(v) \exp\left(-\mu v^2/2k_B T\right) v^3 dv. \tag{3.2}$$

This leaves μ in both the exponential Boltzmann term in the integral and in the prefactor and shows that the original arguments justifying standard reduced-mass scaling should be reconsidered (compare to Equation 2.45). To gain additional insight and to explore an alternate scaling approach, assume the cross section to have the analytical form

$$\sigma_{j\to j'}(v) = Bv^a, \tag{3.3}$$

where B is an (undetermined) constant and a is some power. This leads to rate coefficients of the form (Stancil et al. 1998)

$$k(T) = A(a)B(T/\mu)^b, \tag{3.4}$$

where $b = (1/2)(a+1)$ and A is a function of a, both deduced from the Gaussian integral in Equation (3.2). This result is exact, given the assumption of Equation (3.3), and applicable to all collision systems. Therefore, if $\sigma(v)$ is assumed to be independent of the collider as originally supposed, Equation (3.1) is corrected by replacing the square-root with the exponent b yielding

$$k^{\mathrm{Z}}_{j\to j'}(T) = \left(\frac{\mu_{\mathrm{Y}}}{\mu_{\mathrm{Z}}}\right)^b k^{\mathrm{Y}}_{j\to j'}(T). \tag{3.5}$$

The scaling equation is now general for any two colliders Y and Z and any dependence of cross section on energy. Only for a constant cross section will b equal 1/2.

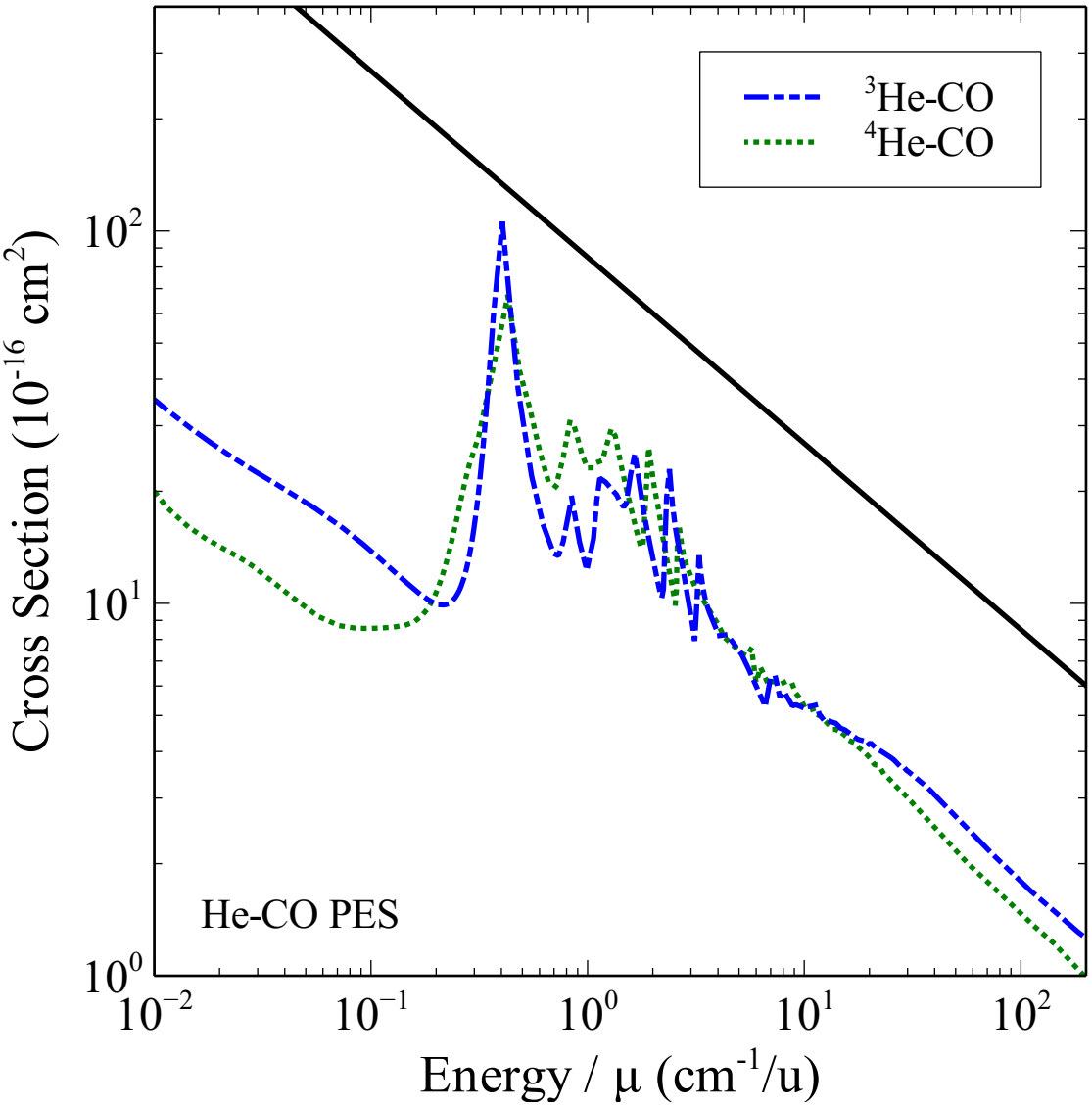

Figure 3.9: Cross sections for the $j = 1 \rightarrow 0$ transition of CO as a function of kinetic energy/μ for the colliders ^{3}He and ^{4}He on the He-CO PES. The straight solid line indicates a $1/v$ cross section dependence.

Figure 3.9 displays the cross section dependence for ^{3}He-CO and ^{4}He-CO, but plotted as a function of the kinetic energy divided by μ, which is proportional to v^2. Above $\sim$0.1 cm^{-1}/u, the cross section is relatively independent of μ, a concept well-known in ion-atom collisions (e.g., Stancil & Zygelman 1995). Figure 3.10 gives a related plot where He and para-H_2 colliders give qualitatively similar behavior, with the background cross sections of each falling-off with a $1/v$ dependence for $E \gtrsim 2$ cm^{-1}/u. Combining these observations with Equations (3.4) and (3.5), the resulting rate coefficients, neglecting the resonances, will be relatively independent of both T and μ (i.e., $a = -1$, $b = 0$). The H cross section is smaller due to a considerably different PES structure (see Chapter 2 and Shepler et al. 2007).

As possible intermediate methods between scaling and explicit calculations, we attempted four other approaches to obtain predictions for para-H_2 as depicted in Figure 3.11. First, considering the differing PESs, a possible scaling is obtained from the ratio of the reduced potentials $\mu_X \varepsilon_X$ (Joachain 1979), where ε_X is the van der Waals well-depth of the PES. However, the H_2 rate coefficients for the $1 \rightarrow 0$ transition are overestimated (see below). Second, explicit scattering calculations using μ_{H_2} on the He-CO PES gave rates in reasonable agreement with the explicitly calculated H_2-CO results. Third, multiplying these rates by the ratio of the well depths alone (a factor of $\sim$3.9, not shown), and by the ratio of reduced potentials again overestimated the H_2 rate coefficients. Finally, cross sections using μ_{H_2} on the He-CO PES scaled to match ε_{H_2} were computed, but the resulting rate coefficients overestimated the explicit H_2-CO rates. Of these, the second approach, which used the simpler 2D He-CO PES with μ_{H_2} appears to give the best results, but still requires new scattering calculations.

Considering the above findings, we arrive at the two most promising scaling options. In the first case, Equation (3.5) can be applied above $\sim 10 - 50$ K when $k_{j \rightarrow j'}(T)$ is known for He. The lower limit can be estimated with knowledge of ε_X which is roughly equal to the upper kinetic energy limit of the quasibound resonances (see Figs. 3.2 - 3.10). For

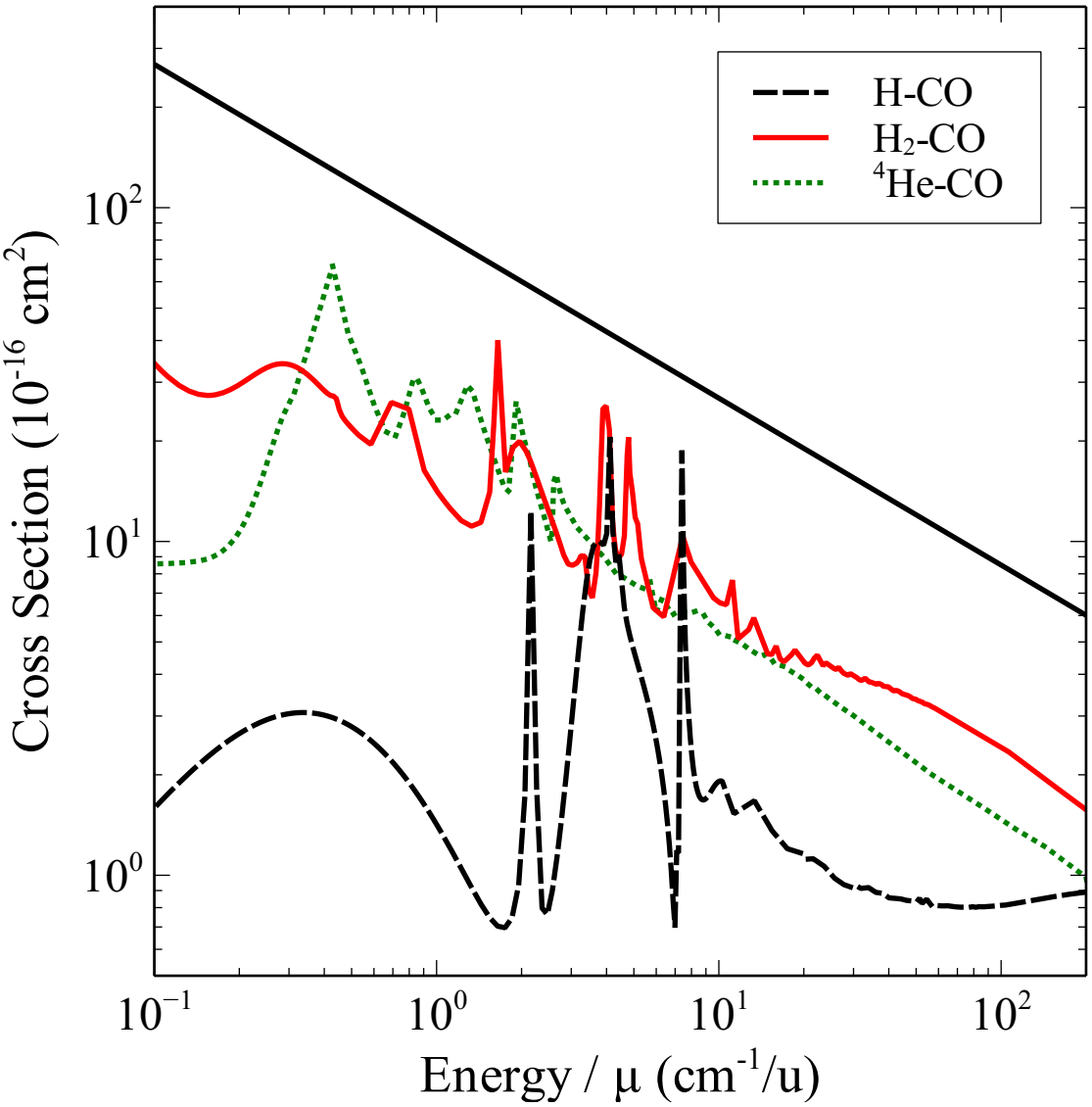

Figure 3.10: Cross sections for the $j = 1 \rightarrow 0$ transition of CO as a function of kinetic energy/μ for calculated cross sections on their respective PESs. The straight solid line indicates a $1/v$ cross section dependence.

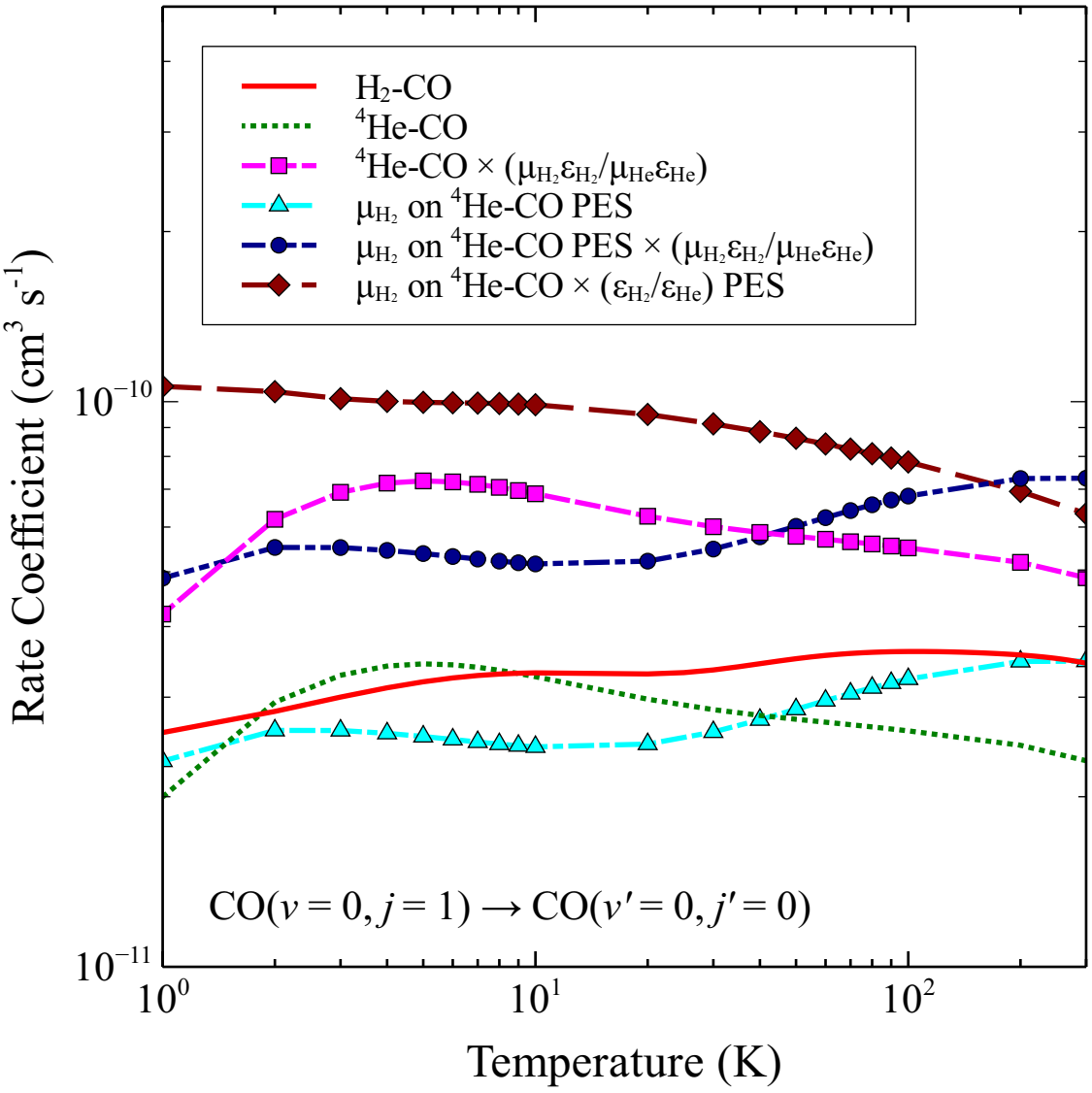

Figure 3.11: Rate coefficients for the deexcitation of CO(j=1) with the colliders He and para-H_2 and estimated values for H_2 via possible scaling relations. See text for discussion. $\varepsilon_{H_2} = 93.1$ cm^{-1} (Jankowski & Szalewicz 2005) and $\varepsilon_{He} = 23.7$ cm^{-1} (Heijmen et al. 1997).

example, if $b = 0$ ($a = -1$), the rate coefficients are independent of T and μ_X, as opposed to Equation (3.1). Of course B is assumed to be the same for He and H_2 colliders.

The second option is appropriate for $T \lesssim 10-100$ K where rate coefficients are highly sensitive to quasibound resonances. These resonances may partially be accounted for by scaling via the ratio of the reduced potentials $\mu_X \varepsilon_X$, as discussed above, with a phenomenological exponent C according to

$$k^{\mathrm{Z}}_{j\to j'}(T) = \left(\frac{\mu_{\mathrm{Z}}\varepsilon_{\mathrm{Z}}}{\mu_{\mathrm{Y}}\varepsilon_{\mathrm{Y}}}\right)^{C} k^{\mathrm{Y}}_{j\to j'}(T). \tag{3.6}$$

Numerical values for the van der Waals well-depths of the interaction PESs are generally available from experimental and theoretical work in the chemical physics community (see Radzig & Smirnov 1980). This scaling option was explicitly tested for fifteen Δj transitions using He-CO (Cecchi-Pestellini et al. 2002) and H_2-CO (Yang et al. 2010) theoretical data. The exponent C was optimized to minimize the scaling residuals from $5 \sim 500$ K. Figure 3.12a,b shows that both the $2\to0$ and $5\to4$ rate coefficients scaled via the reduced potential method give the best estimates. In fact, even Δj transitions scaled by the reduced potential ratio with exponent $C \sim 0.7-1.3$ give good predictions for H_2-CO rate coefficients.

Although standard reduced-mass scaling reproduces the H_2-CO data for odd Δj transitions more accurately than even Δj transitions, the agreement is likely fortuitous. Reduced-potential scaling, on the other hand, with $C \sim 0.0 - 0.4$ for odd Δj transitions, shows improvement of the predictions *and* is based on the physical properties of the interacting system. We note that near-homonuclear molecules, such as CO, follow propensity rules whereby odd Δj transitions are suppressed compared to even Δj transitions, and it seems the dichotomy of the phenomenological exponent C expresses this propensity.

To determine the accuracy of the new reduced-potential scaling approach, we calculated the normalized root-mean-square deviation (NRMSD), σ_{norm}, of the H_2 rate coefficient pre-

dictions for both standard reduced-mass scaling and reduced-potential scaling, given by:

$$\sigma_{norm} = \frac{\sqrt{\frac{\sum_{i=1}^{N}(k_{scale}(T_i)-k_{calc}(T_i))^2}{N}}}{k_{max}-k_{min}}, \tag{3.7}$$

where N is the number of temperature data points and k_{max} and k_{min} are the values of the maximum and minimum rate coefficients, respectively. The resulting percentage indicates the residual variance between the calculated H_2 rate coefficients, k_{calc}, and those scaled from He, k_{scale}. Table 3.1 lists these values for fifteen transitions of CO. There is a remarkable improvement in reduced-potential scaling predictions for even Δj transitions. Odd Δj transitions also show improved predictions of reduced-potential scaling over standard reduced-mass scaling, albeit less so. These odd Δj transitions exhibit the broadest range in rate coefficients and can vary more than an order of magnitude across the temperature range $2-500$ K, whereas rate coefficients for the even Δj transitions are primarily flat across this range. Hence the odd Δj transitions contain a larger residual variance.

Figure 3.13 - 3.14 gives an example of a similar study of reduced-potential and standard reduced-mass scaling for H_2O to due He and para-H_2 collisions. From a survey of 32 transitions, the dominant transitions which obey the propensity rules[2] $|\Delta j| = |\Delta k_a| = |\Delta k_c| = 1$ are reasonably reproduced by the reduced-potential approach with $C \sim 0.6-0.8$, while the subdominant transitions $|\Delta j| = 1$, $\Delta k_a = 0$, $\Delta k_c = \pm 2$ or $\Delta k_a = \pm 2$, $\Delta k_c = 0$ and $|\Delta j| = 2$, $\Delta k_a = 0$, $\Delta k_c = \pm 2$ or $\Delta k_a = \pm 2$, $\Delta k_c = 0$ extend this range to $C \sim 0.5-1.2$. Cases which are reproduced best with $C \lesssim 0.5$ or $\gtrsim 1.2$ typically correspond to weak transitions with rate coefficients 2-3 orders of magnitude smaller than the dominant transitions so that errors in their prediction are of less significance.

The reliability of the reduced-potential scaling method was again addressed by computing the NRMSD and comparing it to the NRMSD of standard reduced-mass scaling.

[2] k_a and k_c are quantum numbers assigned to asymmetric tops such as water whose three principle moments of inertia have different values.

Figure 3.15 compares the NRMSD for both methods for each transition of H_2O. Predictions from reduced-potential scaling exhibit less residual variance in all 32 transitions, with a mean of 35% or less, and clearly demonstate the superiority of the new reduced-potential scaling method.

Finally, Figure 3.16 shows the two scaling methods for H-CO collisions, where the reduced-potential with $C = 0.9$ rather than standard reduced-mass scaling more accurately predicts the calculated rate coefficients. While additional studies of reduced potential scaling on a variety of other molecules are needed and in progress, the cases studied here suggest that the approach can reasonably predict rate coefficients for dominant transitions with $C \sim 0.8$, while $C < 0.4$ can account for weak transitions with the partitioning predicted from known propensity rules.

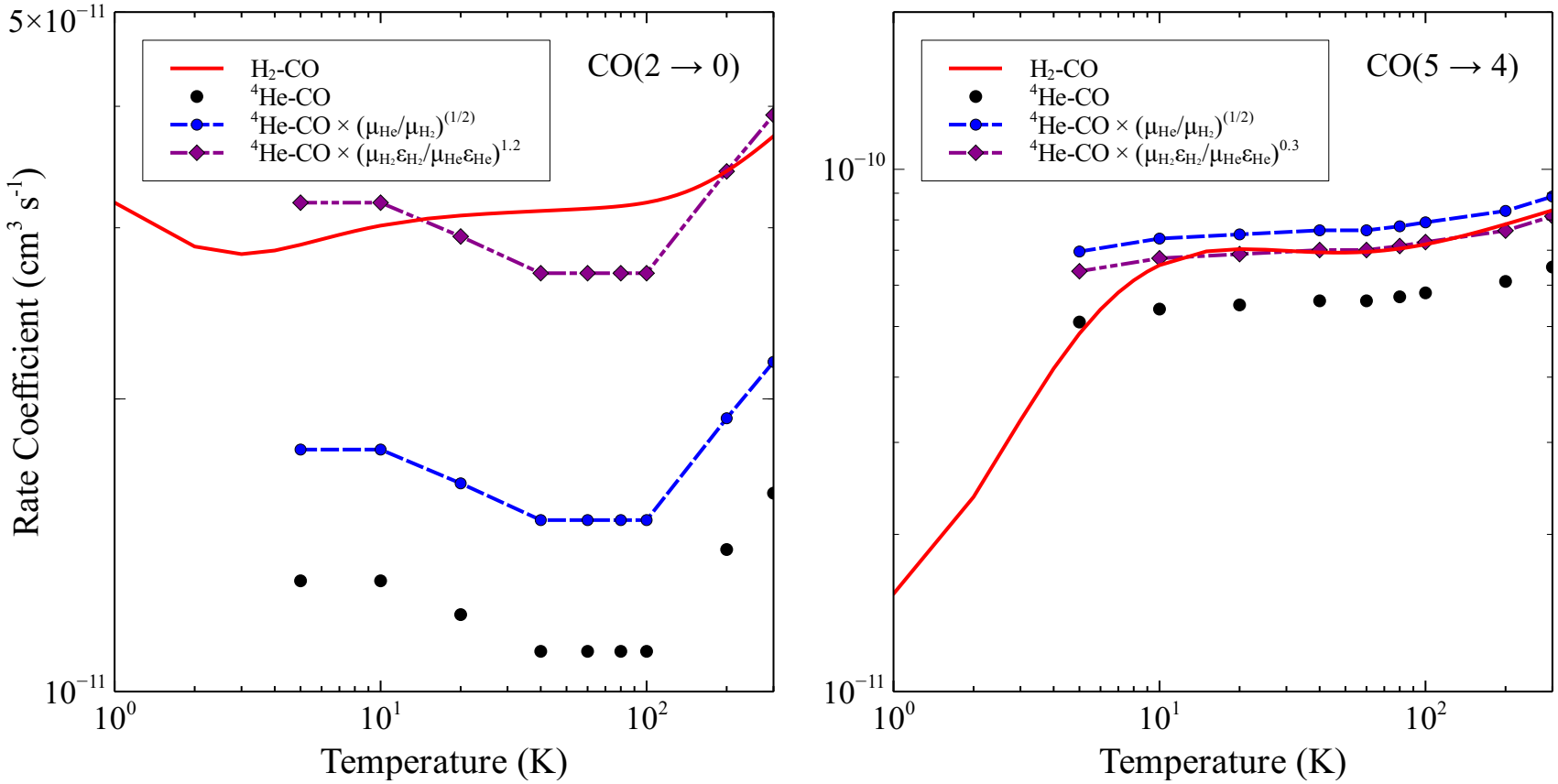

Figure 3.12: Rate coefficients for the (a) $j = 2 \rightarrow 0$ and (b) $j = 5 \rightarrow 4$ transitions of CO with H_2 (Yang et al. 2010) and He (Cecchi-Pestellini et al. 2002) compared to the predictions of standard reduced-mass scaling and reduced-potential scaling with $C = 1.2$ and 0.3, respectively.

Table 3.1: The optimized values of C and their respective normalized root-mean-square deviations (NRMSD) for collisional deexcitation transitions of CO with H_2 and He scaled via the standard reduced-mass (rm) and new reduced-potential (rp) methods.

Δj	$j \rightarrow j'$	C	NRMSD_{rm}	NRMSD_{rp}
Even	2-0	1.2	138.60	17.95
$\cdots$	3-1	1.2	125.31	18.04
$\cdots$	4-2	1.2	133.00	17.64
$\cdots$	5-3	1.3	141.07	25.73
$\cdots$	4-0	0.9	50.16	9.06
$\cdots$	5-1	0.7	28.57	4.07
Odd	4-3	0.4	27.41	26.63
$\cdots$	3-2	0.4	34.38	34.99
$\cdots$	2-1	0.4	40.07	40.89
$\cdots$	5-4	0.3	31.62	18.81
$\cdots$	1-0	0.3	52.43	41.02
$\cdots$	5-0	0.1	20.06	13.79
$\cdots$	4-1	0.1	35.88	22.23
$\cdots$	3-0	-0.2	38.91	29.48
$\cdots$	5-2	-0.2	38.59	34.45

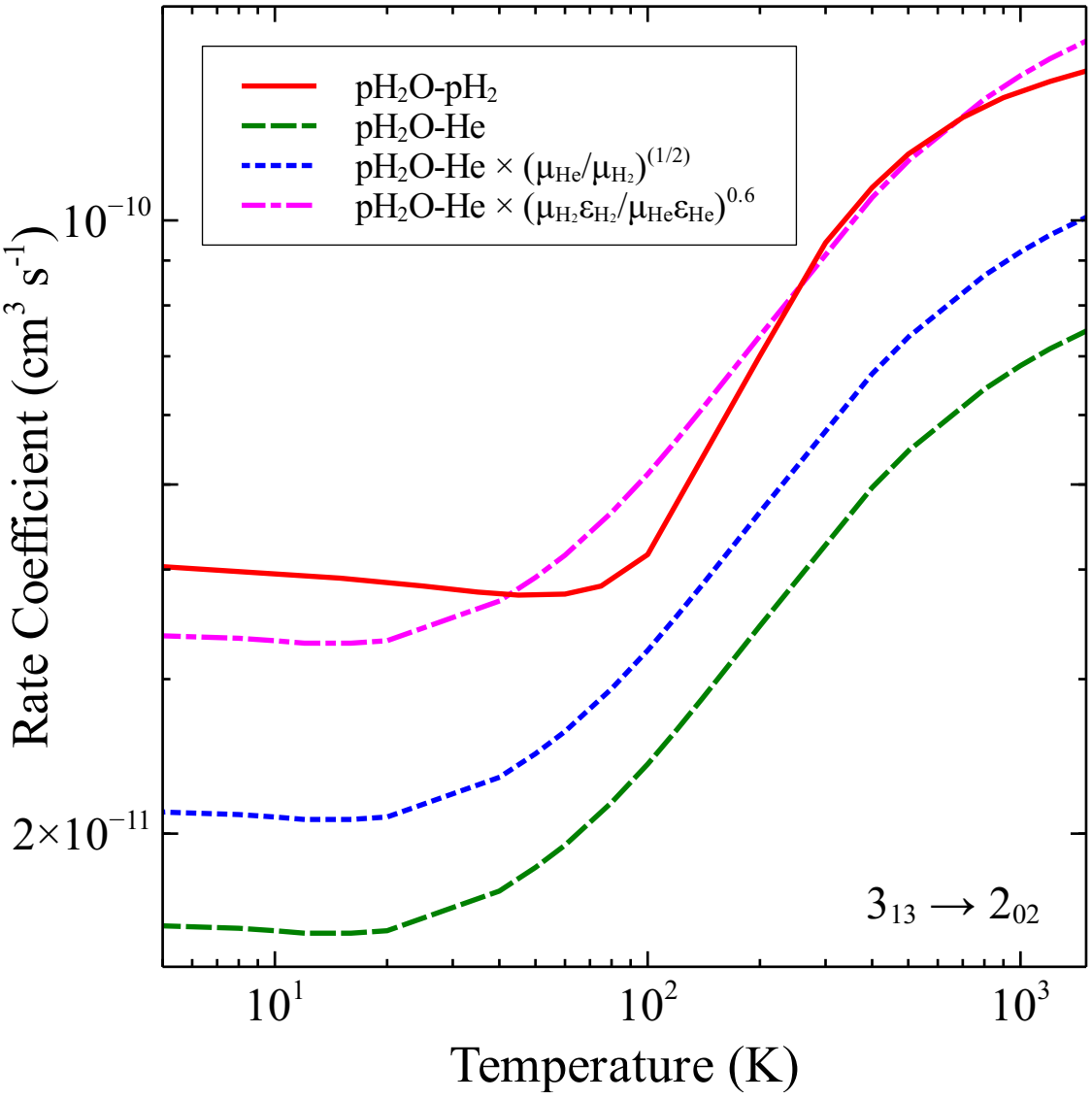

Figure 3.13: Rate coefficients for the deexcitation of $H_2O(j_{k_a k_c})$ $3_{31} \rightarrow 2_{20}$ with para-H_2 (Dubernet et al. 2009) and He (Yang et al. 2013a) compared to standard reduced-mass scaling and reduced-potential scaling with $C = 0.6$. The water well-depths are: $\varepsilon_{\rm He} = 34.4$ cm^{-1} (Patkowski et al. 2002) and $\varepsilon_{\rm H_2} = 221.9$ cm^{-1} (Faure et al. 2005).

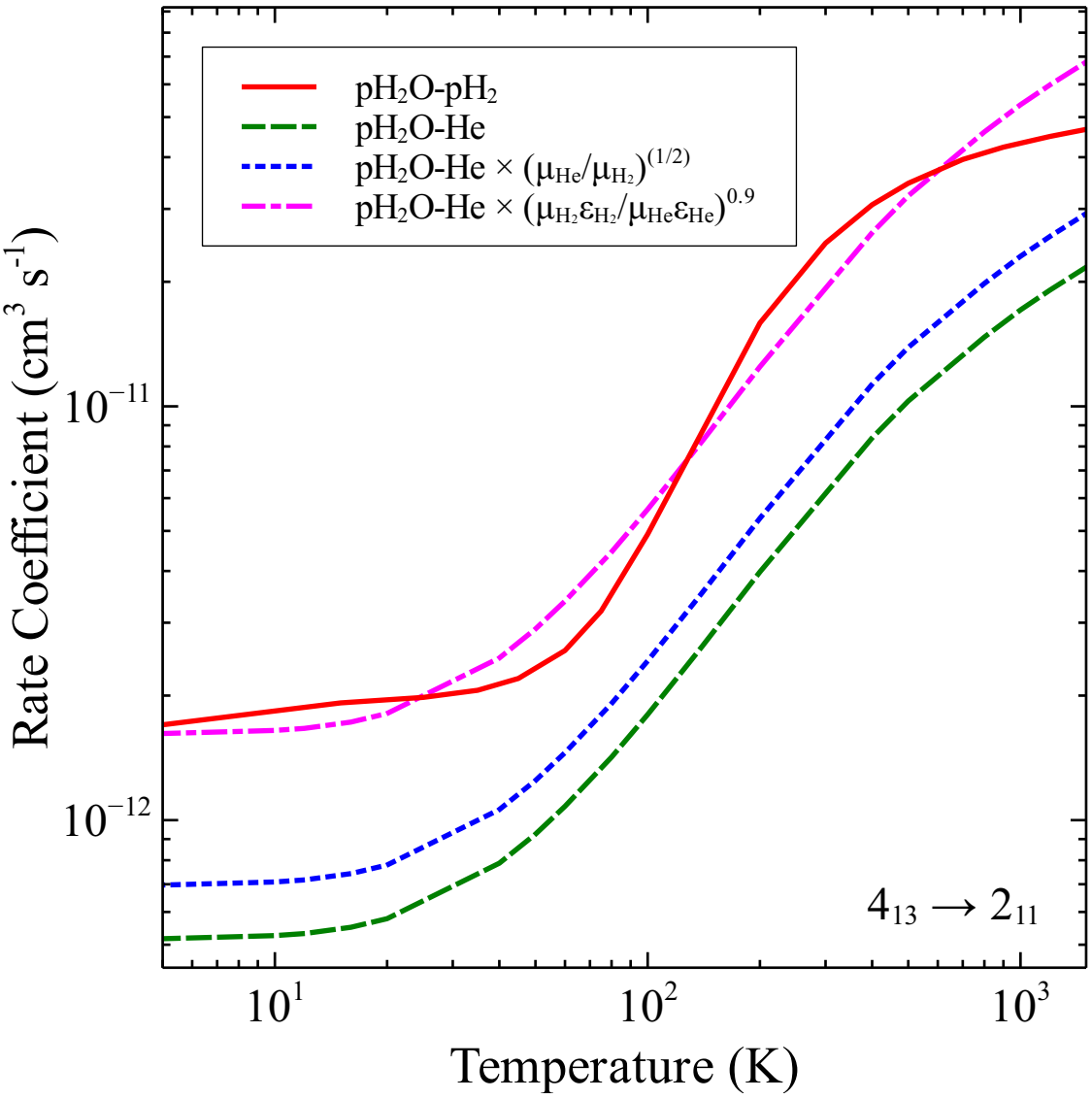

Figure 3.14: Same as Figure 3.13 for the $H_2O(j_{k_a k_c})$ $4_{13} \rightarrow 2_{11}$ with $C = 0.9$.

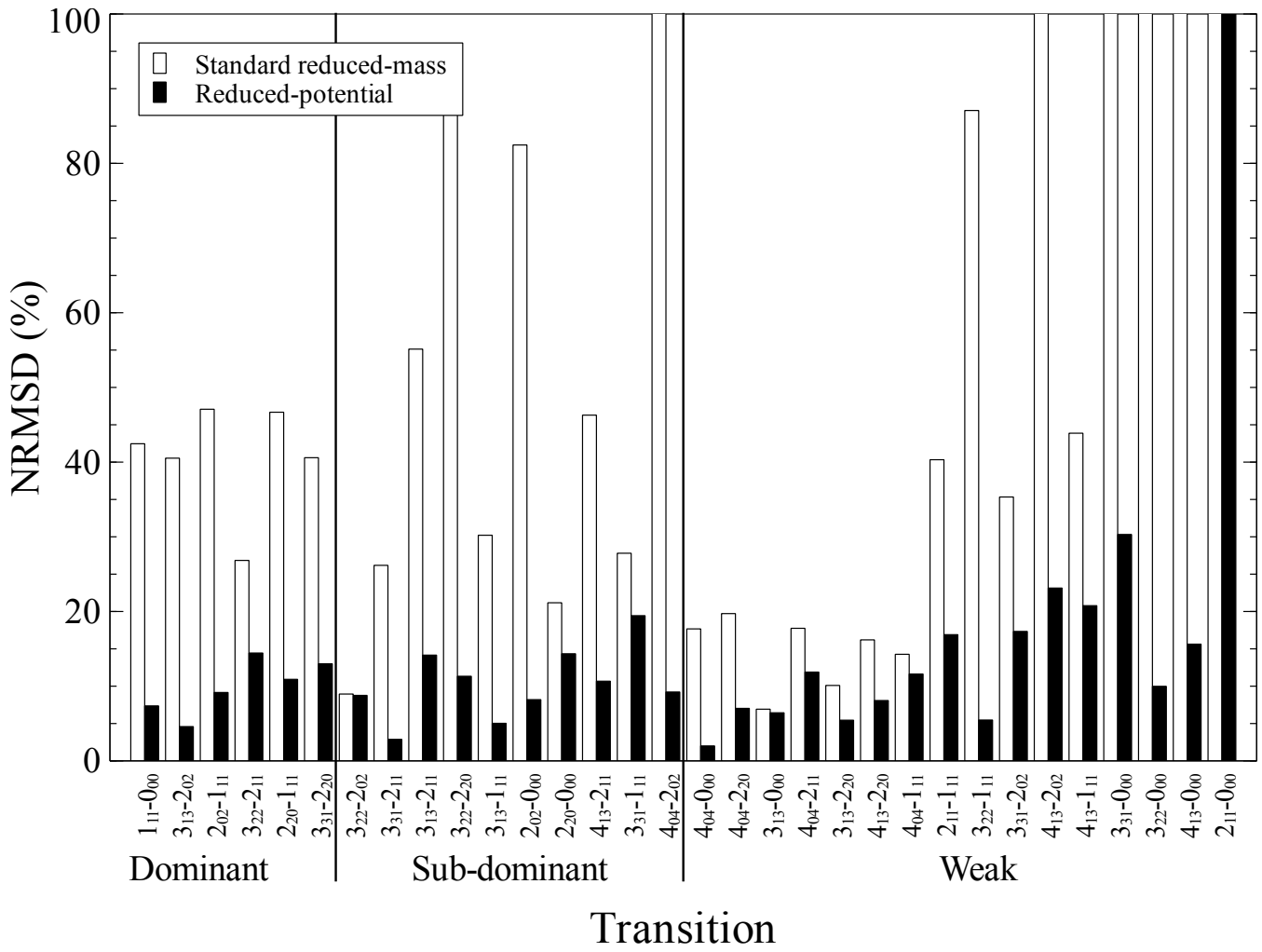

Figure 3.15: The normalized root-mean-square deviation (NRMSD) in standard reduced-mass scaling and reduced-potential scaling for 32 transitions of H_2O, truncated at 100%. The dominant, sub-dominant, and weak transitions are further organized from left to right in increasing values of the exponent C.

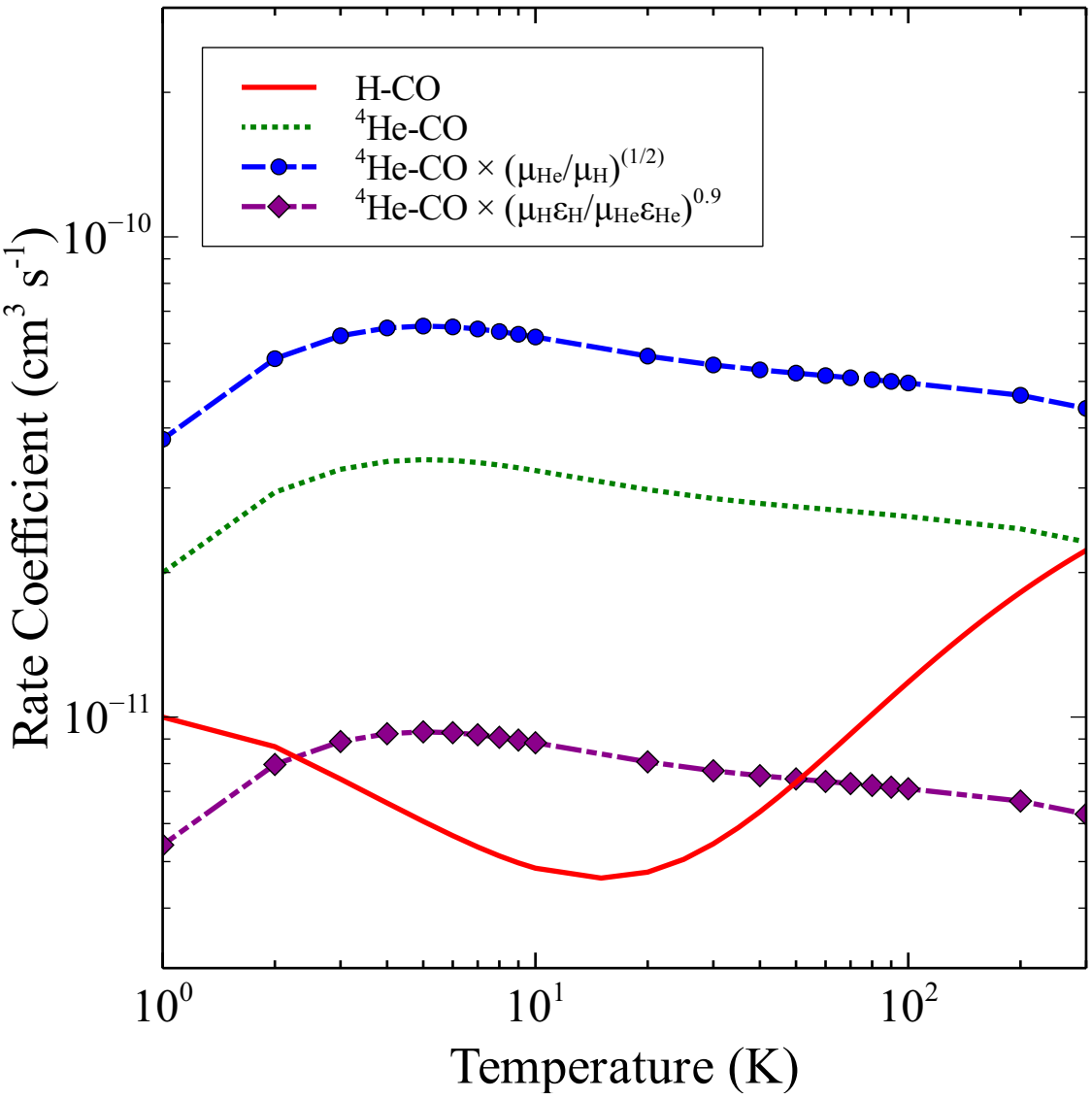

Figure 3.16: Rate coefficients for the deexcitation of CO(j=1) with H (Yang et al. 2013b) and He compared to standard reduced-mass scaling and reduced-potential scaling with $C = 0.9$.

3.2 Application of Reduced-Potential Scaling to HF

The first detection of HF absorption in the interstellar medium was toward Sagittarius B2, a giant molecular cloud complex residing near the center of our galaxy (Neufeld et al. 1997). Since then, HF has been detected in absorption in diffuse molecular clouds (Sonnentrucker et al. 2010), in high-mass star-forming regions (Emprechtinger et al. 2012), and in emission in HII regions (van der Tak 2012). The nature of these environments may cause the rotational levels of HF to exhibit non-thermal behavior and so models may require consideration of H, H_2, He, and electron collisions to accurately discern the physical parameters of the region. However, collisional rate coefficient data are limited to rotational quenching in the HF ground vibrational state from upper states $j \leq 20$ for collisions with He (Yang et al. 2015) and $j \leq 5$ for collisions with H_2 (Guillon & Stoecklin 2012). Rate coefficients with H have not yet been calculated. The He collisional data presented in Yang et al. (2015) range in temperatures from $2 - 3000$ K, while the rate coefficients for para-H_2 span temperatures from $10 - 150$ K. The rate coefficients in this temperature range are sensitive to the presence of quasibound resonances, and the reduced-potential approach detailed above may partially account for them by considering the interaction well-depths.

Both the standard reduced-mass and reduced-potential scaling methods detailed above in section 3.1 are compared in Figure 3.17 for the HF rotational deexcitation transition $j = 1 - 0$. Standard reduced-mass scaling results in an estimate for para-H_2 collisions that is a factor of 10 too small, but the reduced-potential approach with a phenomenological exponent of $C = 1.7$ agrees well with the explicitly calculated rate coefficients of Guillon & Stoecklin (2012).

Compared to the standard reduced-mass scaling technique, and just like CO and H_2O, the reduced-potential scaling approach offers an improvement for predicting HF rate coefficients. To test the accuracy of the reduced-potential scaling approach, the normalized root-mean-square deviation was once again used to quantify the residual variance between the calculated and scaled rate coefficients. The resulting NRMSD percentages for the H_2 rate coefficient

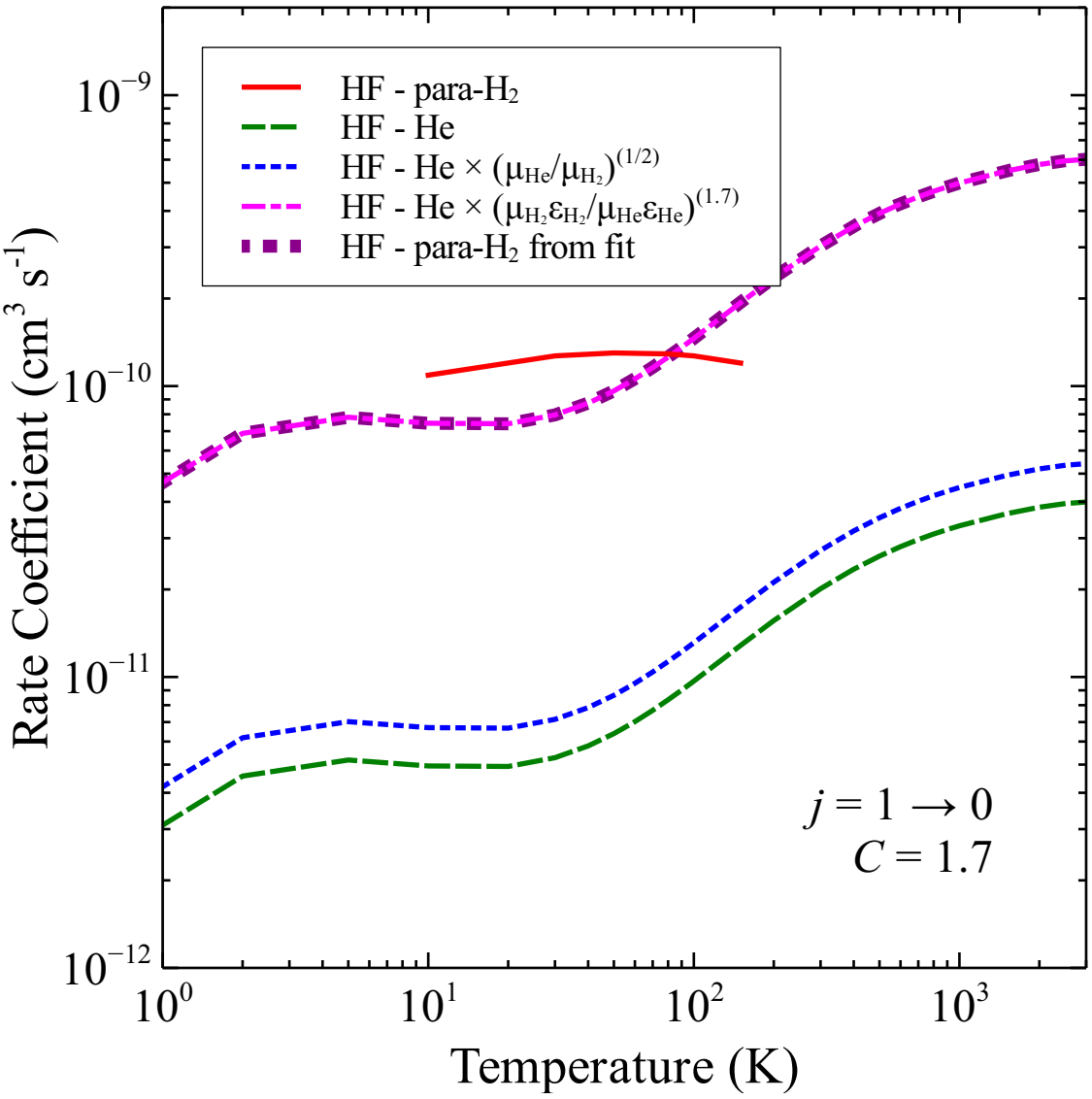

Figure 3.17: Rate coefficients for the deexcitation of HF(j=1) due to para-H_2 (Guillon & Stoecklin 2012) and He (Yang et al. 2015) and a comparison of standard reduced-mass scaling and reduced-potential scaling for para-H_2 rate coefficients with $C = 1.7$.

Table 3.2: The optimized values of C and their respective normalized root-mean-square deviations (NRMSD) for collisional deexcitation transitions of HF with H_2 and He scaled via the standard reduced-mass (rm) and reduced-potential (rp) methods.

$j \rightarrow j'$	C	NRMSD_{rm}	NRMSD_{rp}
1-0	1.7	1058.85	34.90
2-0	1.3	299.75	22.66
2-1	0.6	161.28	15.42
3-0	-0.2	53.29	7.55
3-1	-0.1	30.66	8.77
3-2	-0.2	62.78	3.77
4-0	-1.6	69.89	8.14
4-1	-0.3	42.20	16.48
4-2	-1.3	73.59	13.37
4-3	-0.8	90.81	11.69
5-0	-1.2	54.55	18.68
5-1	-2.0	61.64	13.50
5-2	-0.5	44.98	16.22
5-3	-1.3	66.96	6.48
5-4	-1.2	86.17	7.98

predictions for both standard reduced-mass scaling and reduced-potential scaling are given in Table 3.2 and Figure 3.18 for the first fifteen transitions of HF at 50 K.

When comparing the NRMSD for both methods for each transition of HF, the reduced-potential scaling predictions exhibit less residual variance in all fifteen transitions. In several cases, the NRMSD for standard reduced-mass scaling exceeds 100%. The reduced-potential approach, on the other hand, never gives an NRMSD greater than 35% and has a mean of 14% when reproducing the explicit HF-H_2 calculations of Guillon & Stoecklin (2012).

The optimal values for C are plotted as a function of $|\Delta j|$ in Figure 3.19 for the first fifteen transitions of HF. A linear least-squares analysis was performed for each j' and the resulting linear functions are also plotted in Figure 3.19. Except for $j' = 2$, the lines converge around $|\Delta j| = 6$ and $C = -3$.

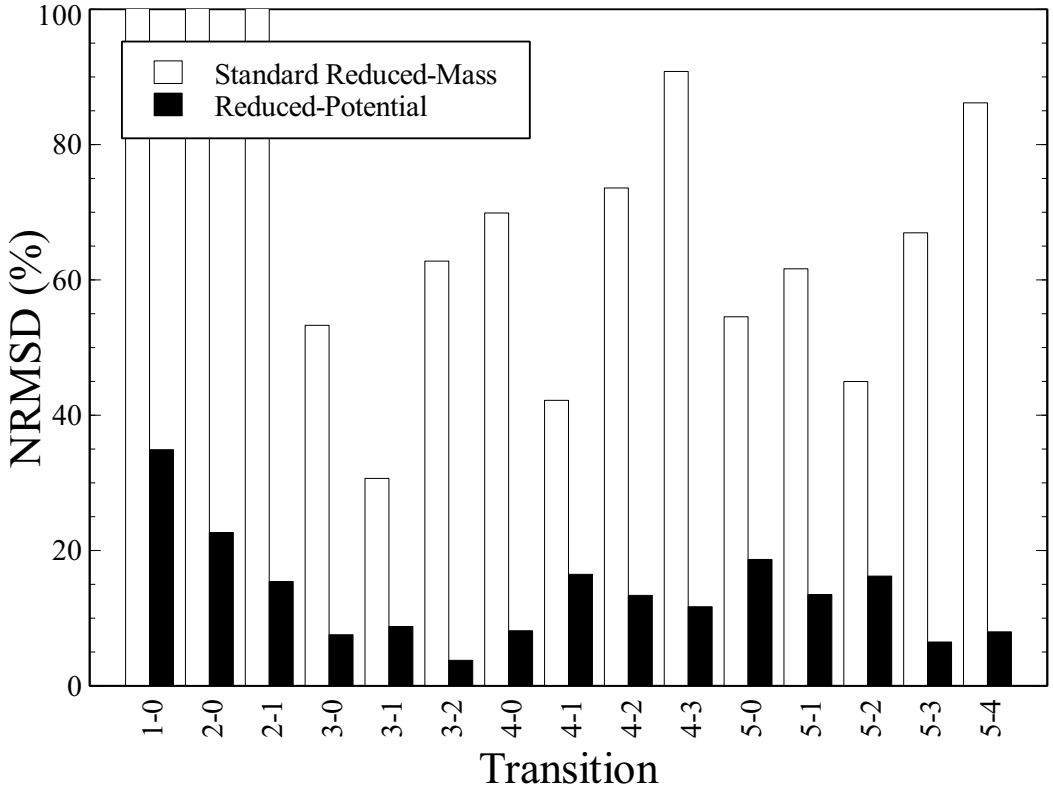

Figure 3.18: The normalized root-mean-square deviation (NRMSD) in standard reduced-mass scaling and reduced-potential scaling for 15 transitions of HF, truncated at 100%.

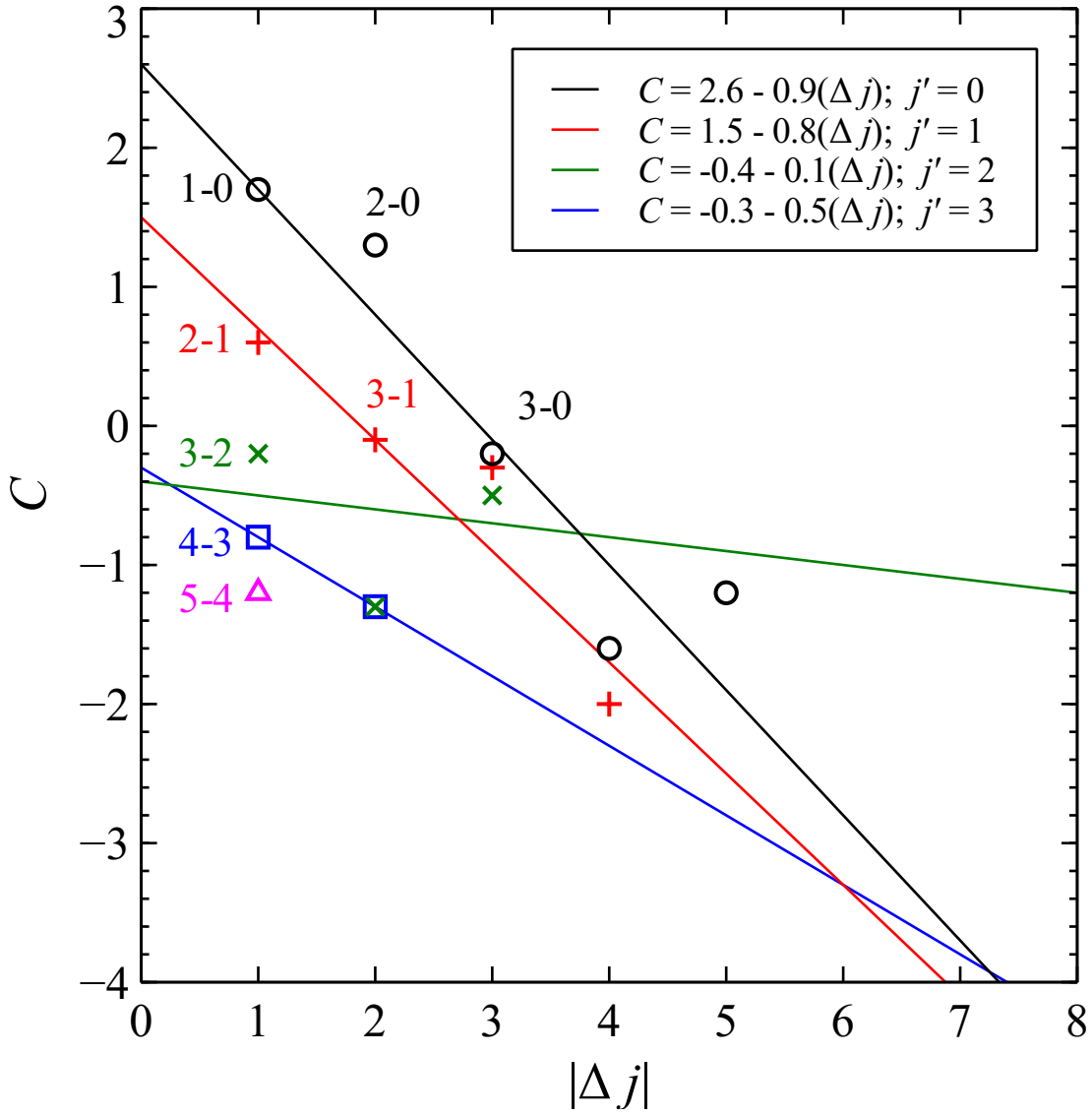

Figure 3.19: The phenomonological constant C as a function of $|\Delta j|$. A linear least-squares analysis was performed for each j' and the resulting linear functions are plotted. Note the convergence of these functions (except for $j' = 2$) around $|\Delta j| = 6$ and $C = -3$.

The value of C for each transition can be predicted by creating a set of linear functions that approximates the trends seen in Figure 3.19. This is accomplished by ensuring the optimal values for C, valid for all temperatures, exactly reproduce the reduced-potential scaling result for the dominant $\Delta j = -1$ transitions and forcing the functions to converge at $|\Delta j| = 6$ and $C = -3$. This set of functions is shown in Figure 3.20. For $|\Delta j| = 1$, the change in C (which decreases linearly with j') and slopes of the resulting linear functions are listed in Table 3.3. By obtaining the slope and intercept for each lower state, a value of C can be determined for all transitions up to $|\Delta j| = 6$. For the weak transitions where $|\Delta j| \geq 7$, the exponent $C = -3$ is adopted — these rate coefficients are several orders of magnitude less than the dominant transitions so larger error in the predicted values is acceptable. Rate coefficients for the transitions of H_2 with $j \leq 5$ are reproduced reasonably well by the reduced-potential approach with C decreasing with increasing $|\Delta j|$ and increasing j'. The predictions are shown in Figures 3.21 – 3.34 for HF transitions from $j \leq 5$. The standard reduced-mass scaling approach predicts rate coefficients more than an order of magnitude greater that the calculated values from Guillon & Stoecklin (2012). On the other hand, predicted rate coefficients obtained via the reduced-potential approach using a value of $C = -2.0$ from the appropriate linear function produces estimates that are within 13.5% of the calculated values considering the whole temperature range from Guillon & Stoecklin (2012) and clearly demonstrates the superiority of the approach.

The reduced-potential scaling method described here was employed with the He-HF data from Yang et al. (2015) to estimate all HF state-to-state rotational deexcitation for $j = 6-20$ in collisions with para-H_2. Furthermore, H-HF rate coefficients were also estimated using the trend in C taken from Figure 3.20. In using the reduced-potential approach, the following parameters were adopted for HF collisions with He, H_2, and H: $\mu_{He} = 3.3353$ u, $\mu_{H_2} = 1.818$ u, $\mu_H = 0.9596$ u, $\varepsilon_{He} = 39.68$ cm^{-1} (Moszynski et al. 1994), $\varepsilon_{H_2} = 359.0$ cm^{-1} (Guillon et al. 2008), and $\varepsilon_H = 100.0$ cm^{-1} (Stark & Werner 1996). The full set of rate

coefficients are available in LAMDA format for use in modeling HF and may be regarded as reasonable estimates until explicit calculations become available.

Table 3.3: The lower states j', the optimized values of C, the change in C (ΔC), and the slope of the derived linear functions.

j'	C	ΔC	Slope
0	1.7	1.1	-0.94
1	0.6	0.8	-0.72
2	-0.2	0.6	-0.56
3	-0.8	0.4	-0.44
4	-1.2	0.2	-0.36
5	-1.4	0	-0.32
6	-1.5	0	-0.30
7	-1.6	0	-0.28
8	-1.7	0	-0.26
9	-1.8	0	-0.24
10	-1.9	0	-0.22
11	-2.0	0	-0.20
12	-2.1	0	-0.18
13	-2.2	0	-0.16
14	-2.3	0	-0.14
15	-2.4	0	-0.12
16	-2.5	0	-0.10
17	-2.6	0	-0.08
18	-2.7	0	-0.06
19	-2.8	0	-0.04
20	-2.9	0	-0.02

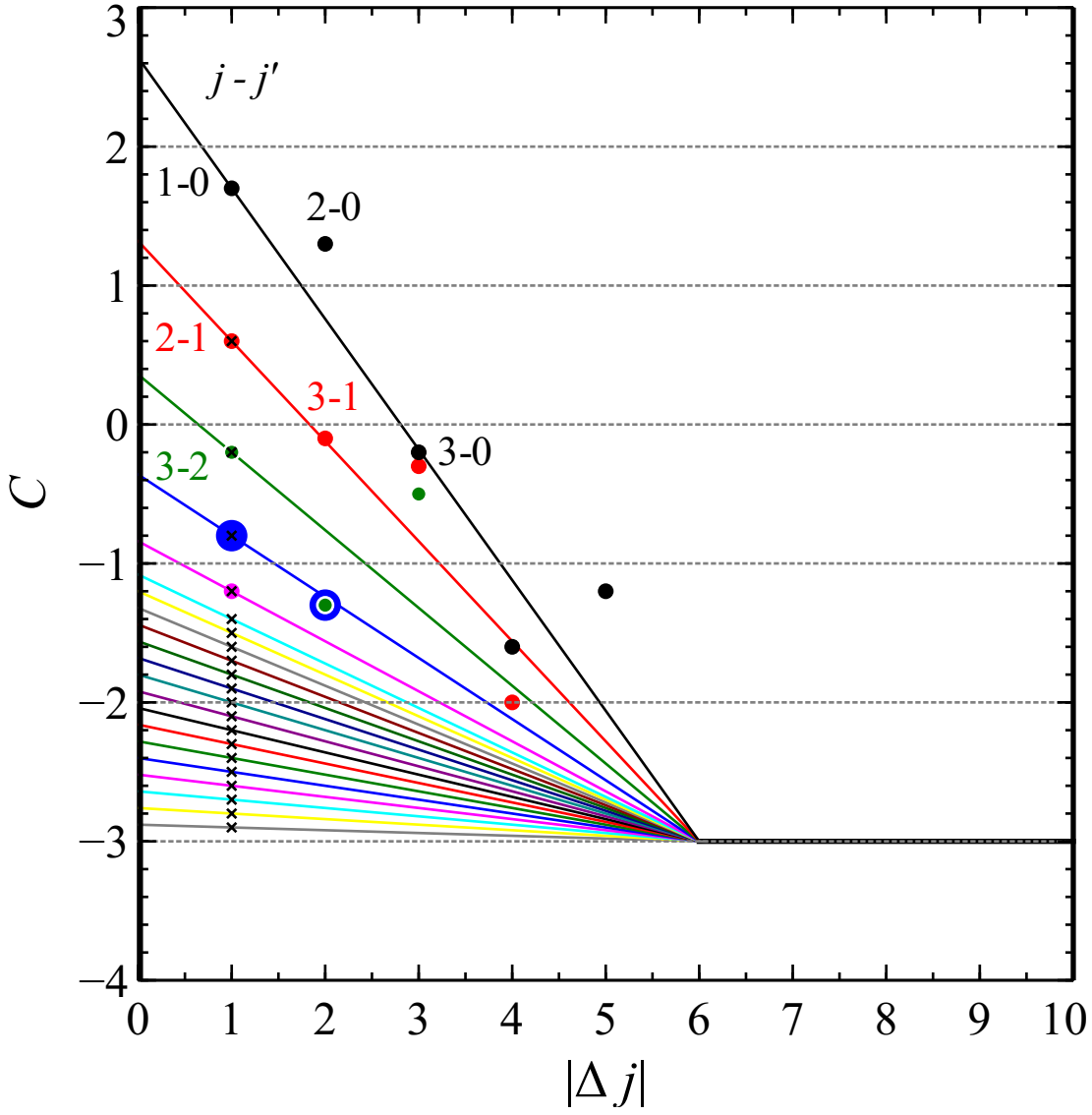

Figure 3.20: The phenomonological constant C as a function of $|\Delta j|$. Due to the linear decrease of C with j' and the convergence around $|\Delta j| = 6$ and $C = -3$, the slope and y-intercept can be obtained for each transition and the value of C can be predicted.

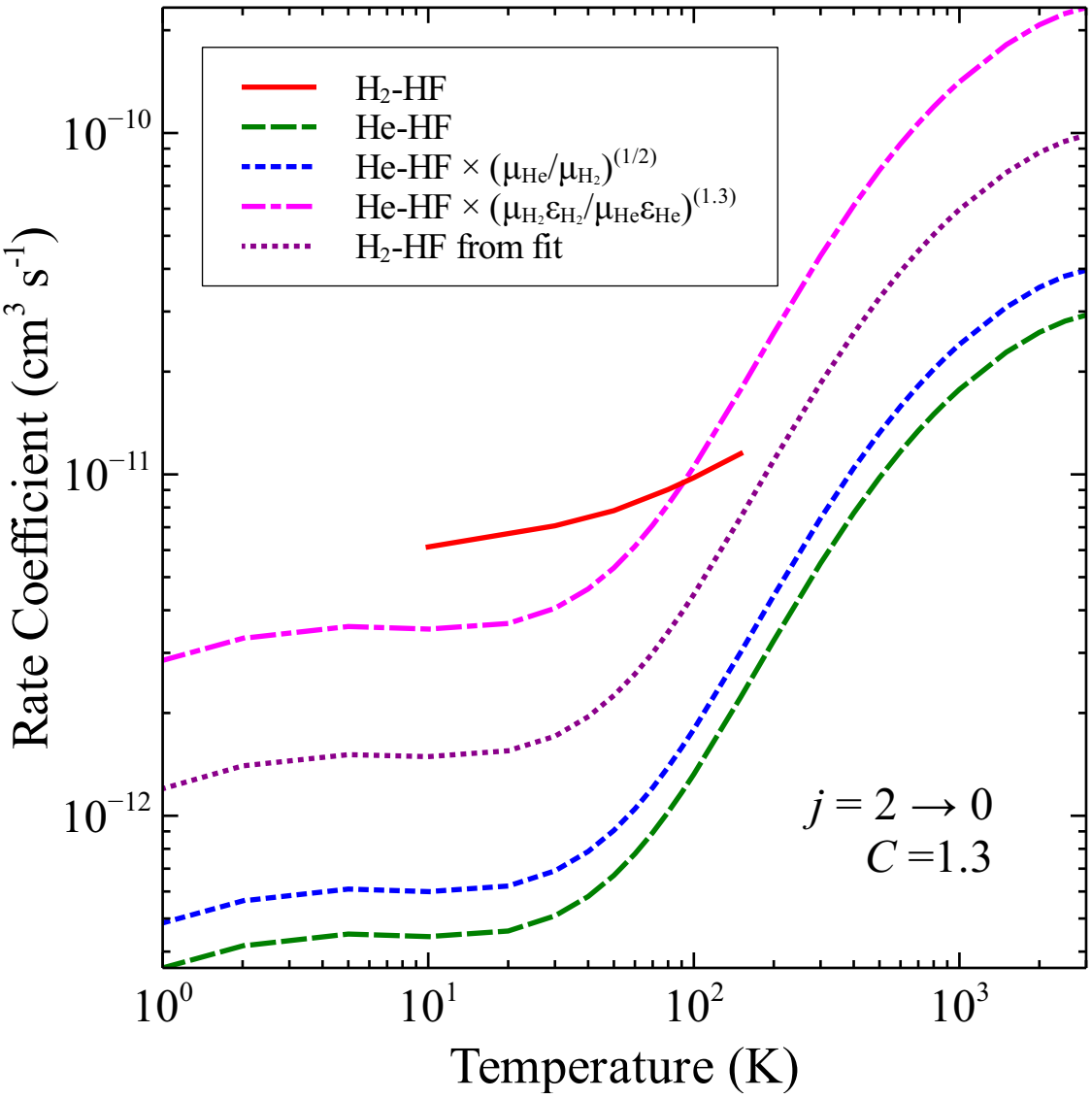

Figure 3.21: Rate coefficients for the deexcitation of HF($j = 2 \rightarrow 0$) due to para-H_2 (Guillon & Stoecklin 2012) and He (Yang et al. 2015) and a comparison of standard reduced-mass scaling and reduced-potential scaling for para-H_2 rate coefficients with $C = 1.3$.

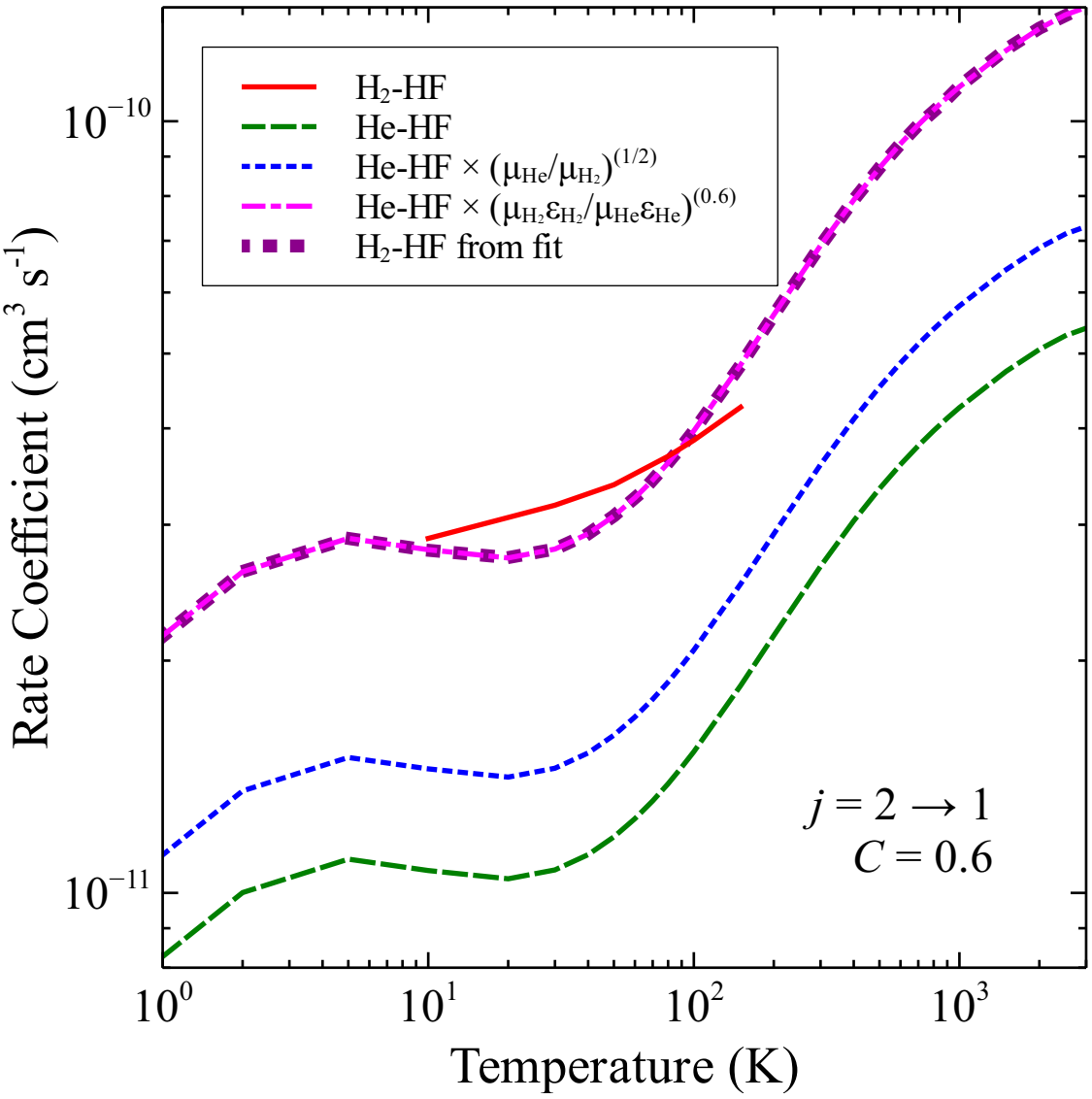

Figure 3.22: Same as Figure 3.21 for the deexcitation of HF($j = 2 \rightarrow 1$).

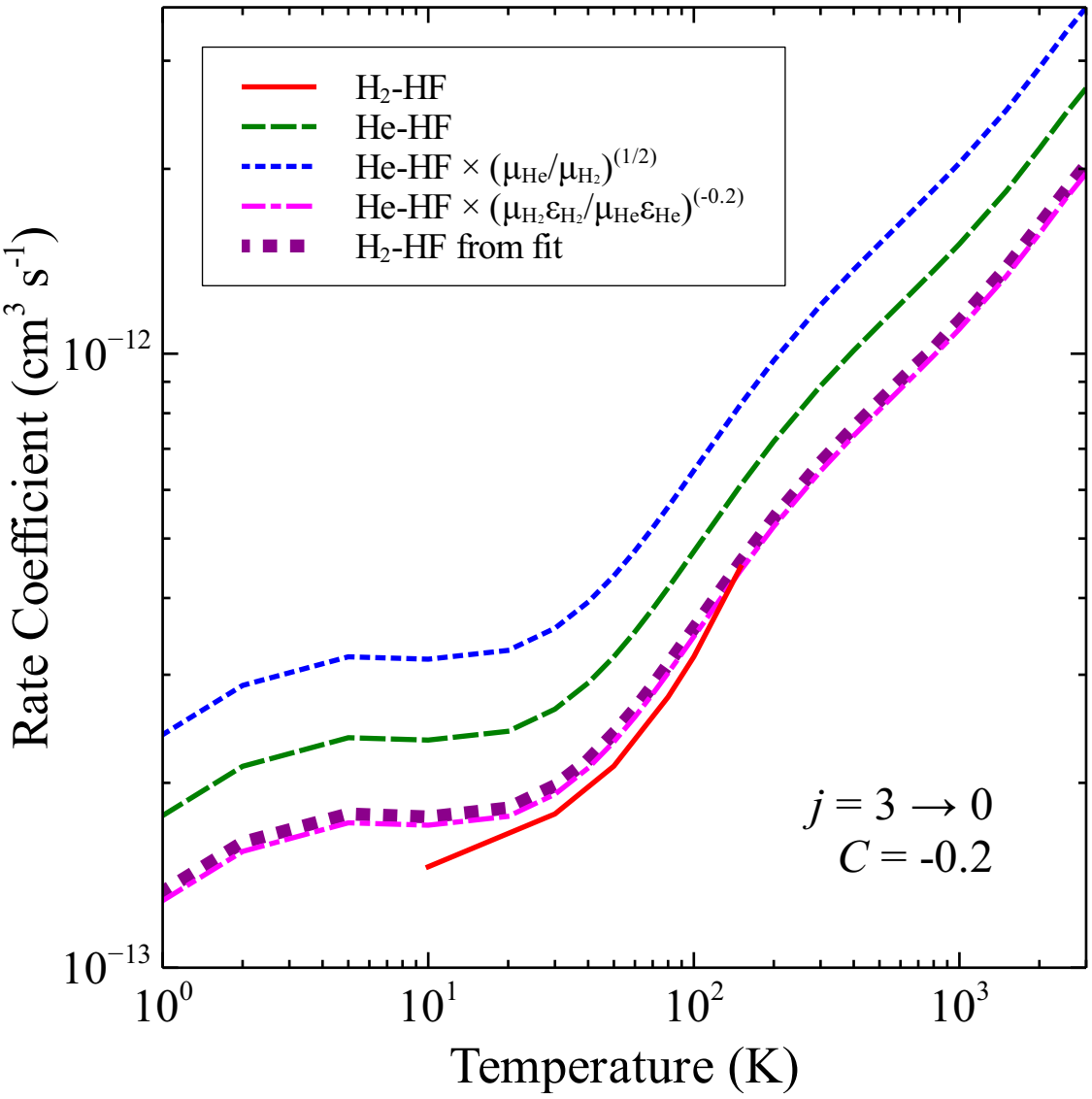

Figure 3.23: Same as Figure 3.21 for the deexcitation of HF($j = 3 \rightarrow 0$).

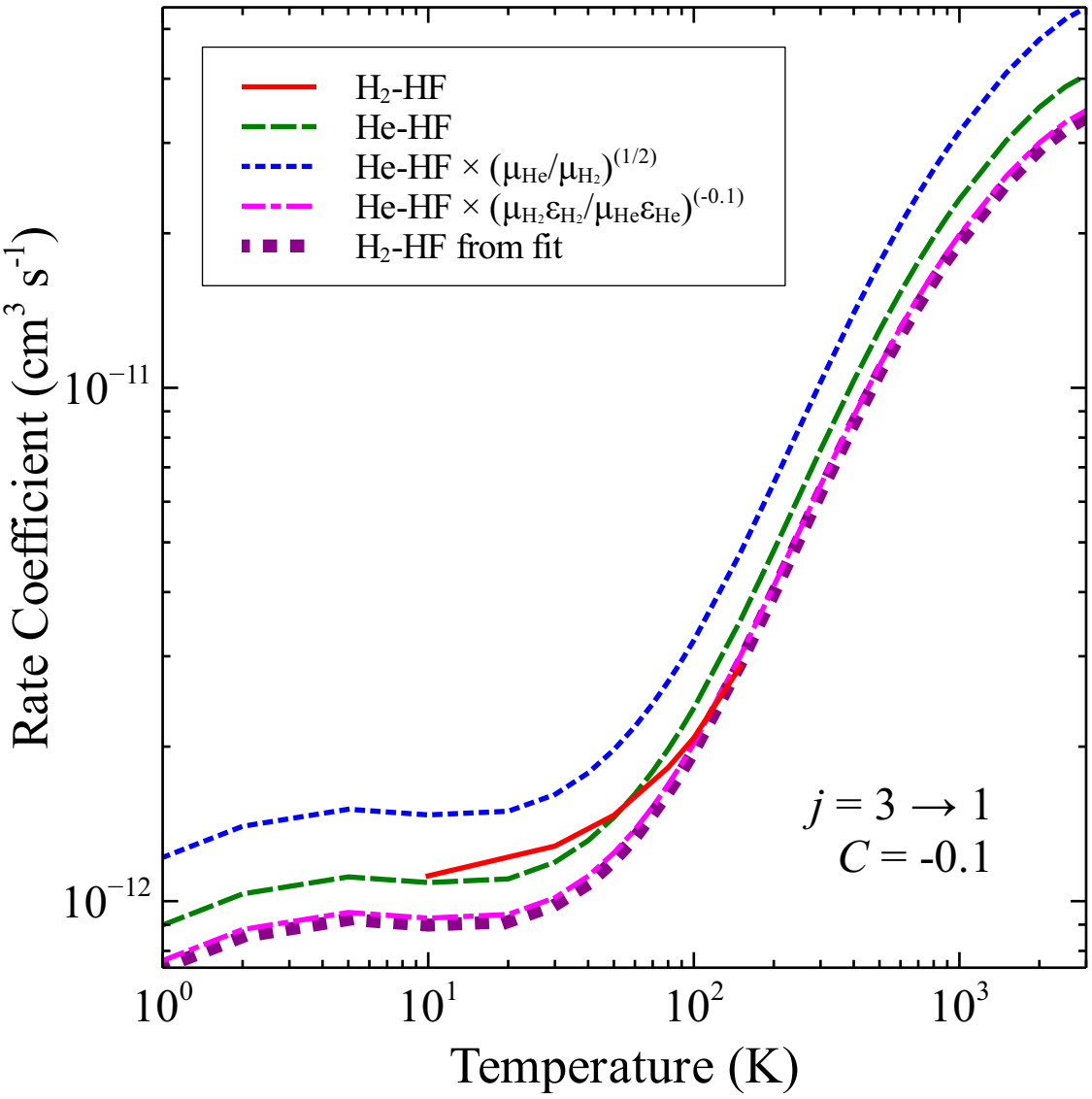

Figure 3.24: Same as Figure 3.21 for the deexcitation of HF($j = 3 \rightarrow 1$).

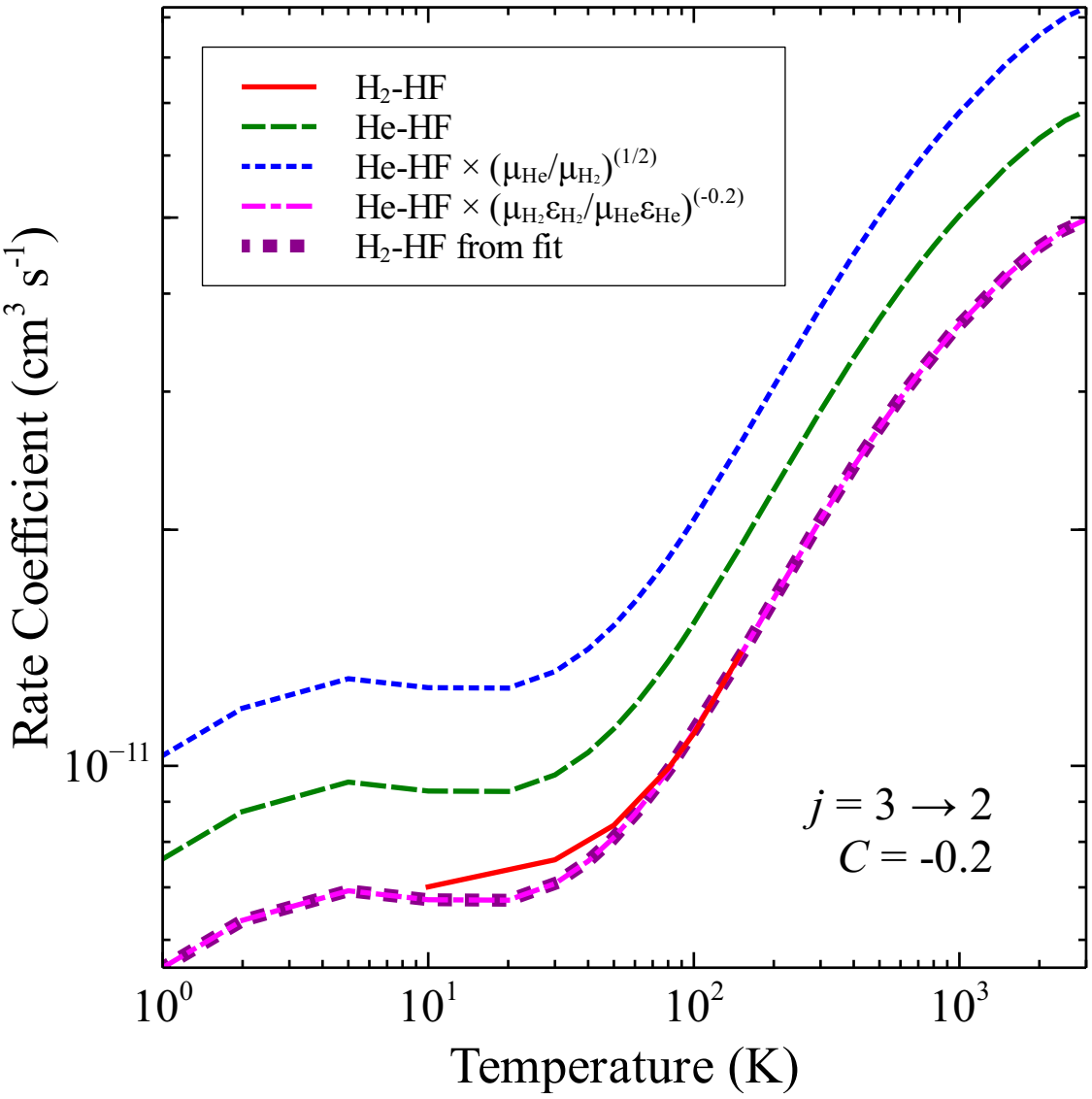

Figure 3.25: Same as Figure 3.21 for the deexcitation of HF($j = 3 \rightarrow 2$).

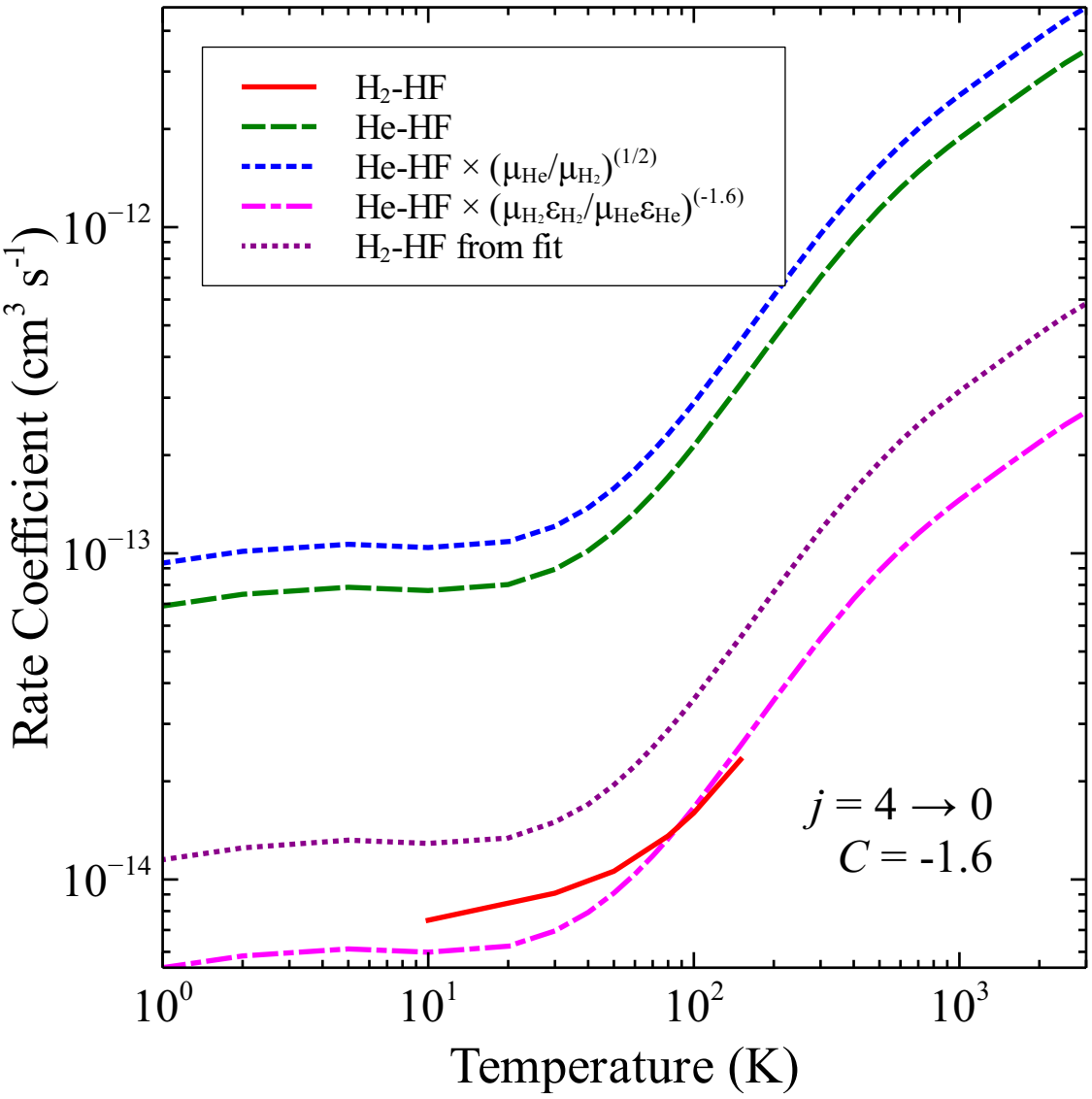

Figure 3.26: Same as Figure 3.21 for the deexcitation of HF($j = 4 \rightarrow 0$).

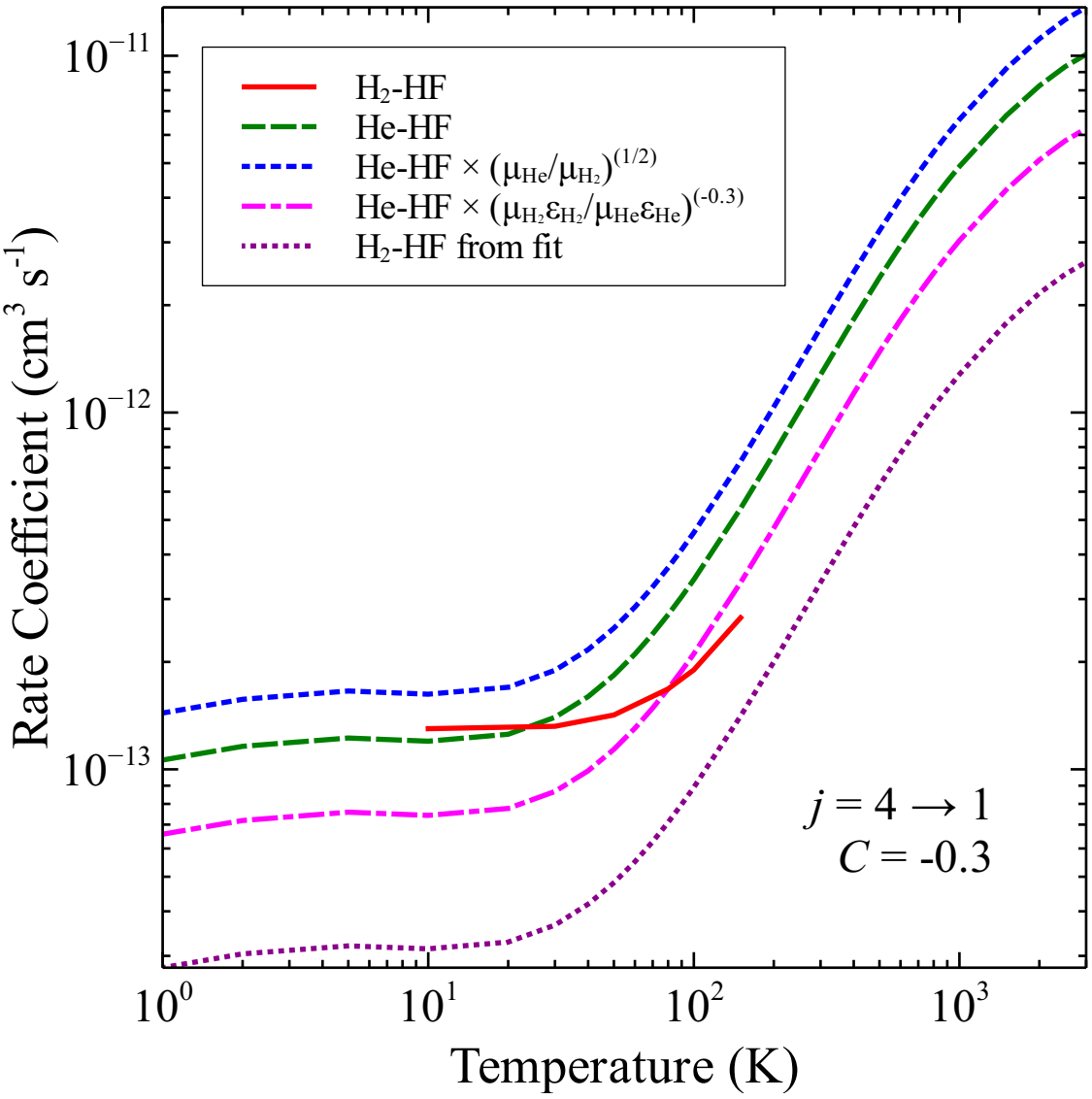

Figure 3.27: Same as Figure 3.21 for the deexcitation of HF($j = 4 \rightarrow 1$).

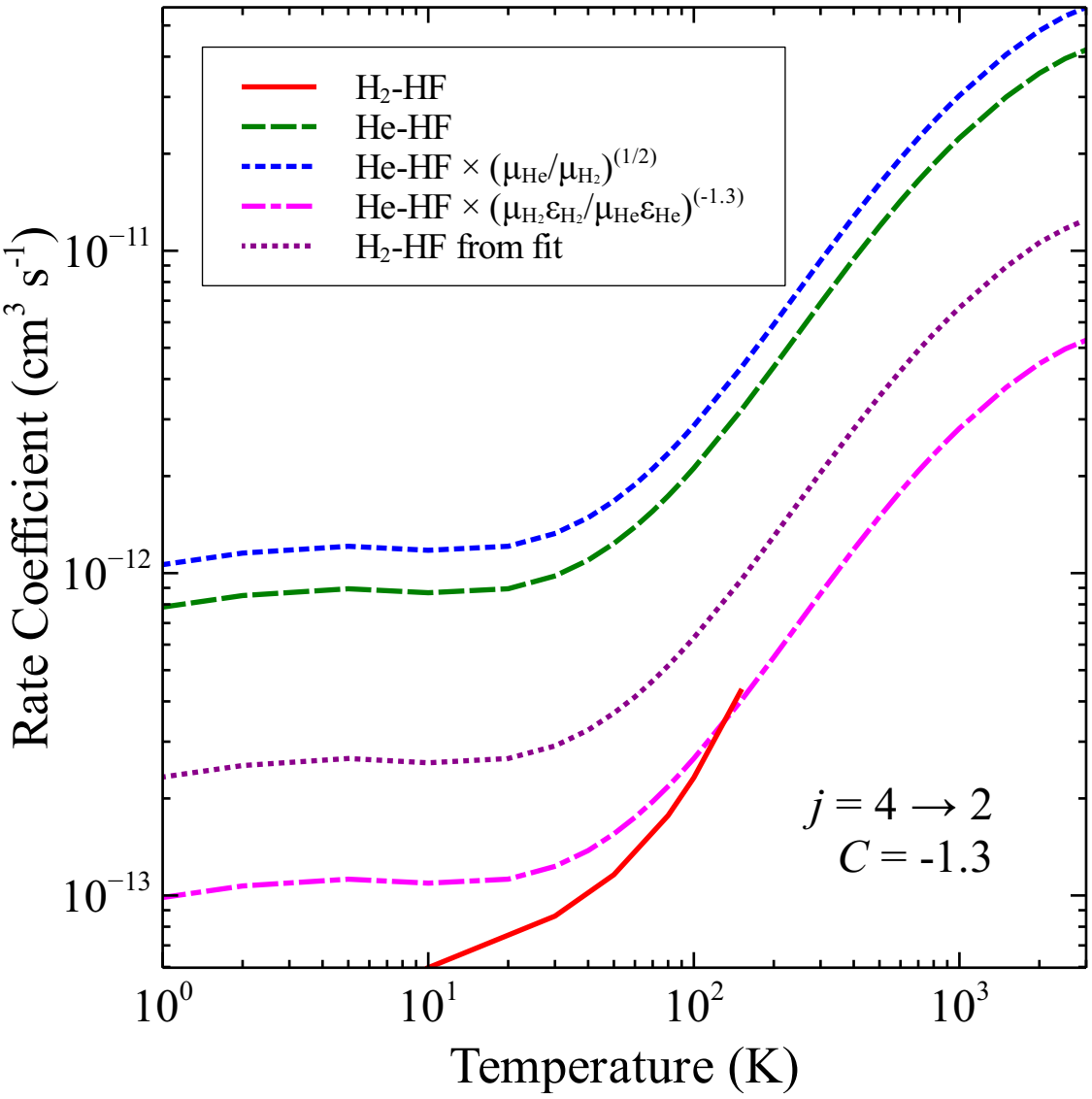

Figure 3.28: Same as Figure 3.21 for the deexcitation of HF($j = 4 \rightarrow 2$).

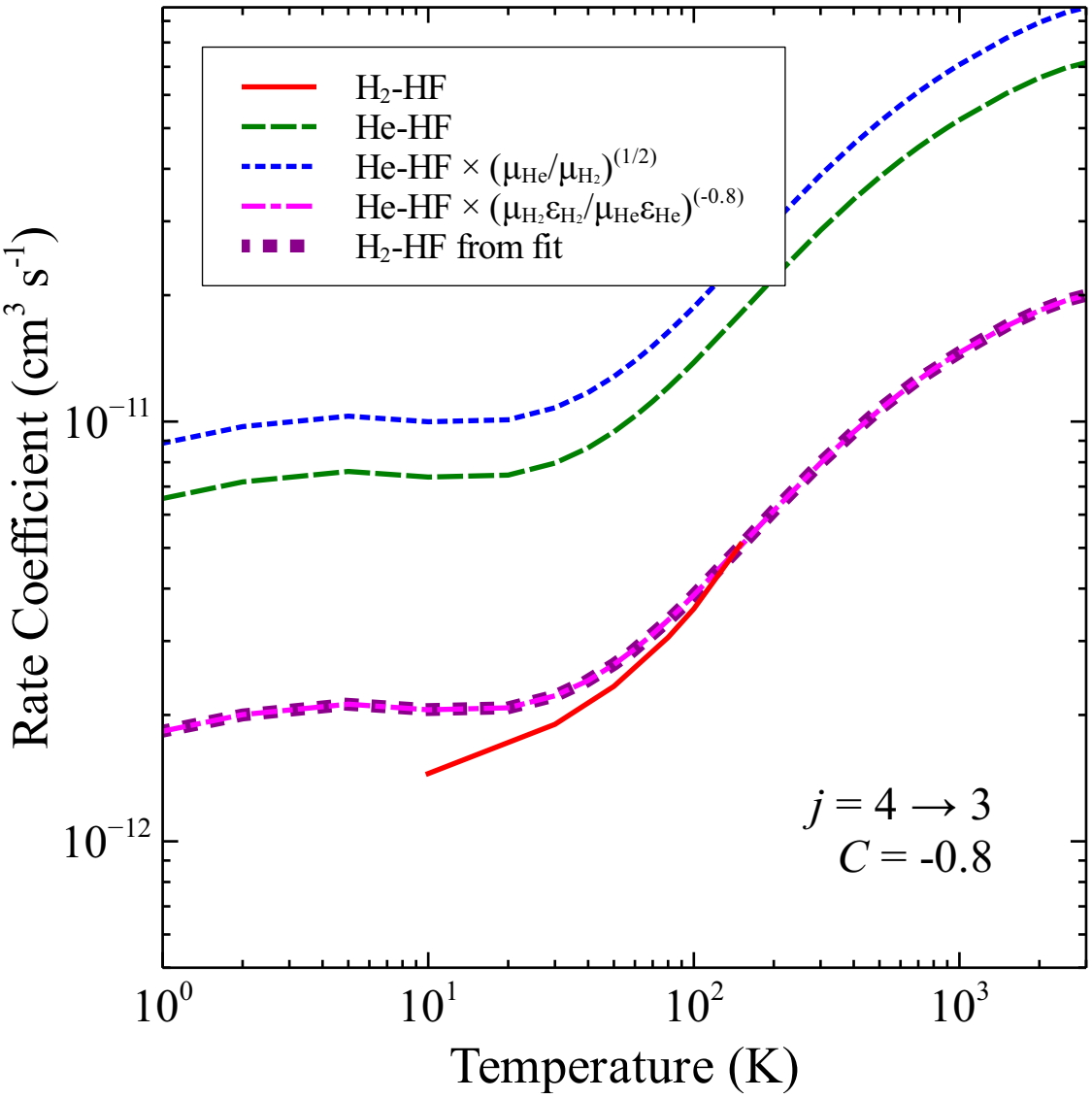

Figure 3.29: Same as Figure 3.21 for the deexcitation of HF($j = 4 \rightarrow 3$).

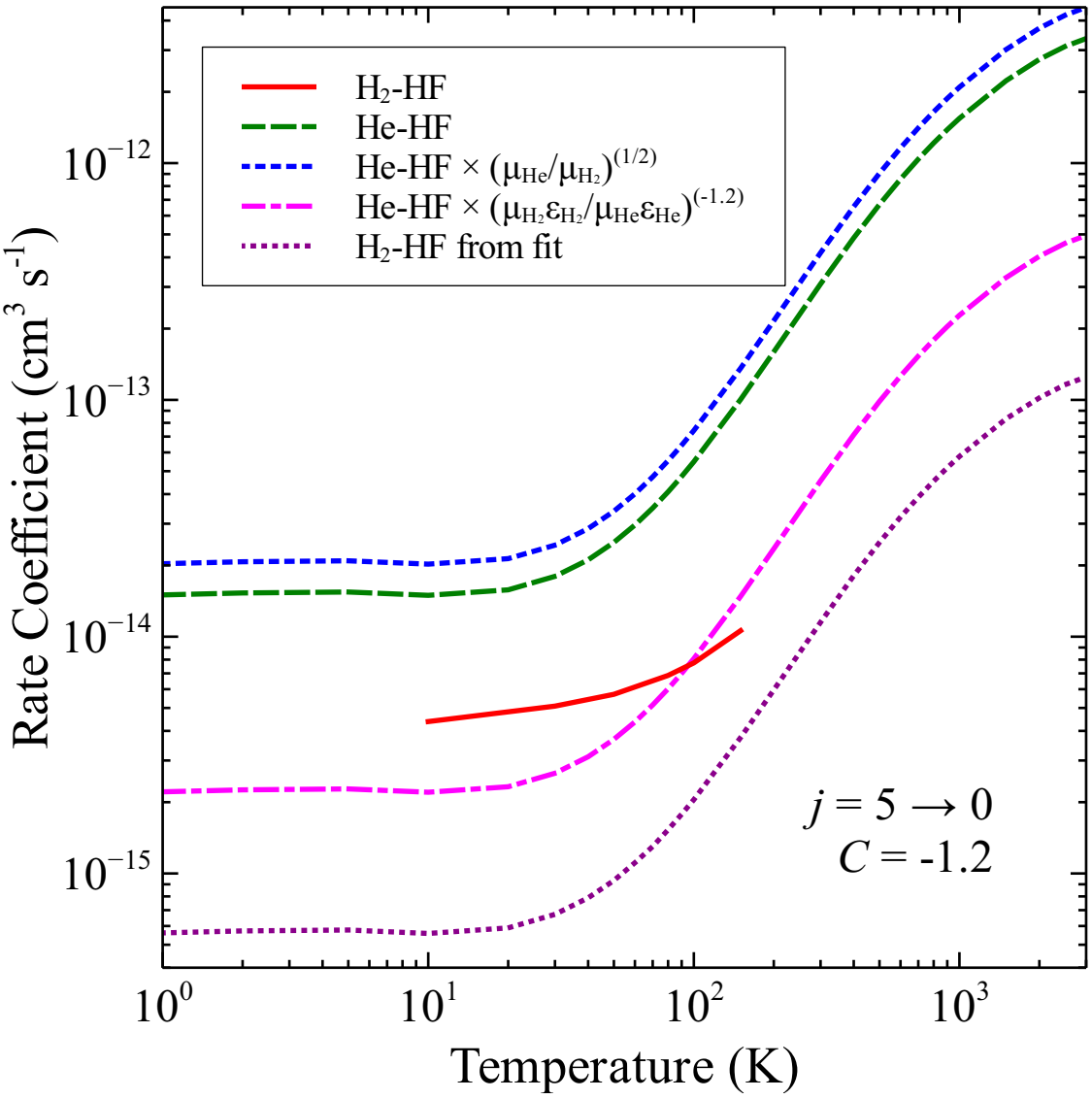

Figure 3.30: Same as Figure 3.21 for the deexcitation of HF($j = 5 \rightarrow 0$).

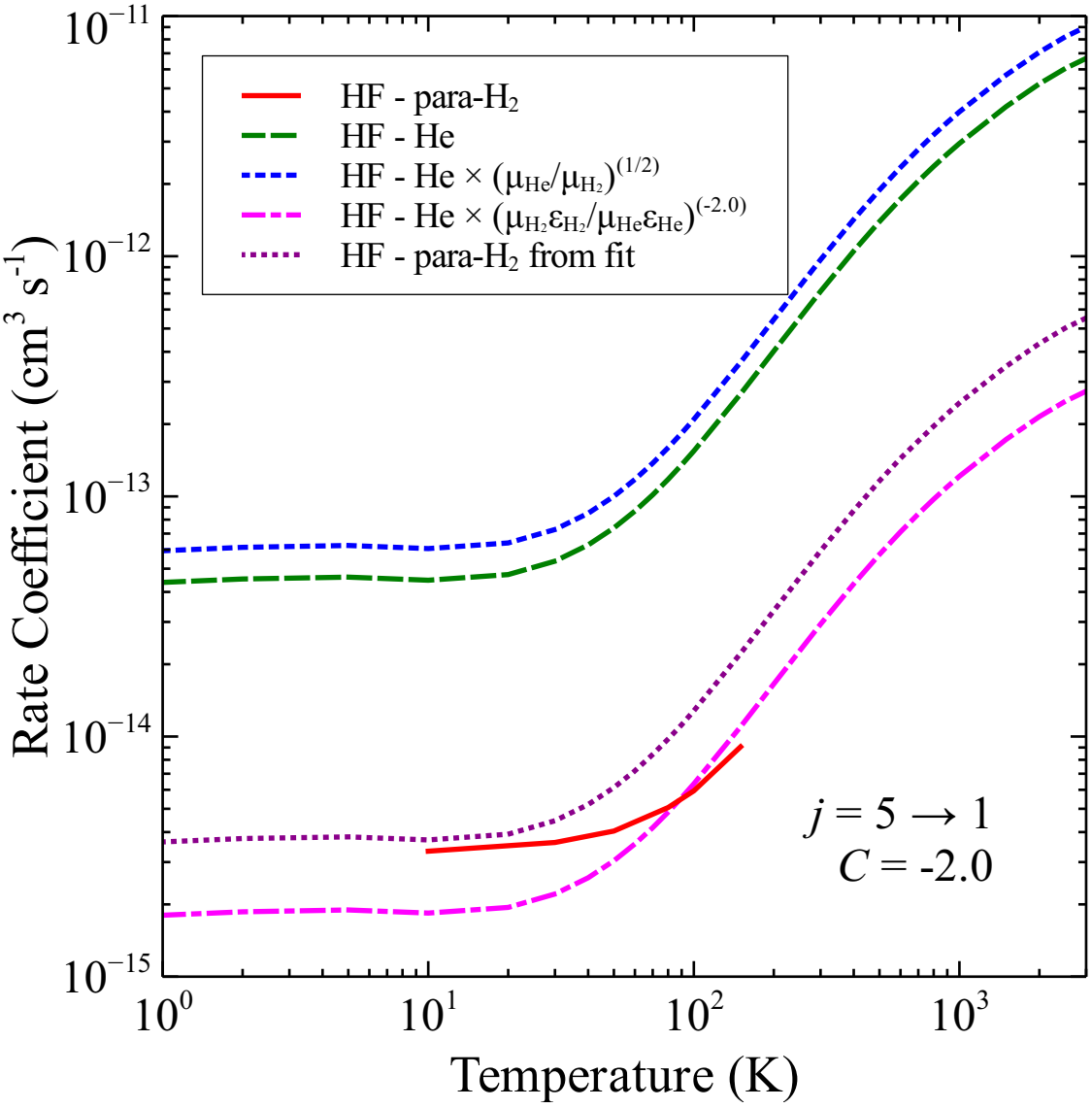

Figure 3.31: Same as Figure 3.21 for the deexcitation of HF($j = 5 \rightarrow 1$).

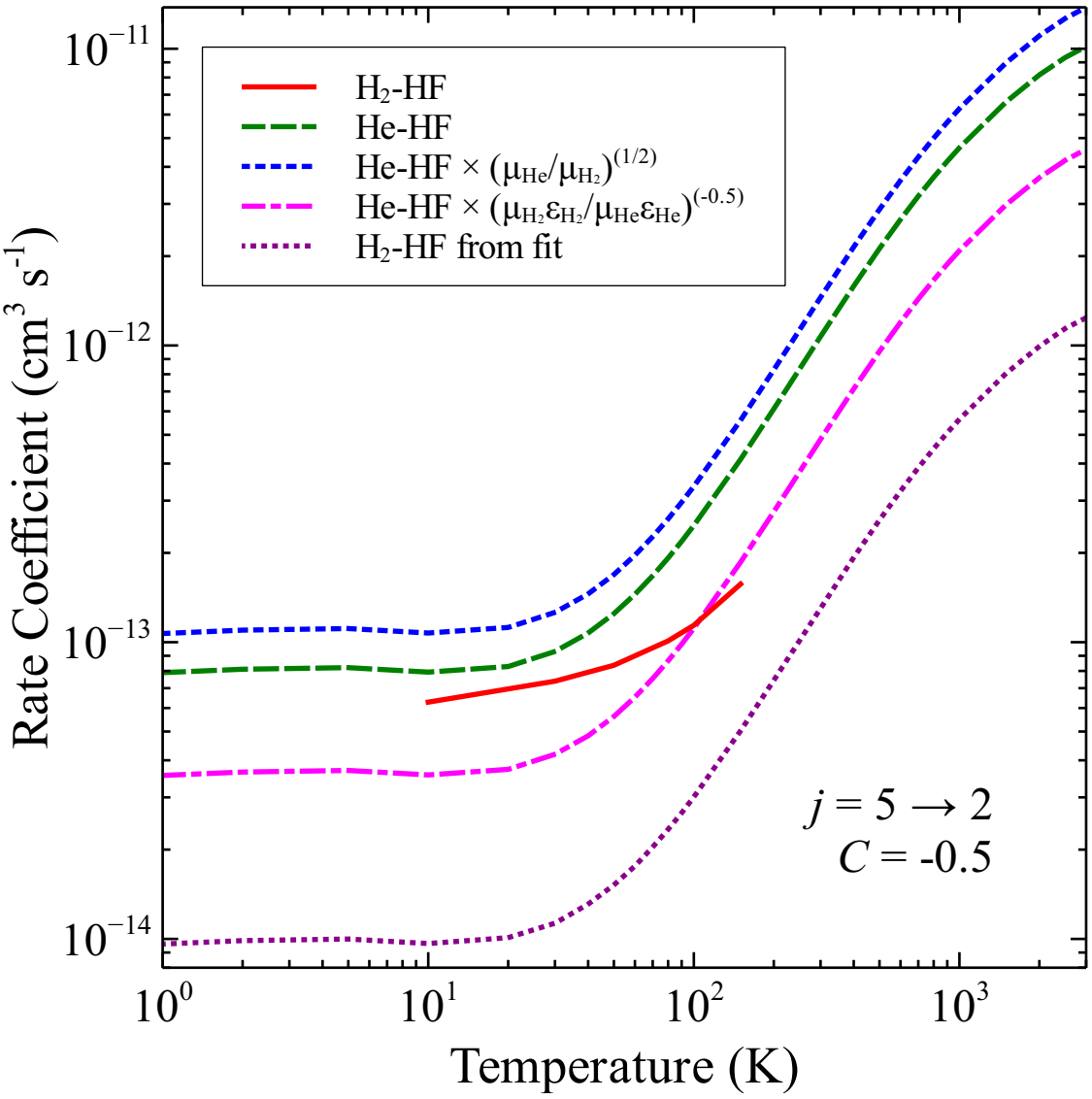

Figure 3.32: Same as Figure 3.21 for the deexcitation of HF($j = 5 \rightarrow 2$).

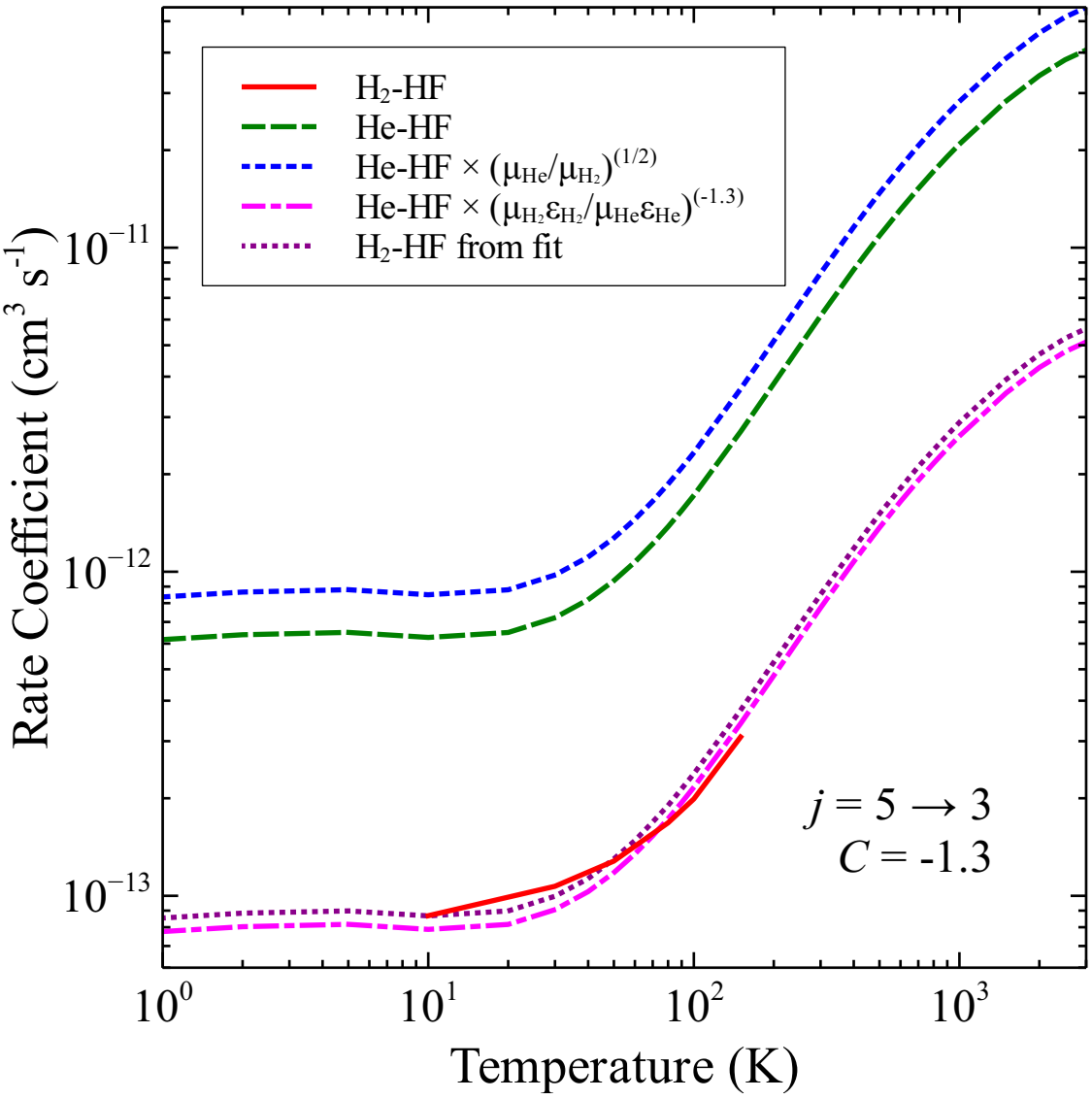

Figure 3.33: Same as Figure 3.21 for the deexcitation of HF($j = 5 \rightarrow 3$).

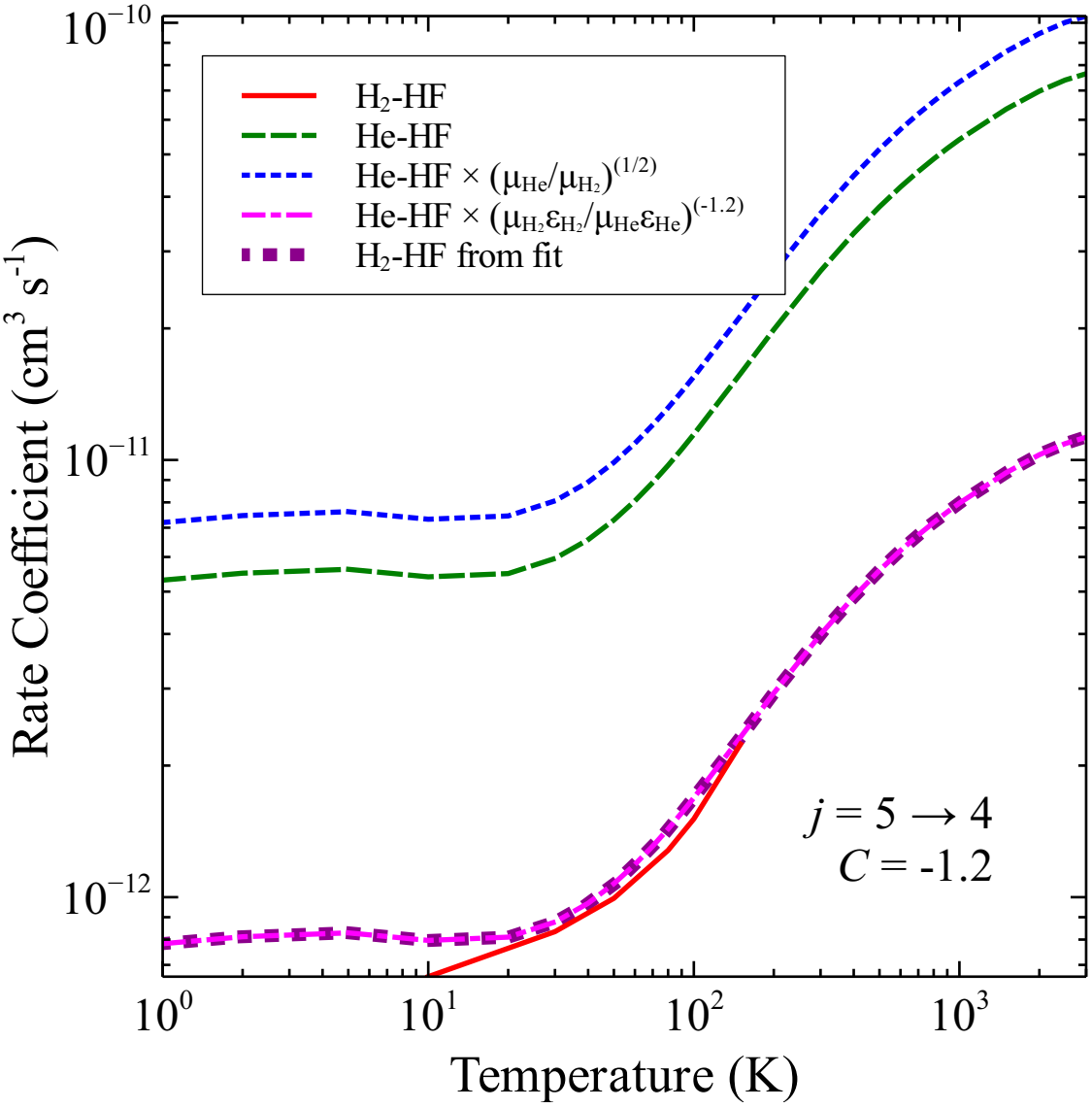

Figure 3.34: Same as Figure 3.21 for the deexcitation of HF($j = 5 \rightarrow 4$).

Chapter 4

Modeling the Early Universe

The Standard Model of Big Bang Nucleosynthesis theoretically predicts the abundances of light nuclei in the early universe (Wagoner et al. 1967), and as the universe expanded and evolved, molecules such as H_2, HD, and LiH formed in the primordial gas. These molecules dominate the subsequent cooling of the gas (Saslaw & Zipoy 1976; Matsuda et al. 1969) which allows primordial clouds to collapse into the first generation of stars. These first stars and their resulting supernovae contaminated the universe with metals which we can observe today (Bromm et al. 2003; Songaila 2001) and were the progenitors of the heavy elements necessary for life on earth.

Recent observations from the Wilkinson Microwave Anisotropy Probe (WMAP) produced data which indicates an early reionization of the universe at $z \sim 20$ (Bennett et al. 2003). The interpretation of the reionization at this redshift is that the radiation of primordial massive stars photoionized the universe (Ripamonti et al. 2002). These first stars therefore would need to be very massive, around 100 to 1000 solar masses (Abel et al. 1997, 2002; Omukai & Palla 2001), and they would emit a signature spectrum. We expect molecular hydrogen line emission from these low-temperature star-forming regions, and recent models discuss and predict the spectra of H_2 (Ripamonti et al. 2002) and HD (Kamaya & Silk 2003) in the first generation of stars. Since we have not yet directly observed star formation in the early universe, models are needed to study primordial cloud collapse in this era.

This chapter focuses on the development of a more robust model of Recombination Era astrochemistry and the prediction of emission spectra of a primordial cloud as it collapses into a first generation star. This model specifically enhances the current notions by including

i) updated rovibrationally resolved molecular collisional data for the species H_2, HD, and H_2^+, ii) an expansive chemical network including more than 10 molecules with consideration of deuterated, ionized, and excited species, iii) a heat equation coupled to the chemical network instead of pre-computed cooling functions, and iv) preliminary non-thermal zero-dimensional hydrodynamic simulations of a collapsing primordial cloud. The resulting synthesized NLTE spectra of the first generation stars are examined for detection by current and future observational facilities.

4.1 Rovibrational Astrochemistry in the Recombination Era

The latest potential energy surfaces and scattering calculations as well as experimental results have made recent contributions to the atomic and molecular data needed as input for Recombination Era chemistry. The main colliders of the early universe are electrons, H, H^+, He, and H_2, and collisional rate coefficients with these species now exist for many systems. Rotational collisional rate coefficients for molecules of interest, such as H_2 and HD, have been theoretically calculated (Forrey et al. 1997; Schaefer 1990) and compare consistently with experimental results (Tejada et al. 2008; Krems 2008). However, vibrationally resolved rate coefficients also exist (Fonseca dos Santos et al. 2013; Nolte et al. 2012) and must be included as an integral part of primordial cloud collapse models. Each vibrational channel is an important chemical pathway that affects the thermal balance and dynamical evolution of primordial gas in the early universe (Coppola et al. 2011a, 2012). These updated molecular collisional data, primarily both rotationally and vibrationally resolved rate coefficients for H_2, HD, and H_2^+, have been input into the chemical network. A developmental version of the spectral synthesis package Cloudy (Ferland et al. 2013) was used to model this primordial gas.

A LAMDA-type file for H_2^+ was created to hold the relevant molecular data (see Appendix A regarding LAMDA files). The level energies and spontaneous decay rates for the O, P, and S branches of H_2^+ were obtained from the UGA Molecular Opacity Project

Database [http://www.physast.uga.edu/ugamop/mainh2p.html] (Stancil 1994). Inelastic vibrationally resolved cross sections for the H-H_2^+ collision system were obtained from Krstiċ (2002). These cross sections had values in the energy range $0.02 - 8.0$ eV, and for use in this work the cross sections were extrapolated to both lower and higher energies. For the low-energy extrapolation, the analytic functional form $1/v$ was applied, scaled to the value of the cross section at the lowest energy. This process yielded low-energy, constant rate coefficients. For the high-energy extrapolation, the cross sections were made constant, equal to the calculated value at the largest energy. This constant simply allowed the integration of cross sections (convoluted with a Maxwellian) over an energy range to produce rate coefficients which exhibit typical behavior for temperatures of astrophysical interest. The resulting calculated rate coefficients span the temperature range $2 - 10,000$ K.

The chemical network expands upon those from Galli & Palla (1998), Stancil et al. (1998), Omukai (2000), Lepp et al. (2002), Glover & Abel (2008), and Gay et al. (2011) and includes over 300 reactions[1] consisting of electrons, H, H^+, H^-, H_2, H_2*, H_2^+, H_3^+, D, D^+, D^-, HD, HD*, HD^+, H_2D^+, D_2, D_2^+, HD_2^+, D_3^+, He, He^+, He^{+2}, HeH^+, HeD^+, Li, Li^+, Li^{+2}, Li^{+3}, Li^-, LiH, LiH^+, LiD, and LiD^+. The network includes creation, destruction, and level-changing reactions and considers the processes of associative detachment, radiative association, collisional dissociation, charge transfer, photoionization, photodissociation, dissociative excitation/recombination, dissociative attachment, collisional (de)excitation, and photodetachment due to distortion photons. These reactions result in chemical rate equations consisting of coupled stiff ordinary differential equations of the form

$$\frac{dn_i}{dt} = \alpha_{\rm form}(T) n_j n_k - \alpha_{\rm dest}(T) n_i n_l - \zeta_{\rm dest}(T) n_i, \tag{4.1}$$

where n_i is the particle density of the reactant species i, $\alpha_{\rm form}$ is the formation rate coefficient, $\alpha_{\rm dest}$ is the destruction rate coefficient, and $\zeta_{\rm dest}$ is the photo-destruction rate.

[1]The * indicates excitation.

The primordial fractional abundances (denoted by $f_{\rm x}$, where x is the species) relative to H for He and Li are 0.079 and 1×10^{-10}, respectively, and the D/H abundance ratio is 1.65×10^{-5} as given by Pettini & Bowen (2001). The shape and intensity of the incident radiation field is purely cosmic microwave background (CMB) radiation with a temperature given by

$$T_{\rm CMB} = T_0(1+z), \tag{4.2}$$

where z indicates redshift and $T_0 = 2.725 \pm 0.002$ K (Mather et al. 1999). We adopt a Lambda Cold Dark Matter cosmology (ΛCDM, also referred to as the standard model of Big Bang cosmology) which is a six-parameter model based on a flat universe and dominated by a cosmological constant, Λ, and cold dark matter (CDM), where $\Omega_{\rm b} = 0.0464$ is the ratio of the baryonic matter density to the critical density to close the universe, $\Omega_{\rm c} = 0.235$ is ratio of cold dark matter density to critical density, $\Omega_{\rm m} = \Omega_{\rm c} + \Omega_{\rm b} = 0.2814$ is the matter density, $\Omega_{\rm r} = 8.23 \times 10^{-5}$ is the radiation density, $\Omega_{\rm m} + \Omega_\Lambda = 1$, and $h = 0.697$ is the Hubble parameter (WMAP9 data, Hinshaw et al. 2013). The Hubble rate within this cosmology is given by

$$H(z) = H_0\sqrt{\Omega_\Lambda + \Omega_{\rm m}(1+z)^3 + \Omega_{\rm r}(1+z)^4}, \tag{4.3}$$

where $H_0 = 100h = 69.7$ km s^{-1} Mpc^{-1} is the Hubble constant. The number density of hydrogen nuclei is given by

$$n_{\rm H}(z) = 1.123 \times 10^{-5}\frac{\Omega_{\rm b}h^2}{1 + 3.9715 f_{\rm He}}(1+z)^3, \tag{4.4}$$

adopted from Switzer & Hirata (2008).

Although Hirata & Padmanabhan (2006) first included vibrational level populations of H_2^+ in models of the early universe, they used a less robust chemical network, did not include collisional quenching, and adopted a pre-computed molecular heating function for H_2. Actually, most primordial models thus far have only incorporated pre-computed heating/cooling functions which are not a good estimate of the cooling rate (Coppola et al. 2011b; Yoshida

et al. 2003). A pre-computed function neglects the evolution of molecular abundances, the effects due to the background radiation field, and reactive sinks or sources. The early universe chemical network presented here is coupled to the heat equation which is solved self-consistently with the CMB radiation field to ensure accurate predictions of the chemical composition and thermal properties of the gas. The net rate of heating of the gas is given by

$$\big(\Gamma - \Lambda\big) = \sum_{p} n^{(p)} \sum_{i>j} \big[n_i q^{(p)}_{i\rightarrow j}(T) - n_{ij} q^{(p)}_{j\rightarrow i}(T)\big](E_i - E_j), \tag{4.5}$$

where Γ represents contributions to heating, Λ represents the contributions to cooling, $\mathrm{n}^{(p)}$ is the number density of the perturber, n_i is the number density of molecules in level i, E_i is the energy of the level, and $q^{(p)}_{i\rightarrow j}(\mathrm{T})$ is the rate coefficient. The cooling rate, L_C — the energy loss by collisionally excited line radiation — for any excited level 2 to a lower level 1 per unit volume is given by

$$L_C = n n_1 q_{12}(T) h\nu_{21}, \tag{4.6}$$

where n is the gas volume density, n_1 is the density of the ground state of the emitting molecule, q_{12} is the rate coefficient, dependent on temperature, and $h\nu_{21}$ represents the energy of the emitted photon.

Finally, the usual approximation made in similar models of the early universe is that the rovibrational level populations are thermalized (in LTE) or the whole population resides in the ground state (see, for example Galli & Palla 1998). These crude approximations lead to inaccurate level populations and ultimately yield models that most likely do not agree with true astrophysical environments. Our primordial model therefore simultaneously solves for the non-thermal level populations, chemistry, hydrodynamics, and radiative transfer. Although the main cooling agent for the low-temperature primordial gas is rovibrational line emission by molecular hydrogen, the effects of other molecules such as H_2^+ and HD are examined here.

The change of abundance over time of this full primordial chemistry network was computed for a grid of 10,000 redshifts starting in the early recombination era ($z = 4000$) and ending with freeze-out ($z = 12$). The resulting fractional abundances of atoms in the network are shown in Figure 4.1, while molecular abundances are shown in Figure 4.2. The atomic ion abundances generally decrease as the universe cools and the ions combine with electrons to become neutral. This is easily seen with the primordial He^{+2} abundance as it decreases by several orders of magnitude and forms He^+ before finally recombining to neutral helium by the end of decoupling (at $z \sim 1100$ matter and radiation are fully decoupled). The atomic abundances agree well with Galli & Palla (1998), and the only substantial difference from Stancil et al. (1998) is a greater fraction of He^+ at $z = 1000$ which lasts until freeze-out. This discrepancy is caused by a larger fraction of helium in our model that resides in HeH^+ and HeD^+. The trend of increasing molecular abundance with time is also quite apparent. The cooler temperatures cause molecular collisional rates to drop and the abundances to increase. These abundances agree well with those shown in Figure 4 of Galli & Palla (1998) and Figures 1-2 of Stancil et al. (1998). The rovibrational level populations of H_2, H_2^+, and HD are shown in Figures 4.3 - 4.5 as a function of redshift. The level populations of H_2 and H_2^+ exhibit similar behavior found in the model of Coppola et al. (2011a) which does not consider rotational levels. The rovibrational level populations of HD, as well as the rotational level populations of H_2 and H_2^+ are presented here for the first time. The only exception are the H_2 and H_2^+ population diagrams of Alizadeh & Hirata (2011) at $z \sim 1142$ and Hirata & Padmanabhan (2006) at $z = 300$, respectively.

Figure 4.6 shows the formation and destruction rates for H_2^+. These rates compare well to Figure 4 of Stancil et al. (1998). The main formation process is radiative association, with earlier times having significant contributions from the associative detachment of H with H(n=2) and the HeH^+ mechanism, $H + HeH^+ \rightarrow H_2^+ + He$. At later times contributions from the reaction $H^+ + H^- \rightarrow e^- + H_2^+$ also become significant. The main destruction mechanism of H_2^+ is photodissociation for earlier times when $z \gtrsim 300$, but for later times, when the

redshift is less than $\sim$ 300, charge exchange with H and dissociative recombination also become dominant pathways of destruction.

Figures 4.7 - 4.8 show the formation and destruction rates for HD, respectively. The main pathways for creation involve molecular hydrogen via the D exchange reactions $H_2 + D \rightarrow H + HD$ and $H_2 + D^+ \rightarrow H^+ + HD$. This is not surprising since this is well-known to be the major source of HD in diffuse interstellar clouds (Dalgarno et al. 1973). The destruction rates for HD are likewise dominated by the reverse D exchange reactions.

Finally, the level populations for $z = 300$ are shown in Figure 4.9, along with lines that indicate LTE populations for the radiation and matter temperatures at $k_{\rm B}T_{\rm CMB} = 0.0707$ eV and $k_{\rm B}T_{\rm m} = 0.0662$ eV, respectively. In contrast to the results of Hirata & Padmanabhan (2006), we find Boltzmann level populations for H_2^+. This is not surprising since Hirata & Padmanabhan (2006) did not include collisions in their model, and it is collisions that dominate the excitation. The density exceeds the critical density in this regime, and any deexcitation from the upper levels is outweighed by collisions which drive the level populations to LTE.

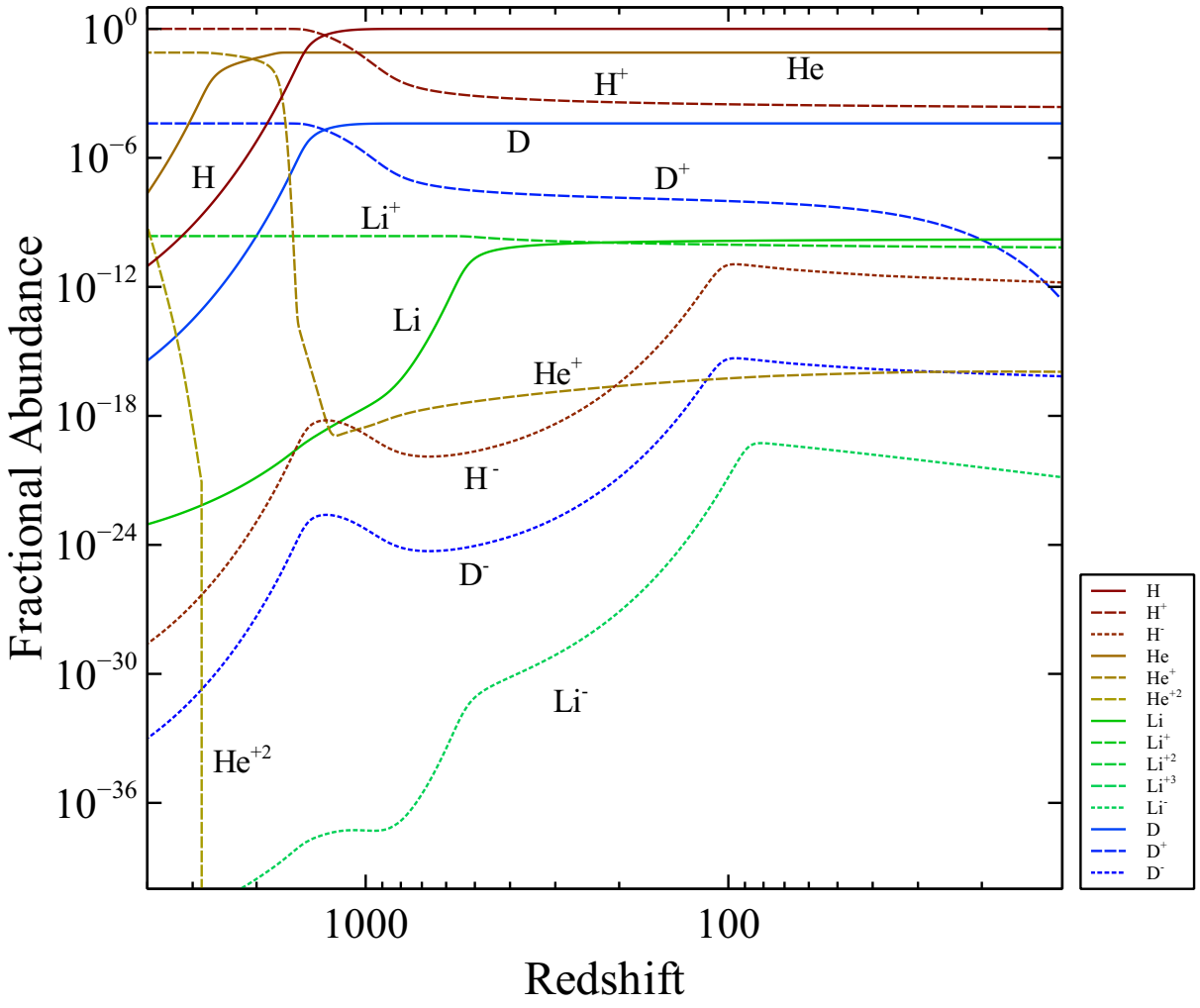

Figure 4.1: Fractional abundances ($n_i/n_{\rm H}$) of atoms in Recombination Era primordial gas. Neutral species are denoted by solid lines, cations by dashed lines, and anions by dotted lines.

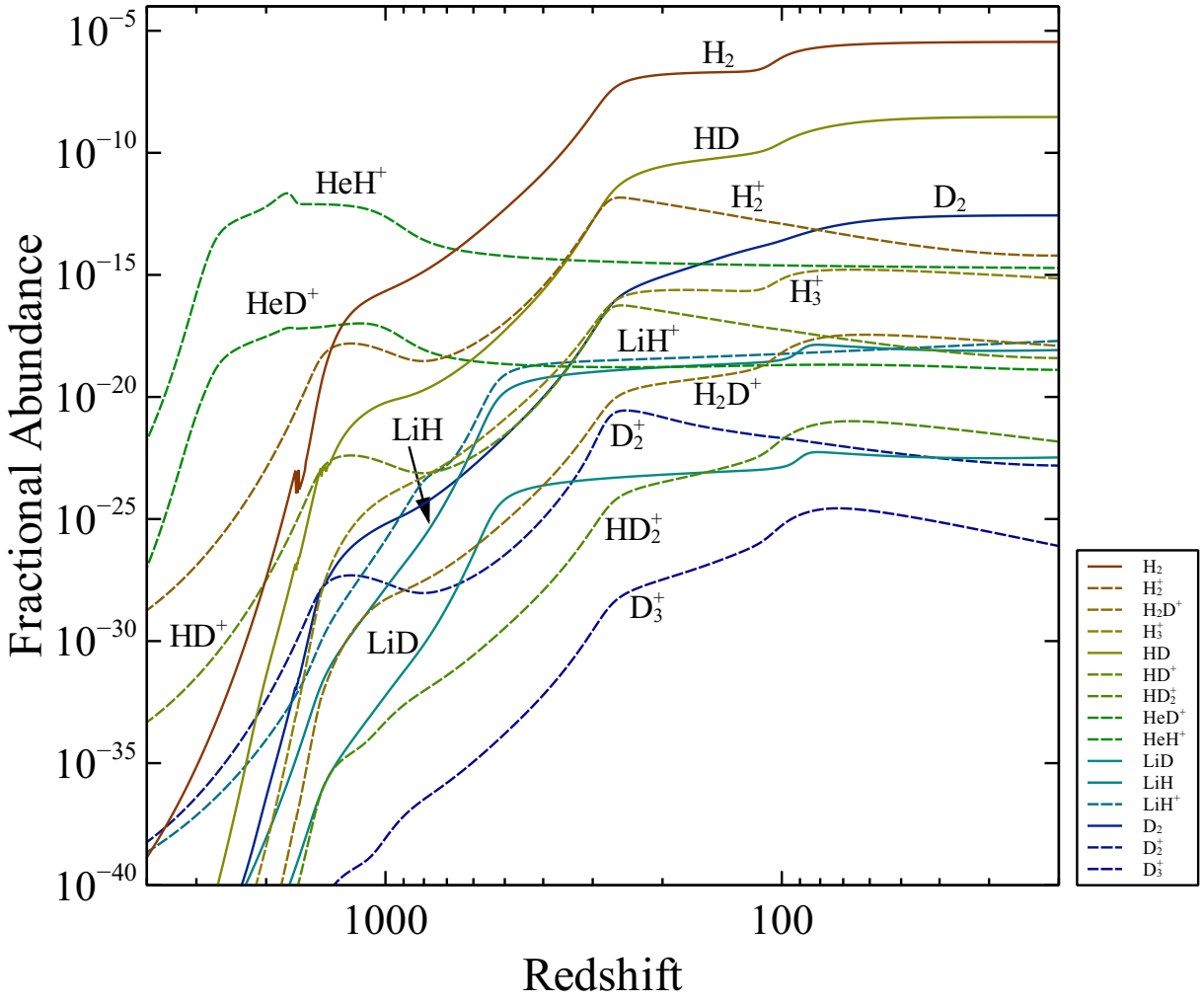

Figure 4.2: Fractional abundances of molecules in Recombination Era primordial gas. Neutral species are denoted by solid lines while cations are denoted by dashed lines.

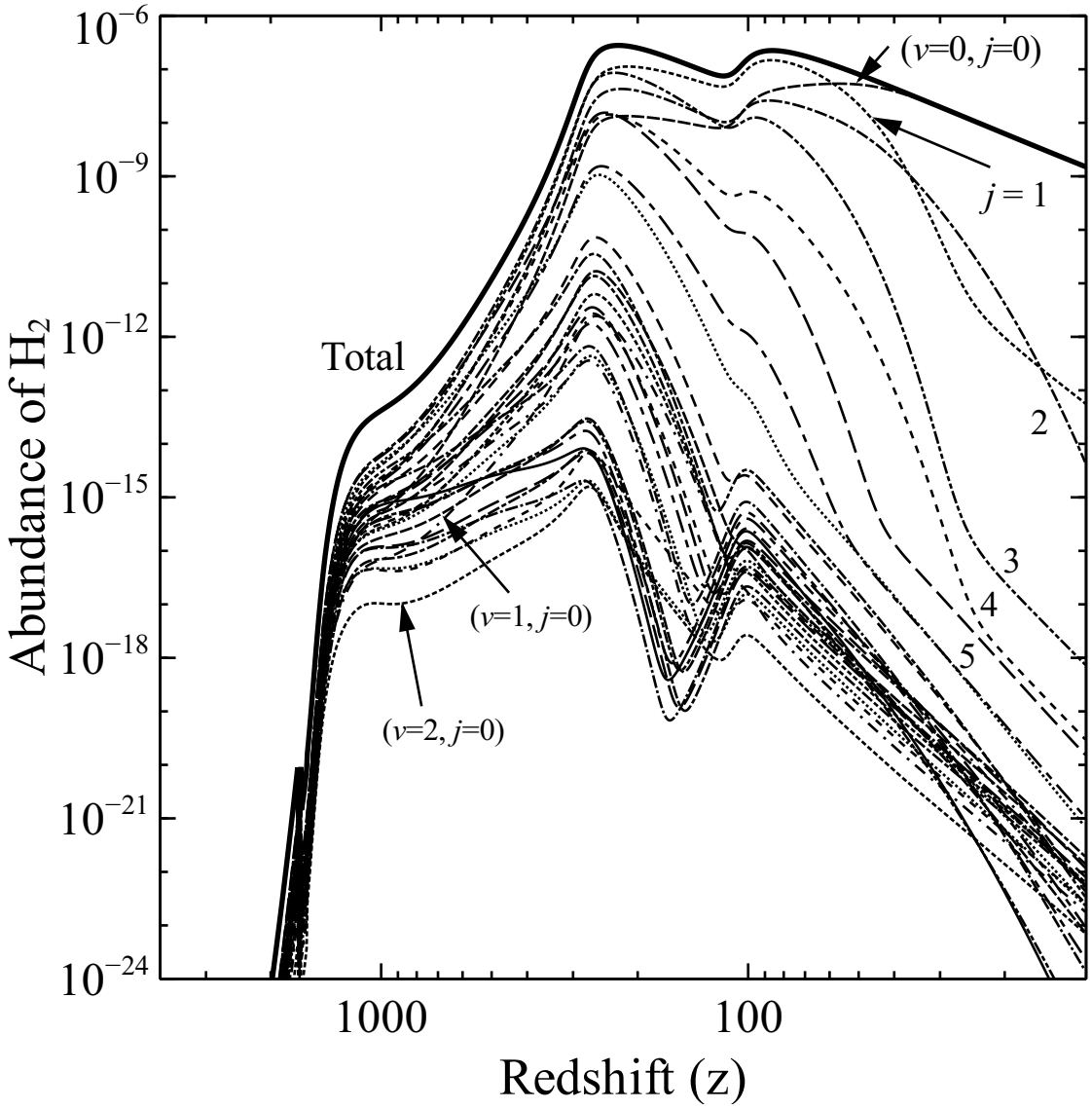

Figure 4.3: Rovibrationally resolved level populations of H_2 in the Recombination Era for the 30 lowest levels. The solid line indicates the total abundance.

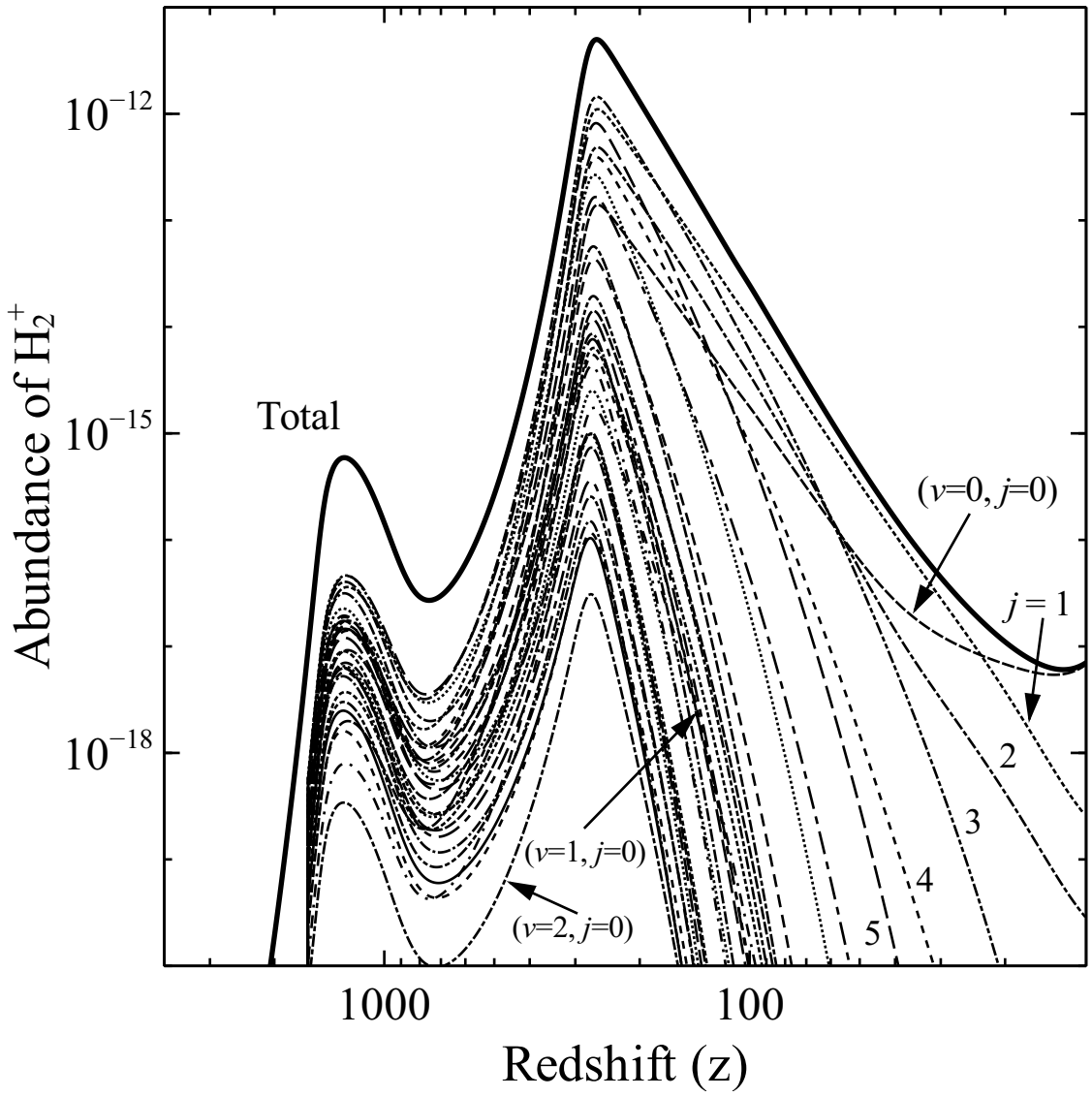

Figure 4.4: Same as Figure 4.3 for H_2^+.

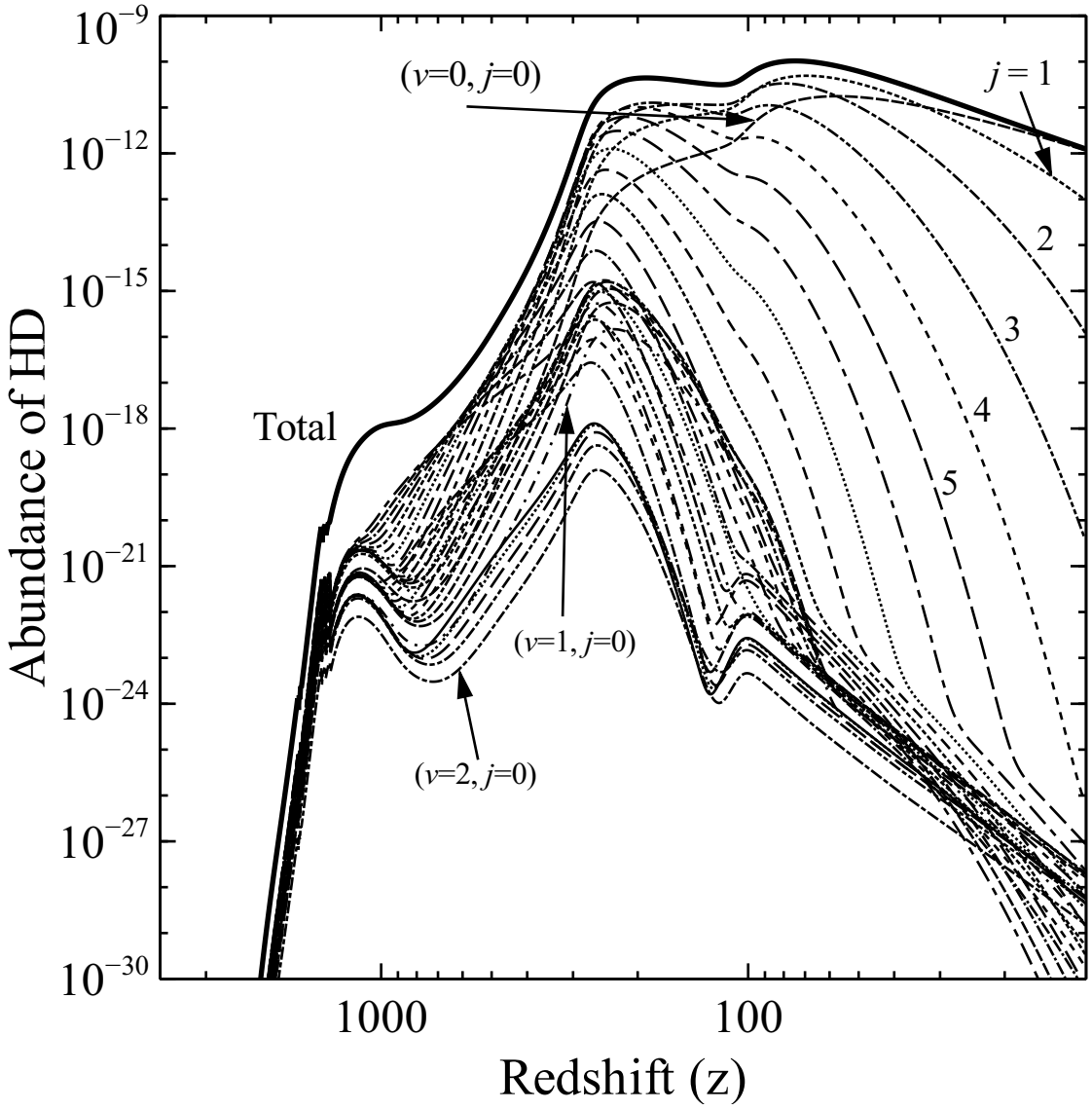

Figure 4.5: Same as Figure 4.3 for HD.

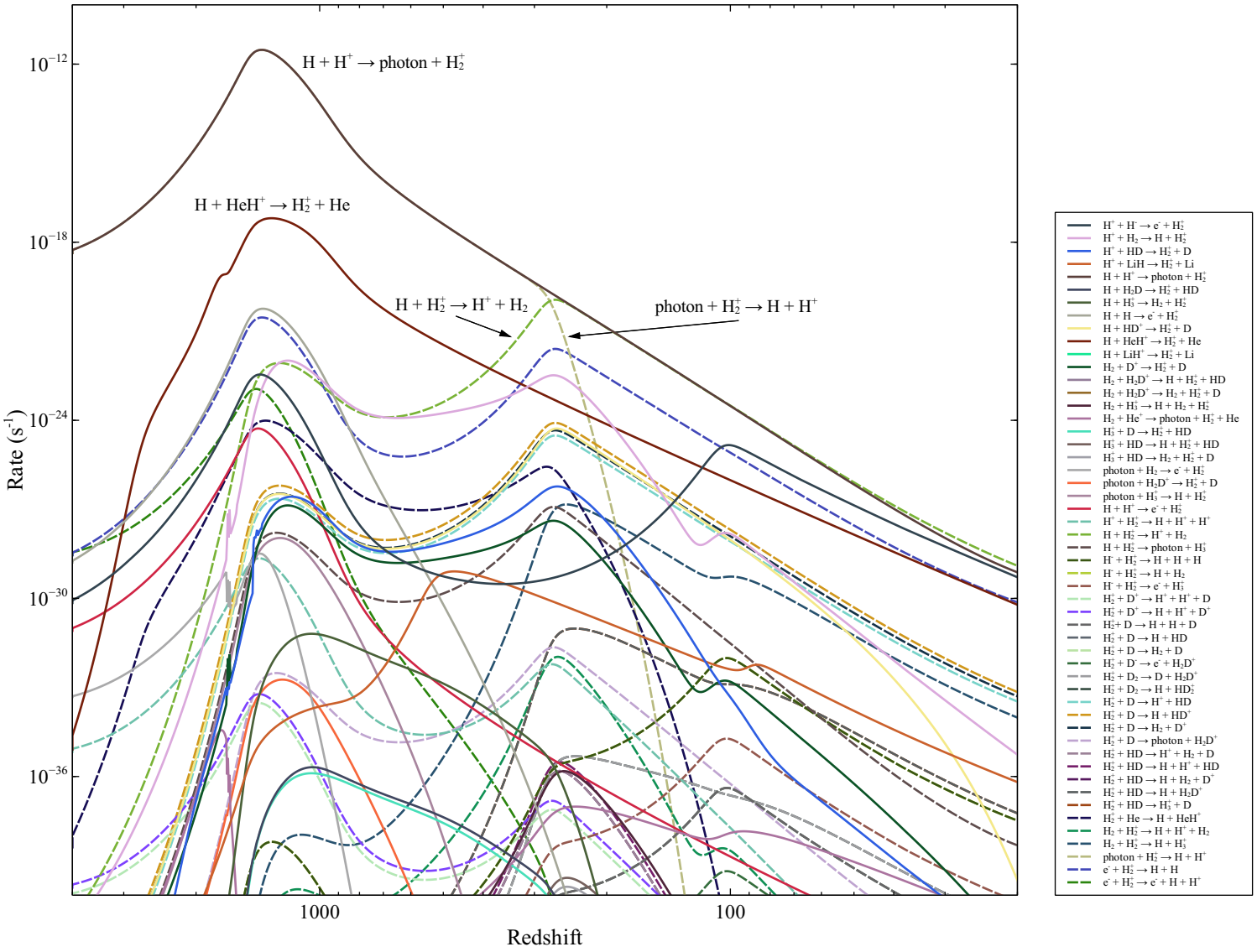

Figure 4.6: Rates of formation (solid lines) and destruction (dotted lines) for H_2^+ in the Recombination Era. The dominant processes are highlighted.

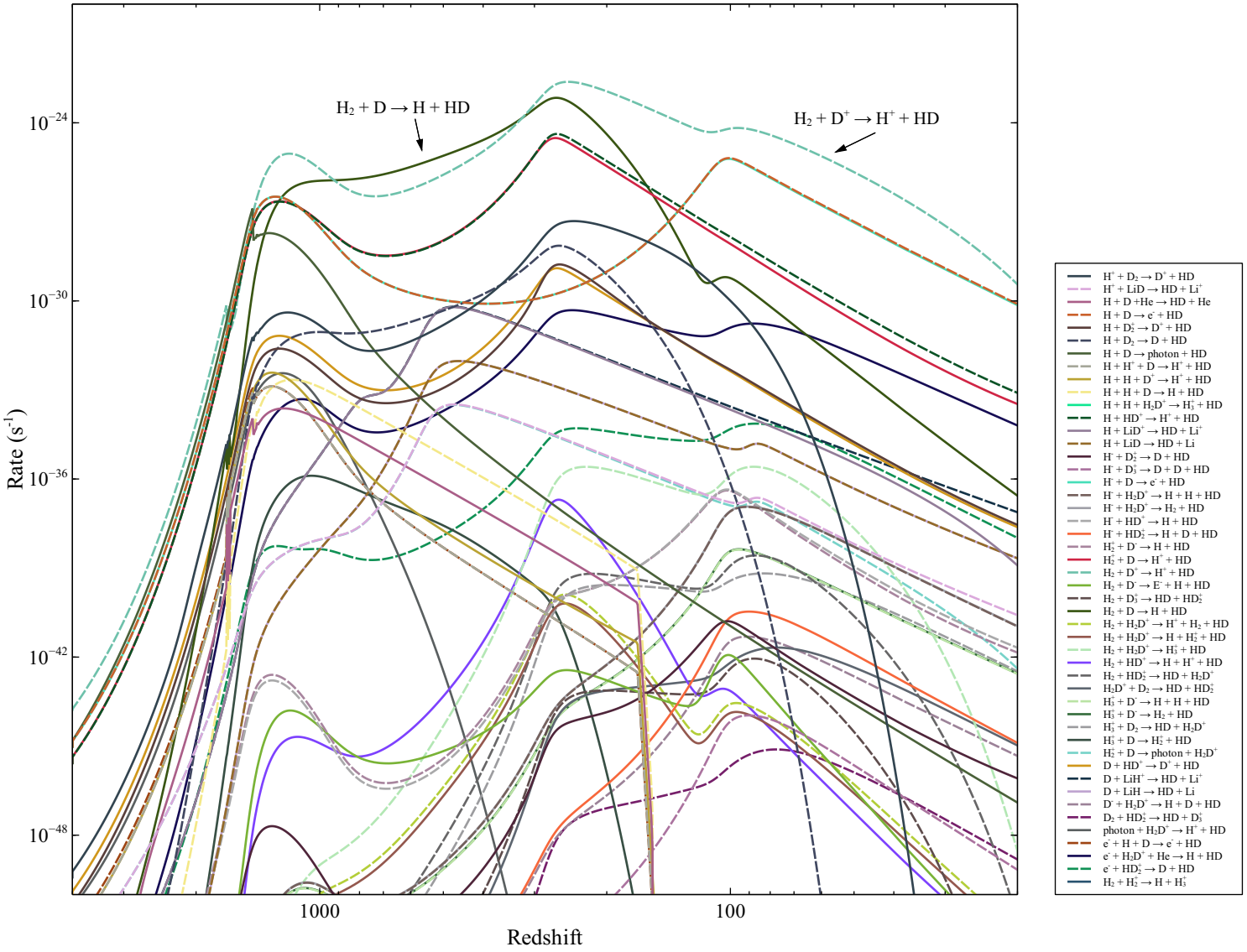

Figure 4.7: Rates of formation for HD in the Recombination Era. The dominant processes are highlighted.

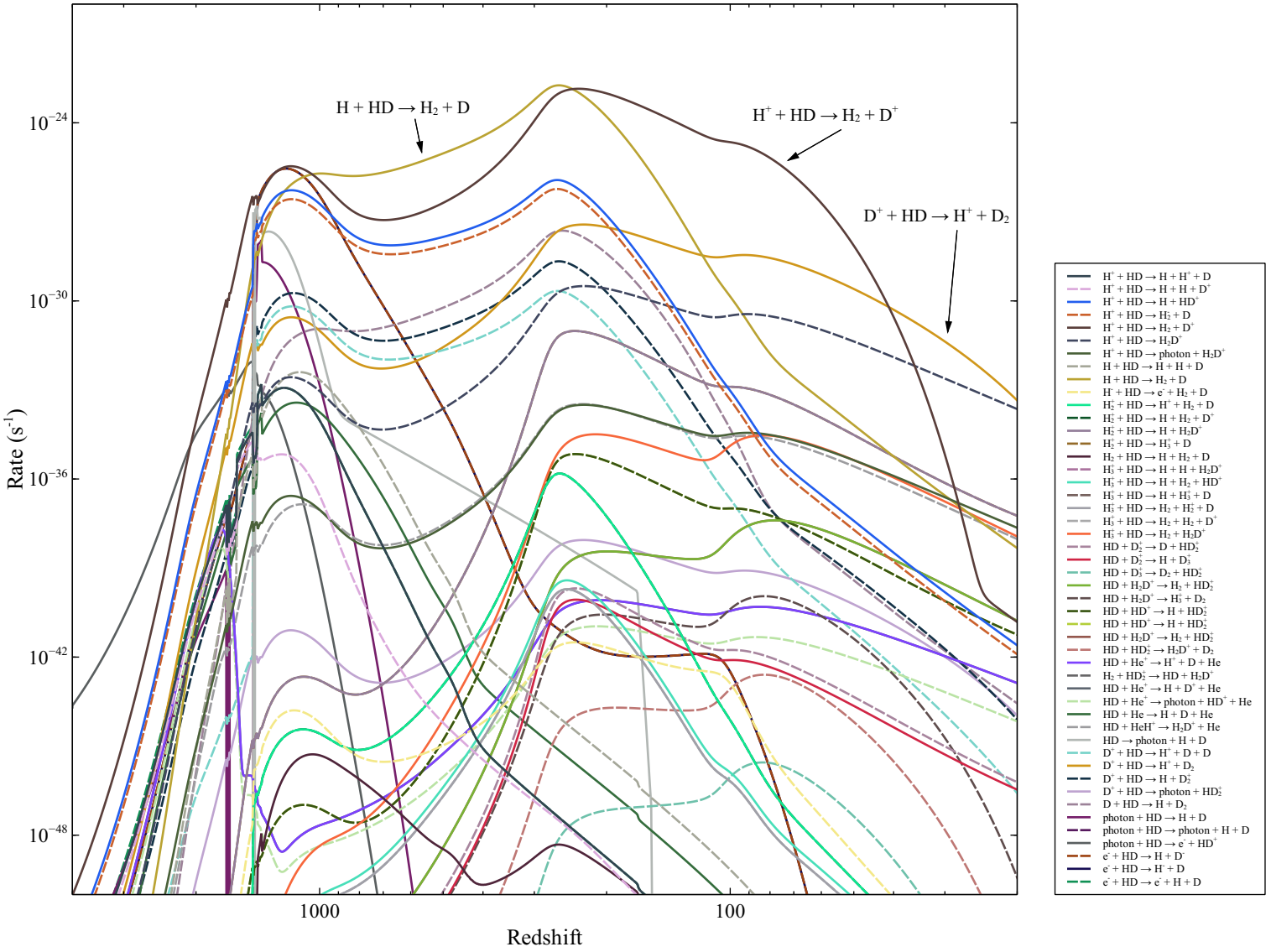

Figure 4.8: Rates of destruction for HD in the Recombination Era. The dominant processes are highlighted.

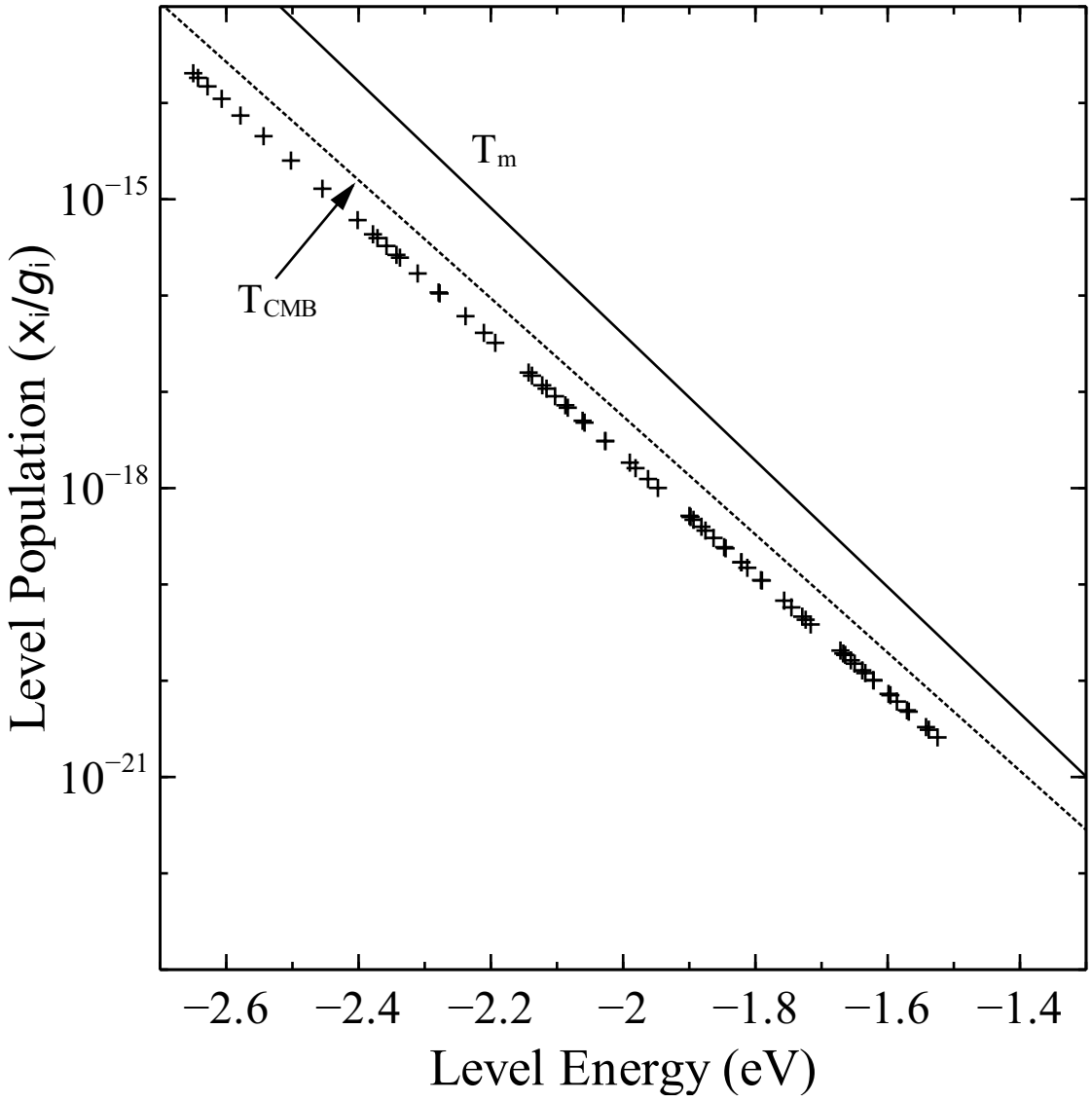

Figure 4.9: Rovibrational level populations of H_2^+ at $z = 300$. $E = 0$ is the dissociation limit of the molecule. The lines indicate Boltzmann equilibrium populations for the radiation (dotted) and matter (solid) temperatures.

4.2 Primordial Cloud Spectral Simulations

Many assumptions are made in currently generated models of primordial cloud collapse, and as the central theme of this dissertation, one of the most widely adopted is that the internal quantum state populations (e.g., rovibrational levels) are thermally populated, the so-called local thermodynamic equilibrium approximation. This common approach is valid in high density environments such as stellar and planetary atmospheres and its application is simple to perform. However, substantial deviations from LTE occur when collisions are too infrequent and the density of the gas is low compared to the critical density of a given internal level. A non-LTE analysis is therefore necessary to properly account for the relevant microphysical processes such as photon absorption, spontaneous emission, stimulated emission, inelastic collisions, and reactions. A developmental version of the spectral synthesis package Cloudy was used to perform an NLTE analysis of a primordial cloud during its free-fall gravitational collapse to a protostellar core, and the resulting NLTE emission spectra are presented here.

After matter and radiation decoupled at the beginning of the Recombination Era, the by-products of Big Band Nucleosynthesis — essentially hydrogen and helium — started to recombine as the temperature of the universe decreased. Primordial clouds of gas developed from density fluctuations and fragmented into clumps (Bromm, Coppi, & Larson 1999, 2002). These clumps have their dynamical stability dependent on Jean's condition, where gravitational collapse occurs when the inward force of gravity becomes greater than the force exerted by the thermal energy of the cloud,

$$3Nk_{\rm B}T < \frac{GM_J^2}{R}, \tag{4.7}$$

where N is the number of particles, $k_{\rm B}$ is the Boltzmann constant, T is the kinetic temperature of the gas, $G = 6.6738 \times 10^{-11}$ m^3 kg^{-1} s^{-2} is the gravitational constant, M_J is the Jean's mass of the cloud, and R is the radius of the cloud. The Jean's mass M_J, or minimum

cloud mass needed for collapse, for a primordial cloud is therefore 10^6 $M_\odot$, which is adopted here as our initial cloud mass. Following from the mass we obtain the Jean's length, or minimum radius of the cloud at collapse, $R \sim 1 \times 10^{20}$ cm, given by

$$R = \sqrt{\frac{15 k_B T}{4\pi \rho G m}}, \tag{4.8}$$

where m is the mass per particle in the cloud and ρ is the density.

In order for runaway collapse to occur, the cooling time must be shorter than the dynamical time and the Hubble time at the epoch of collapse. The dominant way for the gas to cool during this phase is via molecular rovibrational line emission. Molecular line emission is prominent in the spectra as the cloud collapses to form a protostellar core, and LTE molecular line emission from the most abundant molecule, H_2, has been previously studied (see, for example, Ripamonti et al. 2002; Mizusawa et al. 2004). Line cooling via H_2, H_2^+, and HD is examined here and NLTE spectra are synthesized.

The evolution of the primordial cloud is followed from the onset of runaway collapse until the formation of a protostellar core. An initial analytic zero-dimensional top-hat density profile is adopted with the initial number density of hydrogen given by $n_H = 10^4$ cm^{-3}, the number density of molecular hydrogen given by $n_{H_2} = 5 \times 10^{-4}$ cm^{-3}, an electron density fraction of $n_{e^-} = 10^{-8}$, and a gas temperature of T = 200 K, typical values for primordial star-forming regions (Bromm, Coppi, & Larson 2002). The cloud is initially at equilibrium with the timescale for free-fall collapse at the center of the cloud given by

$$t_{ff} = \sqrt{\frac{3\pi}{32 G \rho}}. \tag{4.9}$$

The cooling time is given by $t_{cool} = \rho\epsilon/\Lambda$, where ϵ is the chemical binding energy per unit

mass, and Λ is the cooling rate, made up of the radiative and chemical cooling rates,[2]

$$\Lambda = \Lambda_{\rm rad} + \Lambda_{\rm chem}, \tag{4.10}$$

and is initially longer than the free-fall time. However, after contracting for a period, the cooling time at the center becomes shorter than the free-fall time and the cloud begins to collapse dynamically in a free-fall timescale. The hydrogen becomes almost fully molecular, and as the number density increases drastically, the temperature only increases slightly due to line cooling. As compression continues, the temperature rises and eventually dissociates the molecules needed for radiative cooling. Finally, all the H_2 becomes dissociated and a protostellar core with a central temperature of $\sim 20,000$ K forms. Primordial cloud NLTE emission profiles were computed for H_2, H_2^+, and HD in the collapsing cloud and are shown in Figs. 4.10 - 4.12 for $z = 20$.

The resultant spectra were analyzed for observational characteristics and evaluated for their possible detection by current and future observatories. The most appealing facility for use in the future is NASA's *James Webb Space Telescope* (*JWST*), which will cover the near-IR from $0.6 - 28.5$ μm (Gardner et al. 2006), while the best possiblity for current detection is the Atacama Large Millimeter/submillimeter Array (ALMA), which covers a wavelength range of 300 μm $-$ 3 mm (Remijan et al. 2015). To determine if detection is possible, we first presume that the first stars formed around $1 + z = 20$ (Abel et al. 2002). The brightest H_2^+ rovibrational line of a cloud collapsing at this time is the $v = 1, j = 5 \rightarrow v = 0, j = 3$ transition (see Figure 4.11) with a peak luminosity of $2.99{\times}10^{25}$ erg s^{-1}. The wavelength of this 3.76 μm line emitted from $1 + z = 20$ would be redshifted to 75.2 μm according to the equation

$$1 + z = \frac{\lambda_{\rm obs}}{\lambda_{\rm emit}} \tag{4.11}$$

where $\lambda_{\rm obs}$ and $\lambda_{\rm emit}$ are the observed and emitted wavelengths of the line. The intensity of

[2]Heating rates are denoted by negative Λ.

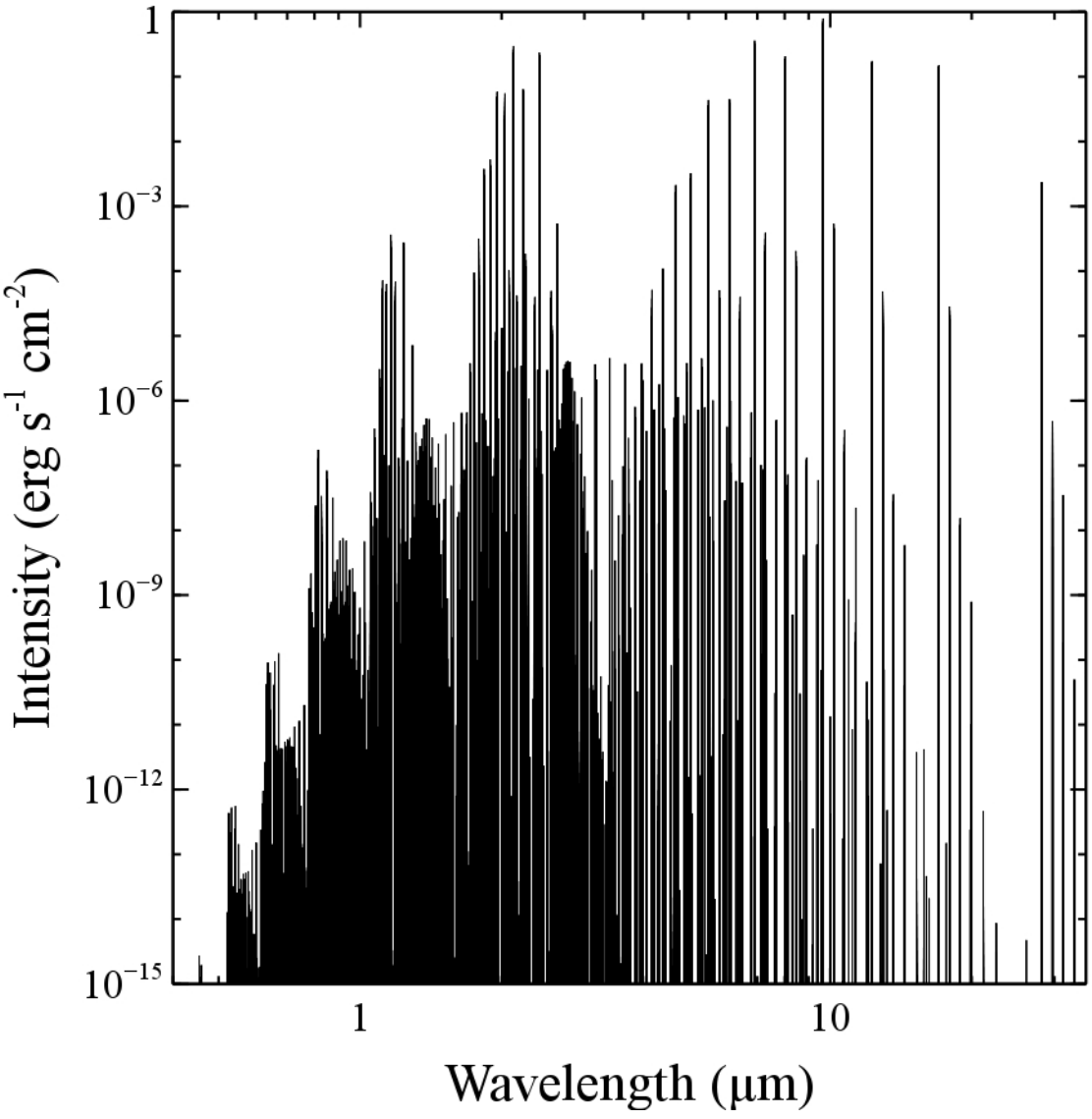

Figure 4.10: The NLTE line emission spectra of H_2 during the collapse of a primordial cloud in the frame of the source.

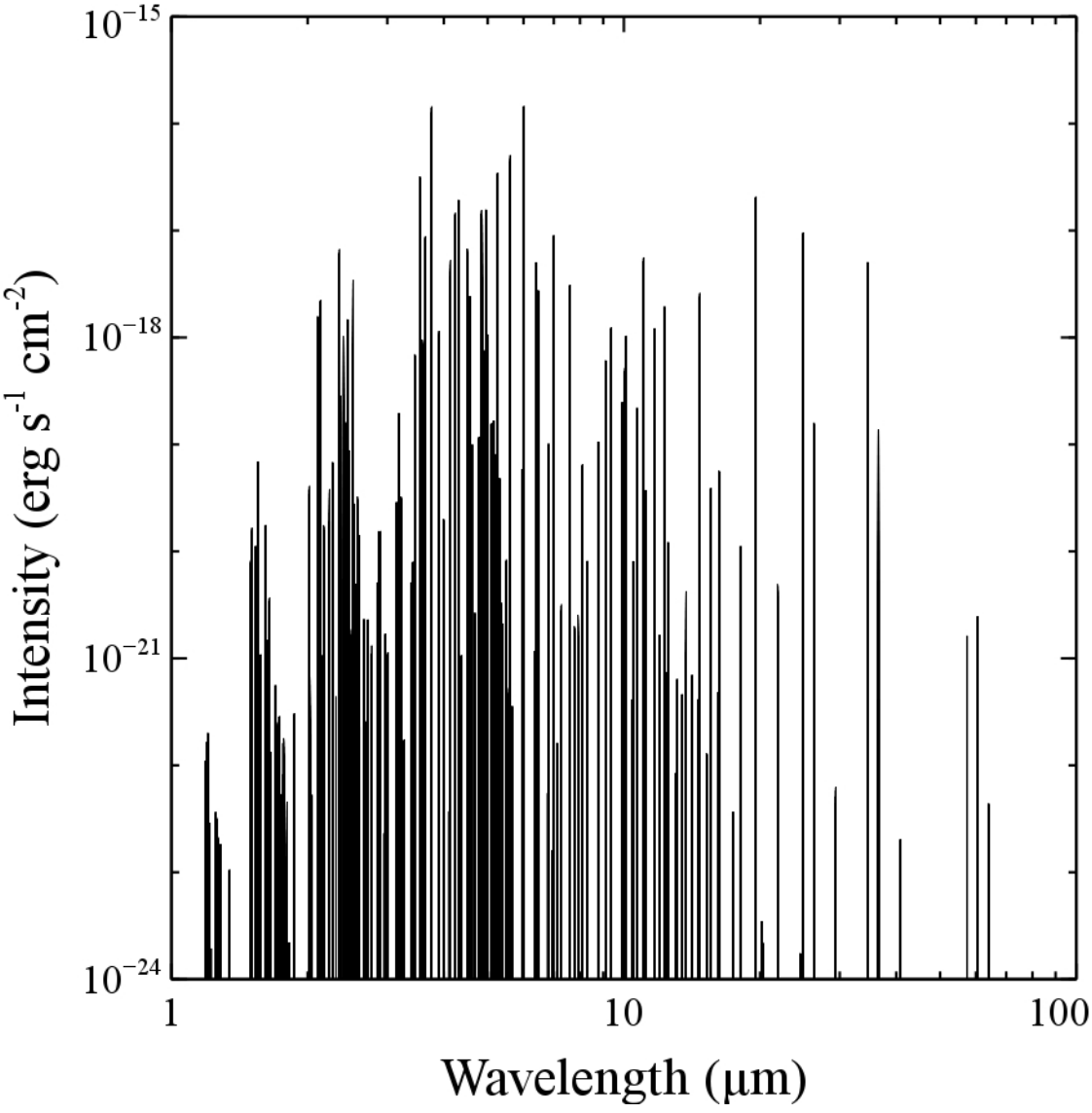

Figure 4.11: The NLTE line emission spectra of H_2^+ during the collapse of a primordial cloud in the frame of the source.

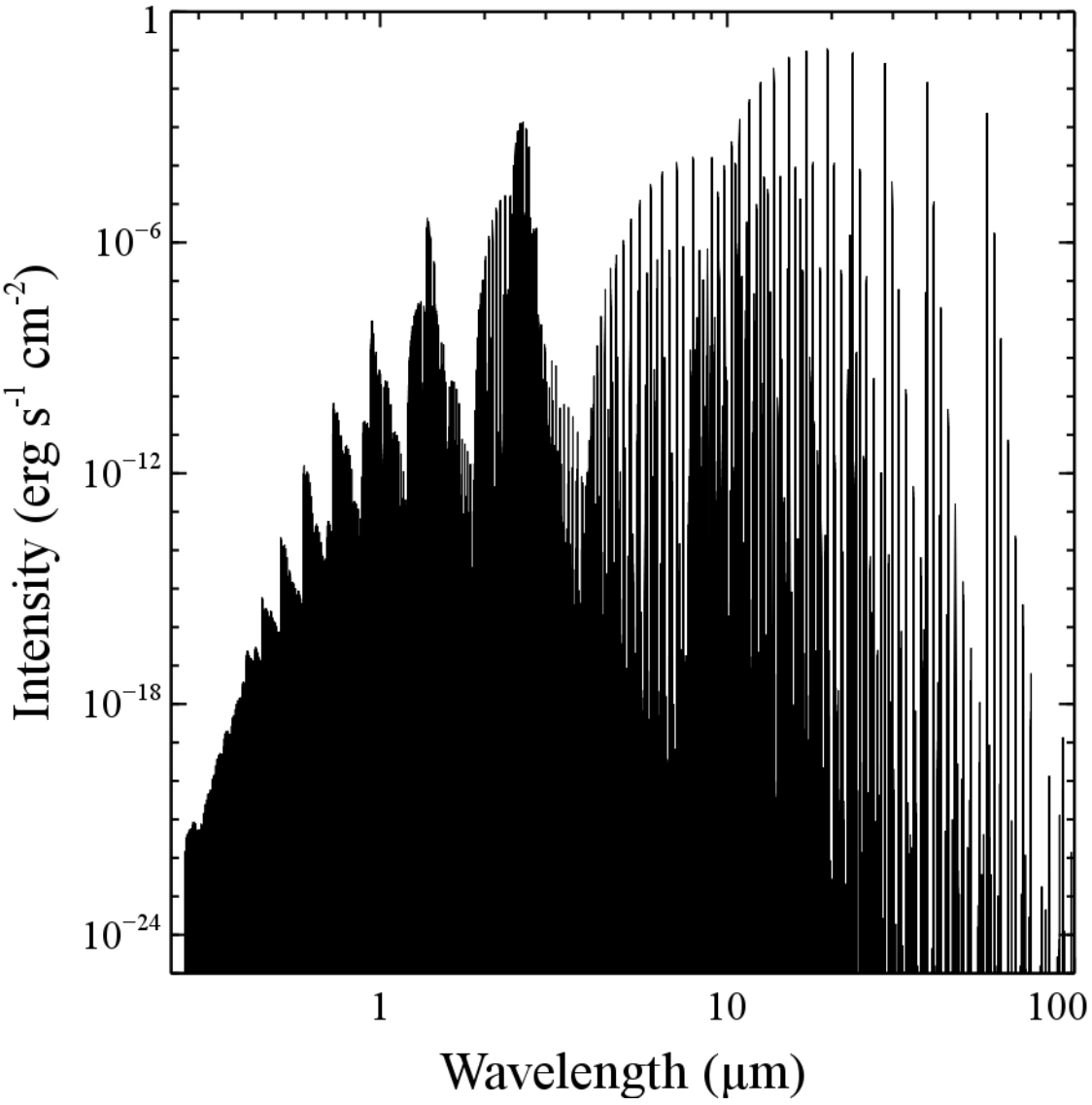

Figure 4.12: The NLTE line emission spectra of HD during the collapse of a primordial cloud in the frame of the source.

this line at earth is given by

$$F_{peak} = \frac{L_{peak}}{4\pi D_{1+z}^2}, \tag{4.12}$$

where D_{1+z} is the luminosity distance given by

$$D_{1+z} = \frac{c(1+z)}{H_0} \int_1^{1+z} \frac{dx}{(\Omega_\Lambda + \Omega_{\rm m} x^3)^{\frac{1}{2}}}, \tag{4.13}$$

where c is the vacuum speed of light. At $1+z = 20$, $D_{20} = 2.13 \times 10^{11}$ pc and therefore the maximum line flux of H_2^+ is $F_{\rm peak} \sim 5{\times}10^{-35}$ erg s^{-1} cm^{-2}. This value does not include extinction.

JWST is an excellent candidate for which to possibly observe primordial star formation, being only background limited by a combination of zodiacal light, thermal emission from the telescope itself, and stray light. The proposed Near-Infrared Specrograph (NIRSpec) and Mid-Infrared Instrument (MIRI) have sensitivities for low resolution or broadband spectroscopy between $8.7 - 700.0$ nJy, while the high resolution modes range in sensitivity from $1.0 \times 10^{-17} - 1.64 \times 10^{-18}$ erg s^{-1} cm^{-2} (Gardner et al. 2006). The sensitivity of ALMA, on the other hand, is in the mJy range. For example, a 60 s integration using 32 12-m antennas over a bandwidth of 7.5 GHz at a frequency of 350 Hz yields an ALMA sensitivity in terms of an image RMS of 0.291 mJy (Remijan et al. 2015). Therefore, even if the strongest rovibrational lines fell in an observable wavelength range, the detectors would still not be able to capture any emission.[3] Unfortunately, the fluxes of these first generation stars are astronomically below the detection threshold of any current or planned instuments and therefore direct observation of a single primordial star formation event is not feasible.

One may also consider the detection possibility for a cluster of star-forming primordial clouds. Assuming a detector sensitivity of 10^{-18} erg s^{-1} cm^{-2}, a cluster of $10^7 - 10^8$ sources of H_2 or HD line emission would have sufficient brightness to be observed. However, the

[3]The decommissioned mid- to far-IR NASA mission *SPICA* would have bridged the gap in wavelength between *JWST* and ALMA. Although impressive sensitivity was planned for *SPICA*, the observatory would also not have been able to detect primordial cloud line emission.

typical free-fall time for collapse is $\sim 10^7$ years, much longer compared to the peak intensity of the spectral lines, which diminish once the protostar forms. Because of the short time scales in which line emission peaks, it is improbable that the collapsing clouds would reach a peak brightness simultaneously and be readily observed.

These primordial cloud collapse models have explored the behavior and interactions of particles in the extreme conditions of the Recombination Era and helped to improve understanding of structure formation and evolution in the earliest epochs. The models investigate the evolution of the universe from the "Dark Ages" into the first generation of stars that would eventually reionize the early universe and determine the composition and structure that is visible today. Future extensions to this work include creating spectra not only for certain epochs but also for various density distributions, chemical abundances, cosmological parameters, and modeling emission as it continues throughout the accretion phase of the protostellar core.

Chapter 5

Conclusions

The three-dimensional H-CO potential energy surface of Song et al. (2013) was used to perform quantum scattering calculations for rotational deexcitation transitions of CO induced by H. State-to-state cross sections for collision energies from 10^{-5} to 15,000 cm^{-1} and rate coefficients for temperatures ranging from 1 to 3000 K were computed for CO pure rotational deexcitation. Not surprisingly, previous scattering results using a PES based on the CCSD(T) level of theory produced similar rate coefficients, but considered only low rotational excitation states. The MRCI surface of Shepler et al. (2007) with a less sophisticated level of theory also produced similar results as presented in Yang et al. (2013b), while the scattering results of Balakrishnan, Yan, & Dalgarno (2002) are deemed to be unreliable due to an inaccurate surface. The H-CO pure rotational rate coefficients presented here can be used to aid astrophysical modeling and they both extend the temperature range and angular momentum quantum number of reported H-CO rate coefficients. Further, while calculations of deexcitation from excited vibrational states are in progress (L. Song et al., 2015, in preparation), experimental data on low-temperature rotational and vibrational inelastic rate coefficients would be highly desirable.

Rotational inelastic transitions for collisions of H, para-H_2, ^{3}He, and ^{4}He with CO(j=1) using three PESs were computed to study the cross section dependence on reduced mass μ and interaction potential with the goal of gaining insight into rate coefficient scaling. Although earlier investigations indicated that scaling via the ratio of the square root of reduced masses gave reasonable estimates for collisional rate coefficients, the current study shows that this agreement was fortuitous (see also Schaefer 1990, for similar findings for HD).

The constant factor of ∼1.4 frequently used to predict the rate coefficients of para-H_2 from that of He generally lead to inaccurate results due to the fact that the underlying assumptions are not valid. Scaling by this standard reduced-mass relation is therefore not recommended. Two alternative scaling approaches are proposed. In the first case, if the inelastic cross section can be represented by an analytical function of the relative velocity, then an exact rate coefficient scaling exists as a function of T and μ, valid for all collision systems. A second approach, which accounts for the contribution of low-energy quasibound resonances, is based on ratios of the product of μ with the PES well-depth. Preliminary testing of the reduced-potential method in conjunction with known propensity rules for CO and H_2O gives reasonable predictions. While these two approaches may lead to mathematically and physically-reasonable scalings, it is only through explicit calculation and/or measurements that reliable inelastic rate coefficients can be obtained. This scaling approach was used to estimate rate coefficients for the deexcitation of rotationally excited HF up to j=20 due to collisions with H_2 and H. The improved scaling approaches proposed here may provide useful estimates until explicit data become available.

Finally, a model of the early universe and a prediction of the spectra of a collapsing primordial cloud during the formation of a first generation star were performed. The work used recent rovibrationally resolved molecular collisional data (H_2^+) and a substantial chemical network of species. The simulations coupled Recombination Era chemical abundances, an appropriate heat equation, and non-thermal level populations with zero-dimensional hydrodynamics to accurately produce the spectra throughout the process of first generation star formation. Furthermore, the resulting spectra of these first generation stars was examined for detection by a current ground-based facility, ALMA, and a future space observatory, *JWST*, and deemed to be undetecable presently neither for one star nor a cluster. Future work includes enhancing the early universe chemical network and considering various density profiles of collapsing primordial clouds.

Many molecular collisional systems remain to be studied, and the parallel codes VRRMM and TwoBC will continue to help calculations progress. In the future, these codes will be used to explore more collisional systems. Further modifications might also include extending the programs for use with systems that include more than four atoms. The new scaling techniques presented here will lead to the production of a large quantity of accurate rate coefficients, exactly what databases such as the BullDog Database (BDDB) and the Virtual Atomic and Molecular Data Centre (VAMDC) are craving. The estimation techniques can become more refined in the future with the addition of energy gap considerations. As larger molecules continue to be found in astrophysical environments and more sophisticated models of the early universe are developed, the demand for atomic and molecular collisional data will only increase. And I will be there to supply it.

Appendix A

LAMDA Files

The Leiden Atomic and Molecular Database data format (Schöier et al. 2005) includes the following information on a given atom or molecule: species name, weight (a.m.u), level energy (cm^{-1}), statistical weight, quantum numbers (usually), spontaneous decay rate (s^{-1}), line frequencies (usually), collision partner(s), values of temperature for collisional data (K), and rate coefficients ($cm^3\ s^{-1}$). The molecular datafiles created for this work can be accessed at [www.physast.uga.edu/amdbs/excitation] and include those of CO, HF, H_2^+, and TiO.

Bibliography

Abel, T., Anninos, P, Zhang, Y., & Norman, M. L. 1997, New Astronomy, 2, 181

Abel, T., Bryan, G. L., & Norman, M. L. 2002, Science, 295, 93

Alexander, M. H., & Manolopoulos, D. E. 1987, JChPh, 86, 2044

Alexander, M. H., Manolopoulos, D. E., Werner, H.-J., Follmeg, B. & Dagdigian, P. J. 1987-2011, HIBRIDON computer program, available at [http://www2.chem.umd.edu/groups/alexander/hibridon/hib43].

Alizadeh, E., & Hirata, C. 2011, Phys. Rev. D, 84, 083011

Adande, G. R., Edwards, J. L., & Ziurys, L. M. 2013, ApJ, 778, 22

Arthurs, A. M., & Dalgarno, A. 1960, Pro. Roy. Soc. London A, 256, 540

Balakrishnan, N., Yan, M., & Dalgarno, A. 2002, ApJ, 568, 443

Bennett, C.L., et al. 2003, ApJS, 148, 1

Bowman, J. M., Bittman, J. S., & Harding, L. B. 1986, JChPh, 85, 911

Bromm, V., Coppi, P. S., & Larson, R. B. 1999, ApJ, 527, L5

Bromm, V., Coppi, P. S., & Larson, R. B. 2002, ApJ, 564, 23

Bromm, V., Yoshida, N., & Hernquist, L. 2003, ApJ, 596, 135L

Cecchi-Pestellini, C., Bodo, E., Balakrishnan, N., & Dalgarno, A. 2002, ApJ, 571, 1015

Cernicharo, J., Barlow, M. J., González-Alfonso, E., Cox, P. et al. 1996, A&A, 315, L201

Cernicharo, J., et al. 2011, A&A, 531, 103

Child, M. S. 1996, Molecular Collision Theory (2nd Ed.; Mineola: Dover)

Chu, S.-I., & Dalgarno, A. 1975, RSPSA, 342, 191

Clegg, P. E., Ade, P. A. R., Armand, C., Balutea, J.-P. 1996, A&A, 315, L38

Coppola, C. M., Longo, S., Capitelli, M., Palla, F., & Galli, D. 2011, ApJS, 193, 7

Coppola, C. M., Lodi, L., & Tennyson, J. 2011, MNRAS, 415, 487

Coppola, C. M., D'Introno, R., Galli, D., Tennyson, J., & Longo, S. 2012, ApJS, 199, 16

Dalgarno, A., Black, J. H., & Weisheit, J. C. 1973, Astrophys. Let., 14, 77

Dunning, T. H., Jr., & Hay, P. J. In Methods in Electronic Structure Theory, edited by H. F. Schaefer III (Plenum, New York, 1971)

Dubernet, M.-L., Daniel, F., Grosjean, A., & Lin, C. Y. 2009, A&A, 497, 911

de Graauw, T., Helmich, F. P., Phillips, T. G., Stutzki, J., et al. 2010, A&A, 518, L6

Emprechtinger, M., Monje, R. R., van der Tak, F. F. S., van der Wiel, M. H. D., et al. 2012, ApJ, 756, 136

Faure, A., et al. 2005, J. Chem. Phys., 122, 221102

Ferland, G. J., et al. 2013, RMxAA, 49, 1

Florian, P. M., Hoster, M., & Forrey, R. C. 2004, Phys. Rev. A, 70, 032709

Flower, D. 2007, Molecular Collisions in the Interstellar Medium (2nd ed; Cambridge: Cambridge University Press)

Flower, D. R., Bourhis, G., & Launay, J.-M. 2000, CPC, 131, 187

Fonseca dos Santos, S., Balakrishnan, N., Forrey, R. C., & Stancil, P. C. 2013, J. Chem. Phys., 138, 104302

Forrey, R. C., Balakrishnan, N., Dalgarno, A., & Lepp, S. 1997, ApJ, 489, 1000

Galli, D., & Palla, F. 1998, A&A, 335, 403

Gardner, J. P., Mather, J. C., Clampin, M., et al. 2006, Space Sci. Rev., 123, 485

Gay, C. D., Stancil, P. C., Lepp, S., & Dalgarno, A. 2011, ApJ, 737, 44

Glover, S. C. O., & Abel, T. 2008, MNRAS, 388, 1627

Goldsmith, P. F. 2013, ApJ, 774, 134

Green, S. 1993, ApJ, 412, 436

Green, S., & Thaddeus, P. 1976, ApJ, 205, 766

Green, S., Garrison, B. J., Lester, W. A., & Miller, W. H. 1978, ApJS, 37, 321

Green, S., Keller, H.-M., Schinke, R., & Werner, H.-J. 1996, JChPh, 105, 5416

Griffin, M. J., Abergel, A., Abreu, A., Ade, P. A. R., et al. 2010, A&A, 518, L3

Guillon, G., & Stoecklin, T. 2012, MNRAS, 420, 579

Guillon, G., Stoecklin, T., Voronin, A., & Halvick, P. 2008, J. Chem. Phys., 129, 104308

Heijmen, T. G. A., Moszynski, R., Wormer, P. E. S., & van der Avoird, A. 1997, J. Chem. Phys., 107, 9921

Hinshaw, G., Larson, D., Komatsu, E., et al. 2013, ApJ, 208, 19

Hirata, C., & Padmanabhan, N. 2006, MNRAS, 372, 1175

Hutson, J. M. & Green, S. 1994, MOLSCAT computer code (Version 14, Distributed by Collaborative Computational Project No. 6; Swindon, UK: Engin., & Phys. Sci. Res. Council)

Huzinaga, S. Approximate Atomic Wave Functions. I, Chemistry Report, University of Alberta, Edmonton, 1971

Jankowski, P. & Szalewicz, K. 2005, J. Chem. Phys., 123, 104301

Joachain, C. J. 1979, Quantum Collision Theory, North-Holland

Kamaya, H., & Silk, J. 2003, MNRAS, 339, 1256

Keller, H.-M., et al. 1996, JChPh, 105, 4983

Kessler, M. F., Steinz, J. A., Anderegg, M. E., Clavel, et al. 1996, A&A, 315, 27

Komatsu, E., Dunkley, J, Nolta, M. R., et al. 2009, ApJS, 180, 330

Krems, R. V. 2006, TwoBC quantum scattering program (University of British Columbia)

Krems, R. V. 2008, Phys. Chem. Chem. Phys., 10, 4079

Krstič, P. S. 2002, Phys. Rev. A, 66, 042717

Knowles, P. J., & Werner, H.-J. 1985, ChPhL, 115, 259

Knowles, P. J., Hampel, C., & Werner, H.-J. 1994, JChPh, 99, 5219

Lee, K.-T., & Bowman, J. M. 1987, JChPh, 86, 215

Lepp, S., Stancil, P. C., & Dalgarno, A. 2002, J. Phys. B, 35, R57

Lique, F., et al. 2008, A&A, 478, 567

Liszt, H. S. 2006, A&A, 458, 507

Liu, X.-W., Barlow, M. J., N.-Q.-R., Truong-Bach. 1996, A&A, 315, L257

Mather, J. C., Fixsen, D. J., Shafer, R. A., et al. 1999, ApJ, 512, 511

Matsuda, T., Sato, H., & Takeda, H. 1969, Prog. Theor. Phys., 42, 219

Matsuura, M. et al. 2014, MNRAS, 437, 532

McGuire, P., & Kouri, D. J. 1974, J. Chem. Phys., 60, 2488

Mizusawa, H., Nishi, R., & Omukai, K. 2004, PASJ, 56, 487

Mizusawa, H., Omukai, K., & Nishi, R. 2005, PASJ, 57, 951

Moszynski, R., Wormer, P. E. S., Jeziorski, B., & van der Avoird, A. 1994, J. Chem. Phys., 101, 2811

Müller, H. S. P., Schlöder, F., Stutzki, J., & Winnewisser, G. 2005, J. Mol. Struct. 742, 215

Neufeld, D. A., Zmuidzinas, J., Schilke, P., & Phillips, T. G. 1997, ApJ, 488, L141

Nisini, B., Lorenzetti, D., Cohen, M., Ceccarelli, C., et al. 1996, A&A, 315, L321

Nolte, J. L., Stancil, P. C., T.-G. Lee, T.-G., Balakrishnan, N., & Forrey, R. C. 2012, ApJ, 744, 62

Nordh, H. L., von Schéele, F., Frisk, U., Ahola, K., et al. 2003, A&A, 402, L21

Omukai, K. 2000, ApJ, 534, 809

Omukai, K. 2006, ASPC, 353, 2630

Omukai, K., & Palla, F. 2001, ApJ, 561, 55L

Omukai, K., Tsuribe, T., Schneider, R., & Ferrara, A. 2005, ApJ, 626, 627

Osterbrock, D. E. & Ferland, G. J. 2006, Astrophysics of Gaseous Nebulae and Active Galactic Nuclei (2nd ed.; Sausalito: University Science)

Panuzzo, P., Rangwala, N., Rykala, A., Isaak, K. G., et al. 2010, A&A, 518, L37

Patkowski, K., et al. 2002, J. Mol. Struct., 591, 231

Persson, C. M., Olofsson, A. O. H., Koning, N., & Bergman, P. 2007, A&A, 476, 807

Pettini, M., & Bowen, D. V. 2001, ApJ, 560, 41

Pickett, H. M., Poynter, R. L., Cohen, E. A., Delitsky, M. L., Pearson, J. C., & Muller, H. S. P. 1998, J. Quant. Spectrosc. & Rad. Transfer, 60, 883

Pilbratt, G. L., Riedinger, J. R., Passvogel, T., Crone, G., et al. 2010, A&A, 518, L1

Pilleri, P., Fuente, A., Cernicharo, J., Ossenkopf, V., et al. 2012, A&A, 544, A110

Polehampton, E. T., Menten, K. M., van der Tak, F. F. S., & White, G. J. 2010, A&A, 510, A80

Purvis, G. D., & Bartlett, R. J. 1982, JChPh, 76, 1910

Radzig, A. A., & Smirnov, B. M. 1980, Reference Data on Atoms, Molecules, and Ions (Springer-Verlag)

Remijan, A., et al. 2015, ALMA Cycle 3 Technical Handbook Version 1.0 (ALMA)

Ripamonti, E., Haardt, F., Ferrara, A., & Colpi, M. 2002, MNRAS, 334, 401

Roueff, E. & Lique, F. 2013, Chem. Rev., 113, 8906

Sakurai, J. J. 1994, Modern Quantum Mechanics Revised Ed. (Reading: Addison-Wesley)

Saslaw, W. C., & Zipoy, D. 1976, Nature, 216, 976

Schaefer, J. 1990, A&AS, 85, 1101

Schneider, N., Stutzki, J., Winnewisser, G., Block, D. 1998, A&A, 335, 1049

Schöier, F. L., van der Tak, F. F. S., van Dishoeck, E. F., & Black, J. H. 2005, A&A, 432, 369

Shepler, B. C., Yang, B. H., Dhilip Kumar, T. J., Stancil, P. C., et al. 2007, A&A, 475, L15

Song, L., van der Avoird, A., & Groenenboom, G. 2013, JPhCh A, 117, 7571

Songaila, A. 2001, ApJ, 561, 153

Sonnentrucker, P., Neufeld, D. A., Phillips, T. G., Gerin, M. et al. 2010, A&A, 521, L12

Stancil, P. C. 1994, ApJ, 430, 360

Stancil, P. C. & Zygelman, B. 1995, Phys. Rev. Lett., 75, 1495

Stancil, P. C., Lepp, S., & Dalgarno, A. 1998, ApJ, 509, 1

Stark, K., & Werner, H.-J. 1996, J. Chem. Phys., 104, 6515

Switzer, E. R., & Hirata, C. M. 2008, Phys. Rev. D, 77, 083006

Tejeda, G., Thibault, F., Fernández, J. M., & Montero, S. 2008, J. Chem Phys., 128, 224308

Thi, W. F., Kamp, I., Woitke, P., van der Plas, G., et al. 2013, A&A, 551, A49

Valiron, P., & McBane, G. C. 2008, Mixed MPI and OpenMP extension of the MOLSCAT v14 package.

van der Tak, F. F. S., Black, J. H., Schöier, F. L., Jansen, D. J., & van Dishoeck, E. F. 2007, A&A, 468, 627

van der Tak, F. F. S. 2011, in The Molecular Universe (IAU Symposium 280), eds. J. Cernicharo & R. Bachiller, p. 449

van der Tak, F. F. S., Ossenkopf, V., Nagy, Z., Faure, A., Röllig, M., Bergin, E. A. 2012, A&A, 537, L10

Wagoner, R. V., Fowler, W. A., & Hoyle, F. 1967, ApJ, 148, 3

Walker, K. M. 2013, VRRMM: Vibrational/Rotational Rich Man's MOLSCAT v3.1.

Walker, K. M., Yang, B. H., Stancil, P. C., Balakrishnan, N., & Forrey, R. C. 2014, ApJ, 790, 96

Walker, K. M., Song, L., Yang, B. H., et al. 2015, ApJ, *submitted June 2015*

Werner, H.-J., & Knowles, P. J. 1989, JChPh, 89, 5803

Werner, H.-J., Bauer, C., Rosmus, P, Keller, H.-M., Stumpf, M., & Schinke, R. 1995, JChPh, 102, 3593

Werner, H.-J. & Knowles, P. J., with contributions from Almlöf, J., Amos, R. D. , Deegan, M. J. O., Elbert, S. T., Hampel, C., Meyer, W., Peterson, K., Pitzer, R., Stone, A. J., & Taylor, P. R. MOLPRO is a package of *ab initio* programs. http://www.molpro.net

Woon, D. E., & Dunning, T. H., Jr. 1994, JChPh, 100, 2975

Yang, B. H., Perera, H., Balakrishnan, N., Forrey, R. C., & Stancil, P. C. 2006, J Phys. B, 39, S1229

Yang, B. H., Stancil, P. C., Balakrishnan, N., & Forrey, R. C. 2010, ApJ, 718, 1062

Yang, B. H., et al. 2013a, ApJ, 765, 77

Yang, B. H., et al. 2013b, ApJ, 771, 49

Yang, B. H., Walker, K. M., Forrey, R. C. et al. 2015, A&A, 578, A65

Yildiz, U. A., van Dishoeck, E. F., Kristensen, L. E., Visser, R., et al. 2010, A&A, 521, L40

Yoshida, N., Abel, T., Hernquist, L., & Sugiyama, N. 2003, ApJ, 592, 645

Yoshida, N., Omukai, K., Hernquist, L., & Abel, T. 2006, ApJ, 652, 6